UNIVERSITÀ DI PARMA

# UNIVERSITA' DEGLI STUDI DI PARMA

DOTTORATO DI RICERCA IN FISICA

CICLO XXXII

# $TiO_2$-graphene nanostructures for energy storage: materials and devices


Coordinatore:

**Chiar.mo Prof. Stefano Carretta**

Tutori:

**Chiar.mo Prof. Danilo Bersani**

**Chiar.mo Prof. Daniele Pontiroli**

Dottoranda:

**Laura Fornasini**


Anni 2016/2019

*This page intentionally left blank*

*A chi è vicino da lontano,*
*a chi è vicino da vicino*

*This page intentionally left blank*

*"We have only got one Earth.*
*We can't use 1.75 without destructive consequences"*

Mathis Wackernagel,
co-inventor of Ecological Footprint

*This page intentionally left blank*

# Abstract

Electrical energy storage devices are dominating the market of mobile electronics and their relevance is growing in hybrid vehicles systems. Rechargeable batteries and supercapacitors are the most investigated devices. The current interest in improving the electrochemical properties of materials and devices has been currently focused on the development of composite materials, exploiting their structure and properties. Graphene is an intriguing material due to its high electrical conductivity, flexibility and large theoretical specific surface area. Nanostructures have been suggested to be combined to graphene to achieve electroactive sites for a remarkable electrochemical performance. Titanium dioxide ($TiO_2$) is a promising candidate in connecting its electrochemical properties with the synthesis methods to obtain it as a nanocrystalline material. Composite materials based on $TiO_2$ and graphene have been reported as anode materials in lithium-ion batteries, the highest current technology of rechargeable batteries. Furthermore, this combination has been effective as electrodes in supercapacitors. Improvements in terms of energy and power densities, costs and safety can be obtained.

In this research, nanostructured $TiO_2$-graphene based materials have been successfully synthesized to be tested as electrodes in rechargeable Li-ion batteries and micro-supercapacitors. A thermally exfoliated graphite oxide (TEGO) has been chosen as graphene material, to take advantage of its defective structure for an *in situ* synthesis of anatase $TiO_2$ nanoparticles onto graphene surface, through a hydrothermal route. A solid-state approach has been also performed to obtain the composite material by a high-energy ball milling treatment. $TiO_2$-TEGO materials have been tested as electrode in lithium-ion half cells. To produce laser-scribed micro-supercapacitors, innovative technologies have been investigated by using the DVD burner laser. A novel approach has been optimized to promote the simultaneous synthesis of nanocrystalline anatase and graphene-based material. The electrochemical performance of lithium-ion half-cells and laser-scribed micro-supercapacitors has been improved thanks to the combination of these materials, making $TiO_2$-graphene nanostructures a remarkable candidate in electrical energy storage devices.

*This page intentionally left blank*

# Table of Contents

*This page intentionally left blank*

# 1 $TiO_2$ and graphene in energy storage

2019, July 29th: the Earth Overshoot Day

2019, October 9th: Nobel Prize in Chemistry
*"for the development of lithium-ion batteries"*

What do these dates have in common?

According to the Global Footprint Network, the international organization monitoring the ecological man footprint, humanity is currently using nature as if there was 1.75 Earth, even though we have only one. The Earth Overshoot Day refers to the date of the year on which the resources consumption by humanity exceeds what the Earth can regenerate in the year. In the last decades, every year the Earth Overshoot Day has moved up, from December 21st in 1971 to July 29th in 2019. Solutions should be found promptly, in how we manage cities, how we feed ourselves, how we deal with food, how we help nature. One of the most challenging goal is cutting $CO_2$ emissions from fossil fuel burning and greenhouse gas emissions. Making a fossil fuel-free world should not be a utopia. Renewable energy can represent the best option to replace fossil fuel energy [1].

2019 is also the year of the Nobel Prize *"for the development of lithium-ion batteries"*. John Bannister Goodenough, Micheal Stanley Whittingham, and Akira Yoshino were awarded with the Nobel Prize in chemistry for their work and discoveries in lithium-ion batteries, the current highest technology in the field of rechargeable batteries for energy storage. Lithium-ion batteries have had – and are still having – a huge impact on our lives, as the driving force of mobile electronics revolution and the foundations for the change from fossil fuel-based vehicles to hybrid and full electric vehicles (HEVs and EVs, respectively) [2].

An efficient energy storage is an essential requirement for many of the sources which produce electricity. The current fundamental importance of electrical energy has led to the development and the growth of renewable energies, which are expected to increase their relevance in the next years, at the expense of fossil fuel energy. Renewable energies strongly

require energy storage, due to their intrinsic intermittent behaviour. They fluctuate over time and they are independent from demand. As an example, wind energy for electrical production is unpredictable and uneven. Solar energy is not constant over time, ranging from day to night. To overcome this discontinuous trend, energy storage systems are required, since they can store energy and give it back when needed. Storing energy can be achieved by the transformation of energy into different forms, such as chemical, electrochemical, mechanical or thermal energy.

Hence, great attention has been recently focused on developing novel storage methods and innovative new materials. Electric energy storage technologies can convert electric energy into chemical, electrochemical, mechanical or thermal energy and re-convert into electricity when needed. They are currently growing in researching and developing successful materials and devices. There are already many of them in the market.

Electrical energy storage devices (EESDs) dominate the market of mobile electronics and their relevance is growing in transportation systems and space applications. Portable equipment is used in laptops, smartphones, wearable computers as well as medical and implantable devices and miniaturized sensors. Transportation systems involve EESDs in HEVs and EVs.

## 1.1 Electrical Energy Storage Devices

For suitable applications, the size of electrical energy storage devices (EESDs) is crucial and their electrochemical properties are strongly connected to it. EESDs properties are essential in determining their performance. Key features are the following: (1) storage capacity, referring to the capacity achieved by the total stored charge in the device. Capacity is usually expressed as volumetric or gravimetric capacity, known as specific capacity; (2) specific energy, or energy density, being the energy per unit mass or volume, which depends on specific capacity and voltage potential; (3) specific power, or power density, being the maximum power per unit mass or volume, which deals with power delivery; (4) efficiency, as the ratio between stored and released charge; (5) capacity retention, being the fraction of the initial capacity (and charge) which the device can store after being repeatedly cycled; (6) life-cycle, being the number of cycles the device can be cycled for; (7) cycle stability, strongly connected to the device life-cycle; (8) self-discharge, as the capacity loss due to internal leakage; (9) rate capability, being the current the device can deliver without significantly affecting its performance.

EESDs mainly consist of rechargeable batteries and supercapacitors.

Rechargeable batteries are electrochemical energy storage devices which convert chemical energy into electrical energy and can store energy in the device, making it available when required. They dominate the mobile and portable market, from laptops and smartphones to microelectronics such as medical devices or integrated circuits and sensors. High specific energy is one of the main strengths of rechargeable batteries. Li-ion batteries (LIBs) are the state-of-the-art with their highest specific energy. Sodium-ion batteries (SIBs) are currently growing up as alternative to LIBs in order to reduce safety concerns and costs, thanks to sodium abundancy in nature. Magnesium-ion batteries (MIBs) are the newest rechargeable battery technology, as well as an eco-compatible replacement to LIBs. Among rechargeable batteries, great interest has currently been focused also on lithium-air (LABs), sodium-air (SABs) and lithium-sulphur (LSBs) batteries, in order to increase electrochemical performance of the cells, especially in terms of specific energy.

Capacitors are electric energy storage devices which store electrical energy and deliver high specific power, being charged and discharged in shorter time than batteries. Lower specific energies are achieved compared to batteries.

Supercapacitors, also known as Electrochemical Double Layer Capacitors (EDLCs) are EEDs matching capacitors and batteries characteristics, achieving energy and power densities between them. They are used in high-power applications which require short-term storage, such as regenerative braking systems. Long life-cycle is one of the key features of supercapacitors [3–8].

Detailed description of how Li-ion batteries and supercapacitors work will be discussed in the next chapters (chapters 2 and 3).

To meet the demand of the market, improving electrochemical performance of EESDs plays a fundamental role in materials science and research. As mentioned before, energy and power densities are crucial properties to be optimized in the devices. Figure 1.1 show the plot of specific power against specific energy of the most investigated EESDs, known as Ragone plot.

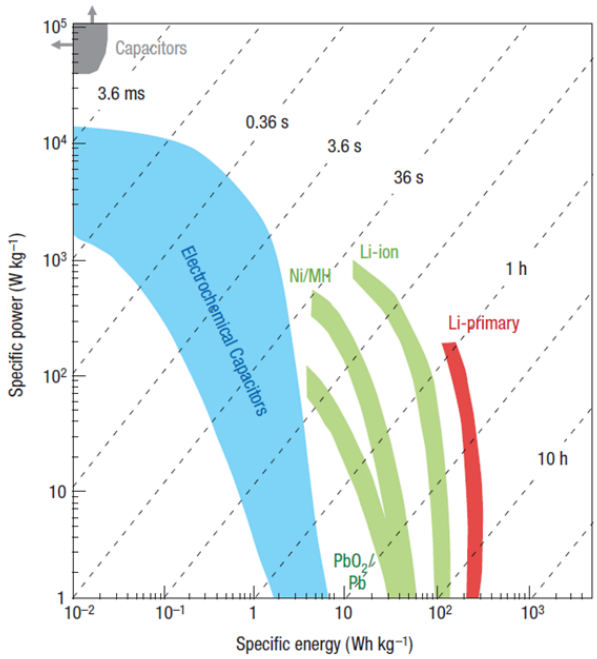


*Figure 1.1 Ragone plot for EESDs. Times shown are time constants of the devices, obtained by the ratio of the energy density to the power density* [4].

The focus on materials science has been devoted to find electrode materials satisfying the above-mentioned electrochemical properties, with high electrical conductivity, low toxicity and low costs. Nanostructured materials have been encouraged to improve the electro-activity of the surface, thanks to their high surface-to-volume ratio.

Since its discovery in 2004, graphene has been reported as a promising material as electrode, exhibiting a high electrical conductivity (up to 8000 S/m) and a high theoretical specific surface area (~2630 $m^2/g$). Besides, nanostructured transition metal oxides have been explored as electrode materials as well, thanks to their abundancy, low cost and the innumerable skills to synthesize them at the nano-scale. Among them, titanium dioxide ($TiO_2$) has attracted great interest. Since transition metal oxides usually suffer from low electrical conductivity, the combination with graphene has been effective in obtaining good electrochemical properties. Detailed investigation about $TiO_2$-graphene composite materials will be illustrated in the next chapters.

## 1.2 Graphene

Graphene is a 2D carbon allotrope consisting of a monolayer of carbon atoms in a honeycomb lattice. Graphene represents the building block of graphitic materials: wrapping graphene in 0D structures gives shape to fullerenes (buckyballs), rolling into 1D to nanotubes, stacking in 3D to graphite, as depicted in figure 1.2. Before its discovery in 2004 by Geim and Novoselov [9], graphene was expected not to exist in a free state, being unstable. The first isolation was performed by microchemical exfoliation of graphite (known as *scotch-tape* method), which leads to the peeling of flakes of single carbon layer. Then, several methods to produce graphene have been investigated, in order to overcome the low yield of the process and the small dimension of flakes (~1 mm). Synthesis techniques consist of mechanical or chemical exfoliation, epitaxial growth, chemical vapour deposition (CVD) and even the *un-zipping* of carbon nanotubes. The method used for the production influences graphene properties and electrochemical properties. Large-scale graphene production can be achieved by using exfoliation processes. This aspect is crucial in determining a wide spread of graphene in applications.

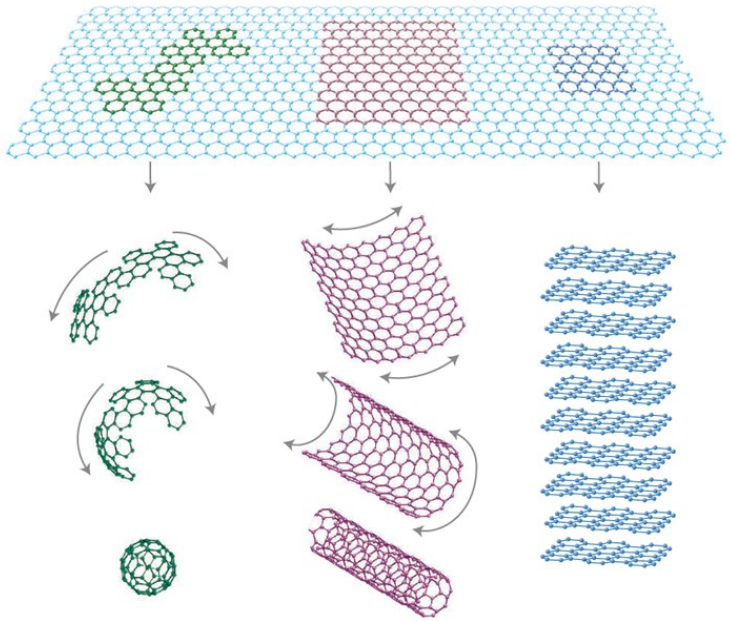

*Figure 1.2 Schematic representation of graphene (on top) and fullerenes, nanotubes and graphite (at the bottom from left to right)* [9].

### 1.2.1 Graphene electronic properties

Figure 1.3 shows the lattice structure of graphene in real and reciprocal space. The crystalline structure of graphene consists of a hexagonal lattice, formed by two sub-lattices. Carbon atoms of each sub-lattice are in the centre of the triangles from the other sub-lattice. The distance between two carbon atoms in a C-C bond is 1.42 Å. In the reciprocal space, the graphene structure consists of a hexagonal Bravais lattice, with two atoms per unit cell. Hexagons in the reciprocal space represent the first Brillouin zone: the point in the centre is known as *Γ*; *K* and *K'* are hexagon corners, belonging to each sub-lattice; *M* refers to the middle point between K and K'.

The electronic structure has been calculated through the tight-binding model for graphite [10], by using Bloch wavefunctions. As for graphite, one of the four valence electrons is involved in electronic properties, while the others are forming in-plane bonds with adjacent atoms. The electronic band structure consists of two bands, usually named π and π* for the lower and the upper one, corresponding to the valence and the conduction bands, respectively, as shown in figure 1.4. Valence band and conduction band join into six points, corresponding to K and K' points in the first Brillouin zone.

In neutral graphene, the valence band is filled, while the conduction band is completely unoccupied. As Fermi energy ($E_F$) is defined as the highest occupied energy, $E_F$ is found exactly in correspondence of these six points, known as *Dirac points*. The linear dependence between band energy and momentum in correspondence of the Dirac points can be seen from the inset in figure 1.4. Thus, the electronic structure in Dirac points resembles that of a zero-gap semiconductor [11], in which the Dirac relativistic equation, rather than the non-relativistic Schrödinger equation, describes the carrier transport in graphene [12].

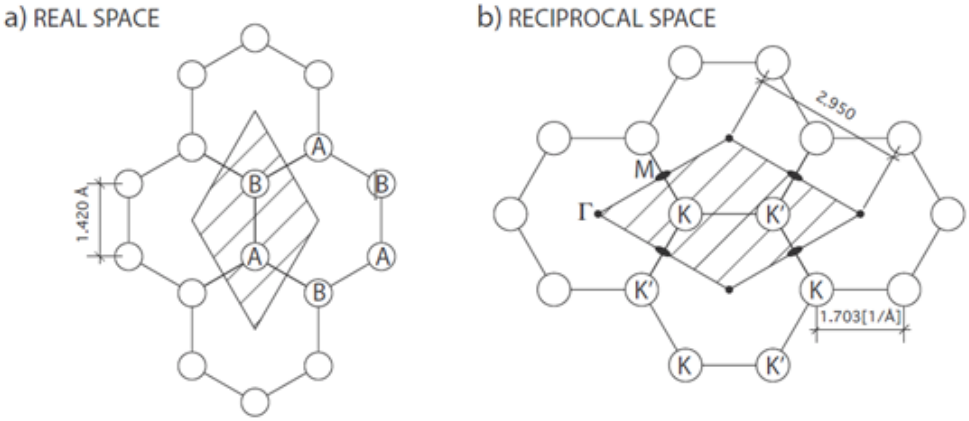


*Figure 1.3 Lattice structure of graphene: (a) real and (b) reciprocal lattice. In the real space, carbon atoms are depicted with open circles: A and B refer to the two sub-lattices in the real space. The diamond represents the real space primitive cell. In the reciprocal space, Γ, M, K and K' refer to the points in the first Brillouin zone. The diamond represents the primitive unit cell* [13].

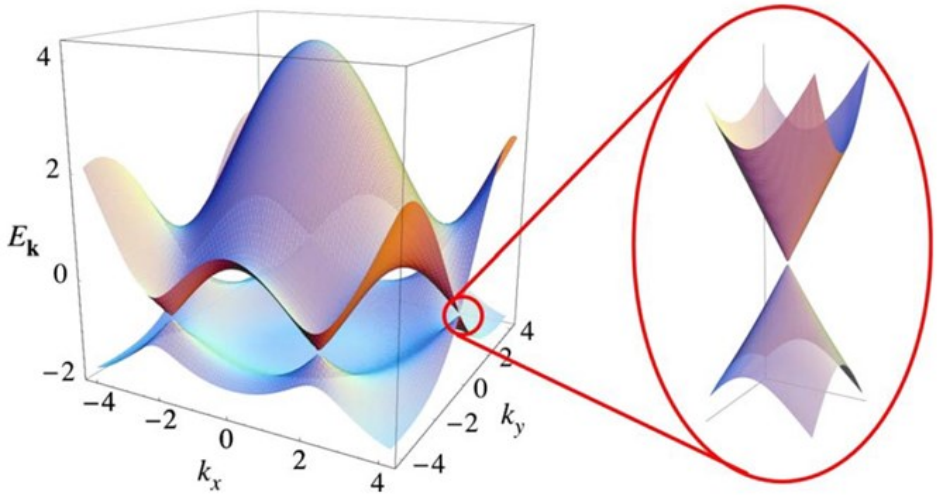


*Figure 1.4 Electronic band structure of graphene. In the inset, a zoom of the energy band close to K point is shown, forming the so-called "Dirac cones"* [11].

## 1.3 Titanium dioxide

Titanium dioxide ($TiO_2$) is a large band-gap semiconductor metal oxide with three main polymorphs: anatase, rutile and brookite. $TiO_2$, also known as *titania*, has been widely investigated in several field of applications thanks to its high abundance, chemical stability, low cost and toxicity. Applications range from photocatalysis of organic pollutants, pigments, sensors, photovoltaic cells, up to energy storage [14–17].

In all the three forms, titanium ($Ti^{4+}$) is coordinated to six oxygen atoms ($O^{2-}$), forming $TiO_6$ octahedra, where oxygen ions are in the corners, while titanium is in the centre. The three polymorphs differ in the 3D assembly of octahedra. In addition to anatase, rutile and brookite, other polymorphs can be obtained: $TiO_2$-B (bronze), $TiO_2$-R (ramsdellite), $TiO_2$-H (hollandite), $TiO_2$-II (columbite) and $TiO_2$-III (baddeleyite) [18]. $TiO_2$-II and $TiO_2$-III are high-pressure $TiO_2$ phases [19]. Crystal structures are shown in figure 1.5. The structural properties of each polymorphs are summarized in table 1.1.

Anatase is a meta-stable phase and irreversibly converts into rutile at temperature exceeding 600 °C. Anatase has a tetragonal structure $I4_1/amd$ (a = b = 3.78 Å, c = 9.51 Å) and each octahedron is in contact with eight neighbours and shares corners.

Rutile is the most thermodynamically stable phase. Rutile still has a tetragonal structure $P4_2/mnm$ (a = b = 4.59 Å, c = 2.96 Å), but it consists of edge-sharing octahedra where each one is in contact with ten nearby octahedra.

Brookite, a meta-stable phase as well as anatase, is made up of both corner and edge sharing octahedra, giving an orthorhombic structure *Pbca* (a = 9.18 Å , b = 5.45 Å, c = 5.15 Å). Two different types of oxygen occur in brookite, deriving from octahedra distortion.

In anatase, greater Ti–Ti distances occur than in rutile (3.79 Å and 3.04 Å vs 3.57 Å and 2.96 Å), while the Ti–O distances are shorter (1.934 and 1.980 Å in anatase vs 1.949 and 1.980 Å in rutile). Thus, different mass densities and electronic band structure result among the three polymorphs [20,21].

$TiO_2$ is an *n*-type semiconductor. The valence band consists of 3d Ti and 2p O states, the conduction band of 3d Ti states. The band gap is 3.20 eV in anatase, 3.02 in rutile and ~3.2 eV in brookite [22–24].

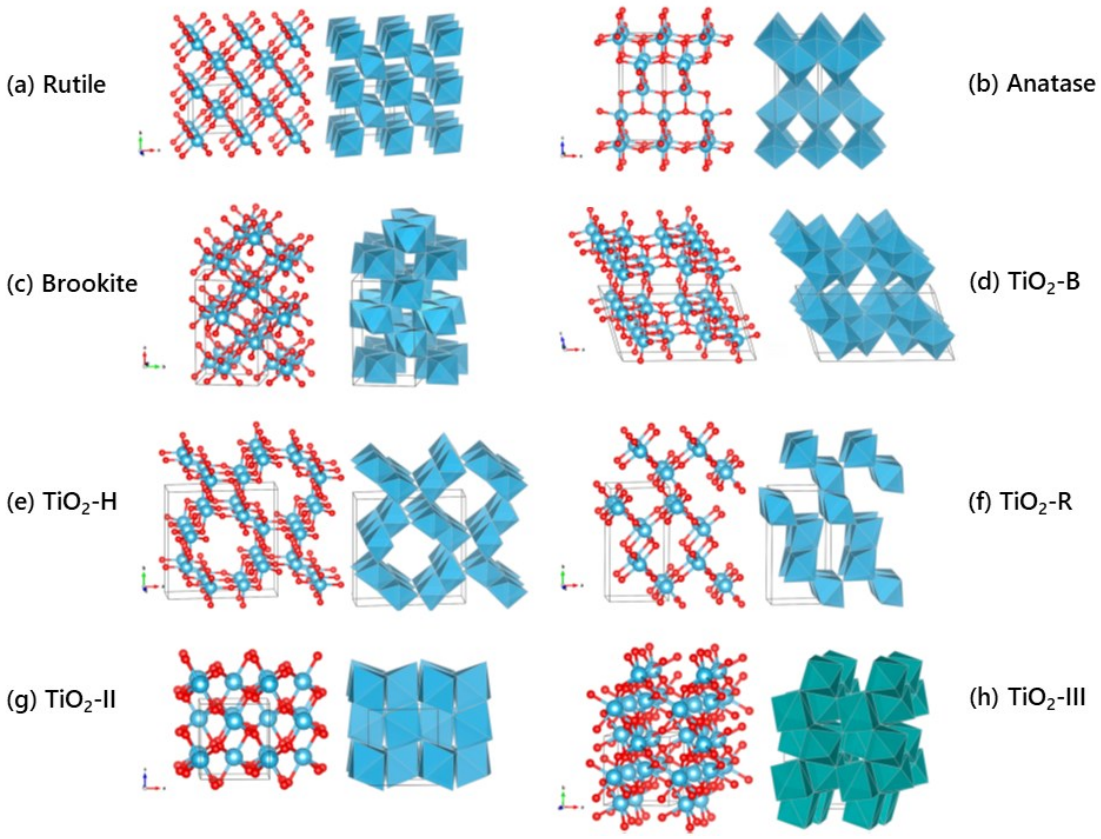


*Figure 1.5 $TiO_6$ octahedra of $TiO_2$ in (a) rutile, (b) anatase, (c) brookite, (d) $TiO_2$-B, (e) $TiO_2$-H, (f) $TiO_2$-R, (g) $TiO_2$-H, (g) $TiO_2$-II, (h) $TiO_2$-III* [18].

*Table 1.1 Structural characteristics of $TiO_2$ polymorphs*

| Structure | Space Group | Density ($g/cm^3$) | Lattice Parameters |
|---|---|---|---|
| Anatase | Tetragonal *$I4_1/amd$* | 3.90 | *a*=3.78 Å, *c*=9.51 Å |
| Rutile | Tetragonal *$P4_2/mnm$* | 4.25 | *a*=4.59 Å, *c*=2.96 Å |
| Brookite | Orthorombic *Pbca* | 4.12 | *a*=9.18 Å, *b*=5.45 Å, *c*=5.15 Å |
| $TiO_2$-B | Monoclinic *C2/m* | 3.73 | *a*=12.18 Å, *b*=3.74 Å, *c*=6.52 Å, β=107.1° |
| $TiO_2$-H | Tetragonal *I4/m* | 3.46 | *a*=10.16 Å, *c*= 2.97 Å |
| $TiO_2$-R | Orthorombic *Pbmn* | 3.87 | *a*=4.90 Å, *b*=9.46 Å, *c*=2.96 Å |
| $TiO_2$-II | Orthorombic *Pbcn* | 4.33 | *a*=4.52 Å, *b*=5.50 Å, *c*=4.94 Å |
| $TiO_2$-III | Monoclinic *$P2_1/c$* | 5.09 | *a*=4.59 Å, *b*=4.85 Å, *c*=4.74 Å β=98.6° |

### 1.3.1 $TiO_2$ synthesis methods

$TiO_2$ nanostructures have been synthesized by using several methods. Among chemical approaches, sol-gel synthesis, hydrothermal and solvothermal processes have been extensively explored. Physical methods to produce $TiO_2$ nanostructures have been also investigated, by using physical vapour deposition, electrodeposition or laser ablation.

The sol-gel process is one of the most widely used techniques. Nanocrystalline materials with high purity in absence of by-products can be obtained. In addition, synthesis conditions usually require low working temperature and the morphology can be tuned controlling the synthesis parameters (pH, reactivity of precursors, complexing agents, catalysts). Sol-gel process usually consists of hydrolysis and condensation reactions to form colloidal suspensions, known as *sol*. Metal alkoxides (e.g. titanium tetraisopropoxide, titanium butoxide) or inorganic metal salts (e.g. titanium chloride, titanium oxysulfate) have been widely used as precursors [25,26]. To improve crystallinity, calcination processes at

high temperature can be carried out after the sol-gel synthesis. Therefore, the final product is influenced by temperature effects, which promote transformation of anatase or brookite into rutile. Coarsening of nanoparticles (NPs) occurs along with the phase transformation and larger nanocrystals size is usually achieved [27].

Hydrothermal syntheses are performed in autoclaves under controlled temperature and pressure conditions. Temperature exceeding 100 °C lead to saturated vapor pressure. Through hydrothermal processes, nanocrystalline titania can be synthesized at moderate temperatures without being affected by large increase in dimension, as in case of calcination procedures [25,26].

Among the three polymorphs, rutile is the most thermodynamically stable at ambient conditions. However, thermodynamic stability depends on crystal size. Zhang and Banfield [28] have demonstrated that there is a critical size (~14 nm) above which the phase transition from anatase to rutile starts. Under that dimension, anatase stability is higher. For that reason, nanostructured synthesized titania is expected to crystallize in anatase phase under this dimension.

## 1.4 $TiO_2$-graphene in energy storage

Electrochemical properties, as described in section 1.1, strongly depend on the structure of the device materials. Effective properties should match one of the main challenging goal of applications: large-scale production.

In graphene, different synthesis methods lead to different structural properties. Bottom-up synthesis can produce high purity graphene, as a *"a flat monolayer of carbon atoms"* [9]. However, since these techniques are affected by high cost and low yield, as-obtained graphene is usually limited to few applications or to fundamental research, which does not need large material amount. In contrast, graphene bulk production can be achieved by other approaches, such as liquid-phase exfoliation and reduction of graphite oxide. Thus, graphene has been explored in EESDs, both in rechargeable batteries and supercapacitors.

Regarding batteries, graphene has been used as anode material in lithium-ion (LIBs) and sodium-ion batteries (SIBs), since it can accommodate ions ($Li^+$ or $Na^+$, respectively). Ions can be adsorbed onto both sides of carbon layer and into pores occurring among layers. In LIBs, graphene drawback consists of solid passivation deposition (solid electrolyte interface, known as *SEI*) onto electrode surface, which worsen electrochemical performance

of the device. The quality of graphene in terms of defects also affects electrochemical properties. If re-stacking occurs, a reduced capacity can be stored over the cycles.

Several strategies to overcome these effects have been undertaken: make a pre-lithiation; control the surface functionalization; combine graphene with other materials into composites. Great attention has been focused on the latter solution, with the attempt of using graphene as a support for other electroactive materials, combining the properties of each species.

To this extent, the combination of graphene and $TiO_2$ results in successful combined anode materials. Titania is also used as anode materials in LIBs and SIBs, as a safe, abundant and chemically stable material. However, its low electrical conductivity requires that a conductive network is formed in $TiO_2$-based anodes. Graphene represents one of the best options to reduce drawbacks related to its use as anode material.

Graphene has been recently employed also in supercapacitors, as electrode material. Its high specific surface area (SSA) makes graphene an attractive electrode material, which is expected to reach outstanding specific capacitance. However, obtaining graphene with theoretical SSA is not trivial. Chemical activation processes, through the formation of a hierarchical porous network, can significantly increase graphene SSA and the subsequent capacity. As well as in rechargeable batteries, graphene composite-based materials are encouraged. Graphene is generally combined to electroactive materials used in pseudocapacitors to improve the specific power of the device. Usually, pseudocapacitive materials exhibit good specific energy but lack in specific power [29]. Among them, $TiO_2$-graphene combined materials have been reported to be effective in improving electrochemical properties of the devices.

In this research, the improvement of electrochemical performance of electrodes materials has been carried out by exploring nanostructured $TiO_2$-graphene properties. Two different approaches have been investigated to synthesize composite materials for LIBs and supercapacitors, respectively. The production of the nanostructured materials by means of scalable and large-scale processes represents a successful feature in employing them in devices. In addition, the composite materials have been obtained by *in situ* growth of nanoparticles onto graphene surface, instead of multi-step processes, which usually combine graphene and NPs (prepared separately) or mix commercial NPs to the carbonaceous material [30,31].

Regarding Li-ion batteries, a thermally exfoliated graphite oxide has been used as graphene material; this in order to take advantage of its defective structure to sustain an *in situ*

synthesis of anatase $TiO_2$ nanoparticles onto graphene surface. The composite material ensures good electrical conductivity to $TiO_2$ and reduces the irreversibility connected to the trapping of $Li^+$ in graphene matrix [32,33].

In supercapacitors, innovative technologies have been examined by using large-scale and cost-effective methods. The goal of simultaneously producing both graphene-based material and anatase $TiO_2$ nanoparticles has been proven as a novel and successful strategy, which ensures higher electrochemical performance than for graphene-based devices [34,35].

The improvement in electrochemical performance resulting from the combination of these materials has been achieved both in Li-ion half cells and in micro-supercapacitors. The structural and electrochemical properties of nanostructured $TiO_2$-graphene will be discussed in the next chapters.

## References


[1] https://www.overshootday.org/, (n.d.). https://www.overshootday.org/ (accessed 30 October 2019).

[2] https://www.nobelprize.org/prizes/chemistry/2019/press-release/, (n.d.). https://www.nobelprize.org/prizes/chemistry/2019/press-release/ (accessed 30 October 2019).

[3] P. Simon, Y. Gogotsi, B. Dunn, Where do Batteries End and Supercapacitors Begin ?, Science (80-. ). 343 (2014) 1210–1211. https://doi.org/10.1126/science.1249625.

[4] P. Simon, Y. Gogotsi, Materials for electrochemical capacitors, Nat. Mater. 7 (2008) 845–854. https://doi.org/10.1038/nmat2297.

[5] G. Zubi, R. Dufo-López, M. Carvalho, G. Pasaoglu, The lithium-ion battery: State of the art and future perspectives, Renew. Sustain. Energy Rev. 89 (2018) 292–308. https://doi.org/10.1016/j.rser.2018.03.002.

[6] X. Luo, J. Wang, M. Dooner, J. Clarke, Overview of current development in electrical energy storage technologies and the application potential in power system operation, Appl. Energy. 137 (2015) 511–536. https://doi.org/10.1016/j.apenergy.2014.09.081.

[7] H. Ibrahim, A. Ilinca, J. Perron, Energy storage systems-Characteristics and comparisons, Renew. Sustain. Energy Rev. 12 (2008) 1221–1250. https://doi.org/10.1016/j.rser.2007.01.023.

[8] Y. Wang, B. Liu, Q. Li, S. Cartmell, S. Ferrara, Z.D. Deng, J. Xiao, Lithium and lithium ion batteries for applications in microelectronic devices: A review, J. Power Sources. 286 (2015) 330–345. https://doi.org/10.1016/j.jpowsour.2015.03.164.

[9] A.K. Geim, K.S. Novoselov, The rise of graphene, Nat. Mater. 6 (2007) 183–191. https://doi.org/10.1038/nnano.2010.224.

[10] P.R. Wallace, The Band Theory of Graphite, Phys. Rev. 71 (1947) 622–634. https://doi.org/10.2208/jsceja.64.452.

[11] A. Castro Neto, The electronic properties of graphene, Rev. Mod. Phys. 81 (2009) 109–162. https://doi.org/10.1103/RevModPhys.81.109.

[12] K.S. Novoselov, A.K. Geim, S.V. Morozov, D. Jiang, M.I. Katsnelson, I.V. Grigorieva, S.V. Dubonos, A.A. Firsov, Two-Dimensional Gas of Massless Dirac Fermions in Graphene, Nature. 438 (2005) 197. https://doi.org/10.1038/nature04233.

[13] E. Rotenberg, A. Bostwick, Superlattice effects in graphene on SiC(0001) and Ir(111) probed by ARPES, Synth. Met. 210 (2015) 85–94. https://doi.org/10.1016/j.synthmet.2015.07.030.

[14] L. Bergamonti, G. Predieri, Y. Paz, L. Fornasini, P.P. Lottici, F. Bondioli, Enhanced self-cleaning properties of N-doped TiO2 coating for Cultural Heritage, Microchem. J. 133 (2017) 1–12. https://doi.org/10.1016/j.microc.2017.03.003.

[15] S. Ding, J.S. Chen, D. Luan, F.Y.C. Boey, S. Madhavi, X.W. Lou, Graphene-supported anatase TiO2 nanosheets for fast lithium storage, Chem. Commun. 47 (2011) 5780–5782. https://doi.org/10.1039/c1cc10687b.

[16] S. Filice, D. D'Angelo, S. Libertino, I. Nicotera, V. Kosma, V. Privitera, S. Scalese, Graphene oxide and titania hybrid Nafion membranes for efficient removal of methyl orange dye from water, Carbon N. Y. 82 (2015) 489–499.

https://doi.org/10.1016/j.carbon.2014.10.093.
[17] D. Wang, D. Choi, J. Li, Z. Yang, Z. Nie, R. Kou, D. Hu, C. Wang, L. V Saraf, J. Zhang, I.A. Aksay, J. Liu, Self-Assembled TiO2–Graphene Hybrid Nanostructures for Enhanced Li-Ion Insertion, ACS Nano. 3 (2009) 907–914. https://doi.org/10.1021/nn900150y.
[18] H. Zhang, J.F. Banfield, Structural characteristics and mechanical and thermodynamic properties of nanocrystalline TiO2, Chem. Rev. 114 (2014) 9613–9644. https://doi.org/10.1021/cr500072j.
[19] G.R. Hearne, J. Zhao, A.M. Dawe, V. Pischedda, M. Maaza, M.K. Nieuwoudt, P. Kibasomba, O. Nemraoui, J.D. Comins, M.J. Witcomb, Effect of grain size on structural transitions in anatase TiO2:A Raman spectroscopy study at high pressure, Phys. Rev. B. 70 (2004) 134102. https://doi.org/10.1103/PhysRevB.70.134102.
[20] J.K. Burdett, T. Hughbanks, G.J. Miller, J. V. Smith, J.W. Richardson, Structural-Electronic Relationships in Inorganic Solids: Powder Neutron Diffraction Studies of the Rutile and Anatase Polymorphs of Titanium Dioxide at 15 and 295 K, J. Am. Chem. Soc. 109 (1987) 3639–3646. https://doi.org/10.1021/ja00246a021.
[21] M. Pelaez, N.T. Nolan, S.C. Pillai, M.K. Seery, P. Falaras, A.G. Kontos, P.S.M. Dunlop, J.W.J. Hamilton, J.A. Byrne, K. O'Shea, M.H. Entezari, D.D. Dionysiou, A review on the visible light active titanium dioxide photocatalysts for environmental applications, Appl. Catal. B Environ. 125 (2012) 331–349. https://doi.org/10.1016/j.apcatb.2012.05.036.
[22] X. Chen, S.S. Mao, Titanium dioxide nanomaterials: Synthesis, properties, modifications and applications, Chem. Rev. 107 (2007) 2891–2959. https://doi.org/10.1021/cr0500535.
[23] A.L. Linsebigler, G. Lu, J.T. Yates, Photocatalysis on TiO2 Surfaces: Principles, Mechanisms, and Selected Results, Chem. Rev. 95 (1995) 735–758. https://doi.org/10.1021/cr00035a013.
[24] R. López, R. Gómez, Band-gap energy estimation from diffuse reflectance measurements on sol-gel and commercial TiO 2: A comparative study, J. Sol-Gel Sci. Technol. 61 (2012) 1–7. https://doi.org/10.1007/s10971-011-2582-9.
[25] C.C. Wang, J.Y. Ying, Sol-gel synthesis and hydrothermal processing of anatase and rutile titania nanocrystals, Chem. Mater. 11 (1999) 3113–3120. https://doi.org/10.1021/cm990180f.
[26] M.T. Noman, M.A. Ashraf, A. Ali, Synthesis and applications of nano-TiO2 : a review, Environ. Sci. Pollut. Res. 26 (2019) 3262–3291. https://doi.org/10.1007/s11356-018-3884-z.
[27] D. Bersani, G. Antonioli, P.P. Lottici, T. Lopez, Raman study of nanosized titania prepared by sol-gel route, J. Non. Cryst. Solids. 232–234 (1998) 175–181. https://doi.org/10.1016/S0022-3093(98)00489-X.
[28] H. Zhang, J.F. Banfield, Understanding polymorphic phase transformation behavior during growth of nanocrystalline aggregates: Insights from TiO2, J. Phys. Chem. B. 104 (2000) 3481–3487. https://doi.org/10.1021/jp000499j.
[29] R. Raccichini, A. Varzi, S. Passerini, B. Scrosati, The role of graphene for electrochemical energy storage, Nat. Mater. 14 (2015) 271–279. https://doi.org/10.1038/nmat4170.

[30] L. Jiang, Z. Ren, S. Chen, Q. Zhang, X. Lu, H. Zhang, G. Wan, Bio-derived three-dimensional hierarchical carbon-graphene-TiO2 as electrode for supercapacitors, Sci. Rep. 8 (2018) 1–9. https://doi.org/10.1038/s41598-018-22742-7.

[31] S. Wang, Z.S. Wu, S. Zheng, F. Zhou, C. Sun, H.M. Cheng, X. Bao, Scalable Fabrication of Photochemically Reduced Graphene-Based Monolithic Micro-Supercapacitors with Superior Energy and Power Densities, ACS Nano. 11 (2017) 4283–4291. https://doi.org/10.1021/acsnano.7b01390.

[32] M. Madian, A. Eychmüller, L. Giebeler, Current advances in TiO2-based nanostructure electrodes for high performance lithium ion batteries, Batteries. 4 (2018). https://doi.org/10.3390/batteries4010007.

[33] J.C. Pramudita, D. Pontiroli, G. Magnani, M. Gaboardi, M. Riccò, C. Milanese, H.E.A. Brand, N. Sharma, Graphene and Selected Derivatives as Negative Electrodes in Sodium- and Lithium-Ion Batteries, ChemElectroChem. 2 (2015) 600–610. https://doi.org/10.1002/celc.201402352.

[34] M.F. El-Kady, R.B. Kaner, Scalable fabrication of high-power graphene micro-supercapacitors for flexible and on-chip energy storage, Nat. Commun. 4 (2013) 1475–1479. https://doi.org/10.1038/ncomms2446.

[35] L.L. Jiang, X. Lu, C.M. Xie, G.J. Wan, H.P. Zhang, T. Youhong, Flexible, free-standing TiO2-graphene-polypyrrole composite films as electrodes for supercapacitors, J. Phys. Chem. C. 119 (2015) 3903–3910. https://doi.org/10.1021/jp511022z.

# 2 Li-ion batteries

Batteries are electrochemical energy storage devices (EESDs) which can store energy through the transformation of electric energy into chemical energy and convert it back into electrical energy when required.

Two types of batteries are distinguished: primary and secondary batteries. Primary batteries can work until the electrochemical reaction occurs during the discharge process. Since the reaction is not reversible, primary batteries could not be recharged. Conversely, secondary batteries, also called *rechargeable batteries* or *accumulators*, are devices which can be cycled by discharge and charge processes where the conversion of chemical energy to electrical energy and back is nearly completely reversible.

Rechargeable batteries are currently of great interest as power sources in portable electronic devices and electric vehicles. Meeting the demand of a high energy density and a long life-cycle, Li-ion batteries (LIBs) are the current technology both in electronics and in automotive sectors, as they are widely used for laptops, smartphones, tablets and wearable computers as well as for electric vehicles and hybrid electric vehicles. In addition, rechargeable LIBs have great potential in being used for power supply systems, which need to store energy.

Lithium is a promising element due to its lowest reduction potential (-3.04 V vs SHE, Standard hydrogen electrode) and to its lightest atomic weight (6.94 g/mol) and specific gravity (0.53 g/cm$^3$) [1]. However, safety concerns regarding the use of lithium in LIBs have to be considered. If overcharge or short circuits occur in the cell, the heating effect can lead to the battery burning or explosion [2,3].

## 2.1 Basic principles of Li-ion batteries

Li-ion batteries (LIBs) consist of mainly three parts: an anode (negative electrode), a cathode (positive electrode) and an electrolyte solution soaking a separator between them. The separator electrically insulates the electrodes, preventing a short circuit, but allows the diffusion of ions from one electrode to the other. To keep charge conservation, the electrodes are connected to an external circuit where the transport of the resulting electrons can provide the current flow.

The cathode consists of materials with a more positive redox potential than that of anode materials. In LIBs, cathodes are made of lithium containing materials, such as lithium transition metal oxides or lithium transition metal phosphates.

The anode is made of materials which can intercalate ions, in this case $Li^+$, and typically consist of carbonaceous materials. First, graphite has been extensively used. Recently, great interest has been found in carbon-based composite materials.

The electrolyte is a solution containing lithium salts in organic solvents and plays a fundamental role of promoting the mobility of Li ions. The electrolyte solution is soaking a membrane, called separator, which is usually made of polymers (e.g. polyethylene and polypropylene). The separator prevents direct electric contact between the electrodes, while it is permeable to Li ions.

In LIBs, the electrochemical reactions involve oxidation and reduction processes occurring at the electrodes with a transfer of Li ions between them. Specifically, during the discharge process, lithium ions migrate from the anode through the electrolyte solution to the cathode, while electrons pass into the external circuit (figure 2.1). During the charge process, an external electric current flows in the opposite direction to restore the chemical energy form the electric energy. In the cell, lithium ions are extracted from the cathode, they diffuse into the electrolyte and they are re-intercalated into the anode.

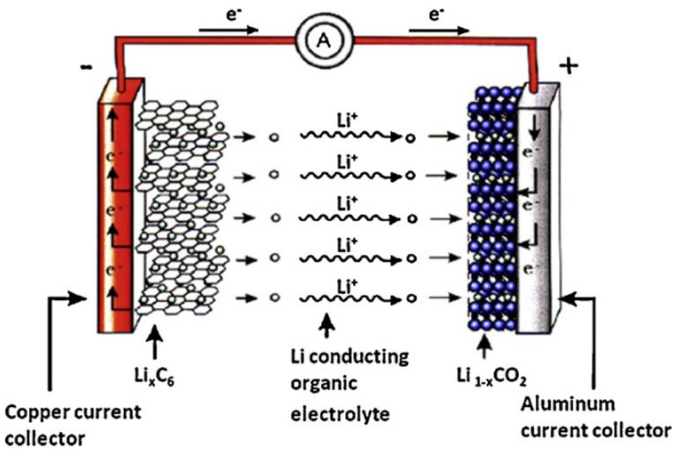


*Figure 2.1 Schematic representation of the discharge process in a lithium-ion battery* [4].

Good performance in a rechargeable battery is achieved with high energy density, high efficiency and a long life-cycle.

The energy density, namely the energy per unit mass, depends on the cell voltage and on the capacity of battery, which is defined as the overall stored charge quantity. High energy density is obtained maximizing these parameters. Lithium ion batteries can be cycled up to ~4 V and energy density of 100-150 Wh/kg can be achieved [4].

The reversibility of the electrochemical reactions is crucial in determining the efficiency. High efficiency is reached when the intercalation and the de-intercalation processes are highly reversible. Thus, rechargeable LIBs should be able to be cycled for hundreds of cycles.

## 2.2 Electrochemical reactions in LIBs

In LIBs, the electrochemical reactions involve reduction and oxidation processes occurring at the electrodes. Lithium ions migrate between anode and cathode, without the formation of metallic lithium in the system. During charging, lithium ions are extracted from the positive electrode and pass through the electrolyte, while electrons move from the cathode to the anode through the external circuit. Thus, oxidation occurs in the cathode. As the positive electrode usually consists of lithium containing transition metal oxides (abbreviated as $LiMO_2$), the reaction can be expressed as follows:

$$LiMO_2 \rightarrow Li_{1-x}MO_2 + xLi^+ + xe^- \quad (2.1)$$

Conversely, in the anode, which usually contains carbon-based materials (*C*), reduction reaction occurs according to the:

$$C + xLi^+ + xe^- \rightarrow Li_xC \quad (2.2)$$

The overall reaction can be condensed by the:

$$LiMO_2 + C \rightarrow Li_{1-x}MO_2 + Li_xC \quad (2.3)$$

During discharging, the battery is connected to a load which receives electric energy through the reversed reactions occurring in the electrodes, with migration of lithium and electrons in the opposite direction in the system [5].

## 2.3 Cathode materials

Cathodes are made of materials which can reversibly and quickly intercalate and release lithium to obtain high efficiency and high energy density. Since the reaction occurs at the electrode/electrolyte interface, a fast transport of the ions can be achieved tuning the morphology and the morphometry of the cathode materials. Usually, micro-sized particles are preferred, while the desired shape is mostly influenced by the structure of the material (e.g. isotropic or layered structure). The surface morphology and the porosity of the electrode are also fundamental in the access of the electrolyte.

The first investigated group of cathode materials consists of layered dichalcogenides, whose compact structure ensures high energy stored per unit volume. Among them, titanium disulphide ($TiS_2$) has been one of the most examined cathodes, thanks to its lightness and the reversible intercalation of lithium without phase changes. Up to 1000 cycles with small capacity loss can be achieved in $TiS_2$-containing cells. Other dichalcogenides have been investigated, such as vanadium diselenide ($VSe_2$) and molybdenum disulfide ($MoS_2$). Besides, trichalcogenides have been reported, such as triselenide of niobium ($NbSe_3$). However, some of them lack of lithium reversibility [6].

Then, the interest in cathode materials has been moved to layered oxides, which have similar structure to layered dichalcogenides. Lithium cobalt oxide ($LiCoO_2$) is the most widely used material in cathodes [7]. However, due to the high cobalt cost, alternatives have been studied. Additionally, $LiCoO_2$ chemical stability is a crucial issue, which can lead to dissolution of cobalt into the electrolyte when lithium is de-intercalated from the cathode during the charge process. As lithium content varies in $LiCoO_2$, lattice parameters changes occur, affecting the structural stability. Lithium nickel oxide ($LiNiO_2$) and lithium manganese oxides ($LiMnO_2$ and $LiMn_2O_4$) have been explored to reduce costs and toxicity and to enhance electrochemical cathode performance. Since lithium intercalation and de-intercalation are strongly influenced by which site lithium occupies in the crystallographic structure of cathode material, lithium paths can be inhibited by a less ordered structure. To overcome drawbacks of different cathode materials, combination of two electrode compounds can improve the performance, creating a composite cathode (e.g. $Li(Ni,Mn,Co)O_2$). Additionally, as a different class of materials, the multiple valences of vanadium oxides make $V_2O_5$ and $LiV_3O_8$ suitable for cathodes. Furthermore, lithium phosphates ($LiMPO_4$, *M* being a transition metal) are attracting cathode materials, being $LiFePO_4$ the most widely investigated. To obtain high performance, the electrical conductivity of cathodes can be improved by adding conductive phases, such as carbon-based materials. Electrons can pass through the electrode in the conductive network, meanwhile lithium access is not prevented. Regarding the architecture of cathodes, thin-film deposition has been encouraged, due to the increasing demand in miniaturization in micro-devices [8].

## 2.4 Electrolytes and separators

In LIBs, the electrolyte has the fundamental role of promoting the migration of Li ions through the electrolyte solution from the anode to the cathode and vice versa. Electrolytes must have the following properties: (1) high ionic conductivity, (2) low electronic conductivity, (3) wide thermal, chemical and electrochemical stability, (4) low reactivity with the other elements of the battery, (5) safety and low toxicity.

Electrolytes can be divided into three groups: liquid, solid and polymer electrolytes.

Liquid electrolytes consist of lithium salts dissolved in organic solvents. To obtain high ionic conductivity, the lithium salts should be easily dissolved into a high polar organic solvent. The solvent should also have a good stability at negative potentials, to avoid reactions with metallic lithium. The most extensively used organic solvents in LIBs are alkyl carbonates, as

ethylene carbonate (EC), propylene carbonate (PC), dimethyl carbonate (DMC) and diethyl carbonate (DEC). Mixtures of organic solvents are usually adopted to combine the required properties. Among lithium salts, the monovalent anions are preferred, in order to obtain a high degree of salt dissociation. The ionic conductivity is in the range of 1-10 mS/cm. Lithium hexafluorophosphate ($LiPF_6$) is one of the most widely used, followed by lithium hexafluoroarsenate ($LiAsF_6$), lithium tetrafluoroborate ($LiBF_4$) and lithium perchlorate ($LiClO_4$) [9].

Solid electrolytes are good ionic conductors at room temperature, even if lower ionic conductivity is usually obtained than for liquid electrolytes (~$10^{-4}$-$10^{-7}$ S/cm). However, solid electrolytes are preferred in terms of safety, thanks to the low flammability and toxicity. They consist of crystalline materials, as lithium halides and lithium oxysalts or lithium ion conductive glassy materials.

Polymer electrolytes can match liquid and solid electrolytes properties above room temperature. They should both promote lithium diffusivity and create a flexible structure without electrolyte leakage. To obtain polymer electrolytes, lithium salts are combined with polymer matrices, including poly(ethylene oxide) (PEO), poly(propylene oxide) (PPO), poly(acrylonitrile) (PAN), poly(methyl methacrylate) (PMMA), poly(vinyl chloride) (PVC) and poly(vinylidene fluoride) (PVDF) [10].

Between the anode and the cathode, the separator is soaked by the electrolyte solution. The separator is a component of the battery which, even if it does not have an active function in the electrochemical reaction, should respond to two requirements: (1) to separate the electrodes one from each other, to prevent a short circuit from electronic contact and (2) to promote the transfer of ions between the electrodes. Suitable materials for separators are porous electronic insulator materials. Usually, the commercially available materials consist of microporous membrane of polymers, such as polypropylene, polyethylene or their combinations [5].

## 2.5 Anode materials

Anode materials should satisfy the following requirements: (1) low volume changes during the discharge and charge processes, which can lead to contraction and expansion of the electrode structure; (2) high electrical conductivity, to promote fast charge transfer; (3) safe and cost-effective materials.

### 2.5.1 Metallic lithium

Metallic lithium has been investigated as anode material at the beginning of rechargeable batteries *era*, thanks to its high energy density and its outstanding specific capacity (3860 mAh/g). However, the major drawback of using pure lithium is the dendritic formation during cycling, causing internal short circuit between the electrodes, leading to poor cyclability and safety concerns for the cell. In addition, volume changes from large lithium intercalation can lead to degradation, resulting in reduced electrical contacts within the electrode materials [1]. To minimize risks and drawbacks associated to the use of lithium, several strategies have been explored.

### 2.5.2 Carbonaceous materials

Carbon-based materials are one of the most investigated compounds in anodes to replace lithium. According to the equation 2.2, lithium can be inserted into several carbonaceous materials as anodes. However, the electrochemical potential is typically close to the reduction potential of lithium, resulting in the formation of lithium dendrites which give rise to safety concerns and cyclability issues (figure 2.2) [9,11]. Among carbonaceous materials, graphite has received much attention, thanks to its high specific capacity (372 mAh/g) with lithium intercalation up to the formation of $LiC_6$. However, graphite exhibits appreciable irreversibility and consequent deterioration of cells. Irreversibility refers to the fraction of charge which can not be recovered after the first discharge cycle in the subsequent charge process (figure 2.3). In graphite, the insertion and the extraction of lithium occur at potential lower than 0.25 V (vs $Li/Li^+$). At this low potential, the formation of a solid electrolyte interface (SEI) is observed, consisting in a solid layer on the graphite surface, which occurs in the first discharge/charge cycles. As lithium reacts with nearby anions from the electrolyte, a solid film containing Li salts is deposited on the electrode. Thus, the irreversibility is related to the formation of SEI, which is insoluble and prevent lithium de-intercalation and re-intercalation in the subsequent cycles [12]. In addition, significant volume changes in terms of expansion and contraction occur in graphite during insertion and extraction of lithium, which lead to deterioration effects in the electrode, reducing the electrochemical performance [13].

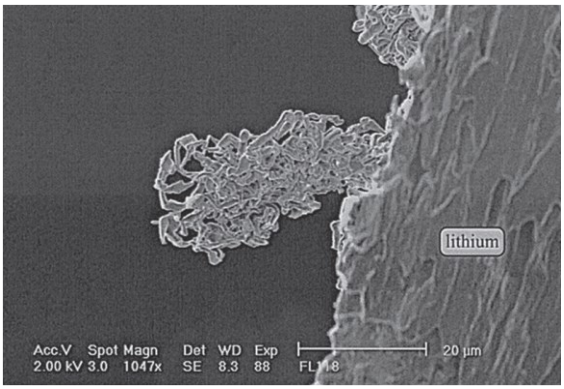


*Figure 2.2 SEM image of lithium dendrite on anode surface after the first charge* [11].

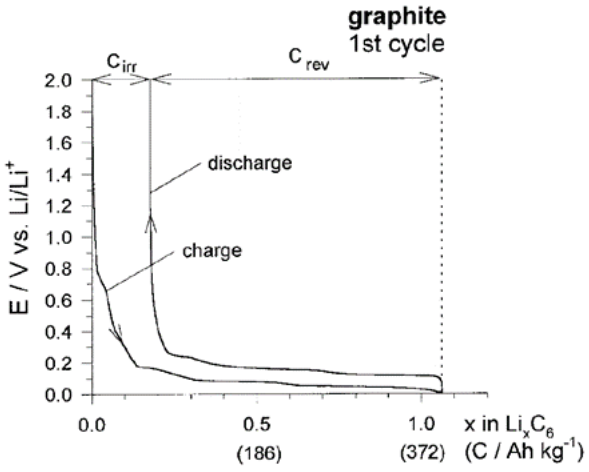


*Figure 2.3 Galvanostatic discharge and charge curves of graphite. $C_{irr}$ refers to the irreversible specific charge, $C_{rev}$ to the reversible specific charge* [13].

Therefore, the attempt in employing other carbonaceous materials is currently of great interest. Among them, fullerenes, carbon nanotubes and graphene have been widely investigated in LIBs [14–17]. Graphene has been considered as an attractive material, thanks to its high theoretical specific surface area (~2630 $m^2/g$), since lithium can be stored on both sides of each carbon layer. Much higher specific capacity is reached in graphene-based electrodes, up to over 3000 mAh/g [14]. Though, the irreversible behaviour is still observed, rising from the formation of SEI on graphene surface. To overcome irreversibility issues, further strategies have been attempted, combining pristine graphene into composite anodes.

Metal oxides (such as $TiO_2$, $Fe_3O_4$, $V_2O_5$, CuO, NiO, FeO) are expected to be good candidates thanks to their abilities to intercalate/de-intercalate lithium at higher potential, with reduction/oxidation reactions of the metal species [18–21]. In addition, they usually have high abundancy, low cost, low toxicity and good chemical stability. Thus, combining graphene with nanostructured metal oxides can improve the electrochemical performance of LIBs [15]. Nanostructures are preferred since their large surface-to-volume ratio can provide innumerable electroactive sites for storing lithium and reduce the lithium transport lengths, enhancing the charge/discharge rates [19]. However, one of the main drawbacks of metal oxides is the low electrical conductivity which inhibits a rapid charge transfer. To this extent, graphene can create a conductive structure among metal oxides nanoparticles, ensuring fast electrons transfer. In addition, the high specific surface area of graphene provides an extensive distribution of nanoparticles, reducing their agglomeration at the same time [15,22,23]. Furthermore, graphene can solve problems connected to the volume changes thanks to its flexibility to accommodate expansions or contractions of the nanostructured materials [24].

### 2.5.3 Titanium-based materials

To overcome issues related to carbon-based anodes, additional materials which can intercalate/de-intercalate lithium ions have been suggested. Lithium titanate ($Li_4Ti_5O_{12}$, known as *LTO*) is currently used as anode material, also in commercial LIBs. In LTO, having a spinel structure, lithium storage occurs at ~1.5 V (vs $Li/Li^+$) with reduction of $Ti^{4+}$ into $Ti^{3+}$, according to the reactions:

$$\mathrm{Li_4Ti_5O_{12}} + 3\mathrm{Li^+} + 3\mathrm{e^-} \leftrightarrow \mathrm{Li_7Ti_5O_{12}} \qquad (2.4)$$

Each mol of $Li_4Ti_5O_{12}$ can accommodate up to 3 mol of $Li^+$, giving rise to a theoretical specific capacity of 175 mAh/g. One of the main advantages of LTO is the structural stability, which determines a hardly noticeable volume change (<0.5 %), thanks to the similar size of $Li^+$ and its sites in LTO. As a result, LTO based anodes can ensure good rate capability and long life-cycle to the cells. Though, it is worth noting that, due to the higher intercalation potential of LTO compared to that of graphite, higher potential is required for cathode materials combining with LTO, in order to obtain a considerable voltage window [25].

Furthermore, titanium dioxide ($TiO_2$) has been explored as anode material in LIBs. Safety concerns are solved by its high thermal and chemical stability, environmental compatibility and low toxicity. Among the eight $TiO_2$ polymorphs, anatase, rutile and $TiO_2$-B exhibit good

electrochemical behaviour [26–28]. Interstitial sites of $TiO_2$ are reported to accommodate lithium, as depicted in figure 2.4 [29]. Rutile shows negligible intercalated lithium content at room temperature, but the intercalation increases with temperature [30]. Anatase offers its $TiO_6$ zigzag channels as possible paths for lithium. A phase transition is also expected during the intercalation, from the orthorhombic distortion caused by Li-Li repulsion. The anatase crystal structure change consists of a slight reduction of the *c*-axis and an expansion of the *b*-axis. However, the overall volume change is low (<4%) [31]. $TiO_2$-B, having longer Ti-O bond distances (~2.2-2.5 Å) than anatase and rutile (~1.9-2.0 Å), can host lithium without deformation of the lattice [32].

Lithium can be inserted/extracted at ~1.7-1.9 V (vs $Li/Li^+$) with reduction of $Ti^{4+}$ into $Ti^{3+}$, according to the reactions:

$$TiO_2 + x\,Li^+ + x\,e^- \leftrightarrow Li_xTiO_2 \qquad (2.5)$$

$$0 \leq x \leq 1$$

Each $TiO_2$ mol can accommodate up to 1 mol of $Li^+$, giving rise to a theoretical specific capacity of 336 mAh/g. However, in order that the reaction is completely reversible, the maximum obtained value is x=0.5, corresponding to a capacity of 168 mAh/g [29,33,34]. Since the performance of $TiO_2$ are strongly related to the morphology and the size of nanostructures, good effort has been made to obtain promising nanostructured $TiO_2$ anodes. During coarsening of nanocrystalline $TiO_2$, surface free energy constitutes a large part of the total free energy involved in the transformation. It has been demonstrated by Zhang and Banfield [35] that the critical size at which anatase starts to transform to rutile is around 14-16 nm. According to that, anatase is more stable than rutile when the particle size decreases below that value. In batteries, since reduced nanocrystal dimensions are preferred for improving the electrochemical performance, anatase results as the favourite candidate among the $TiO_2$ polymorphs.

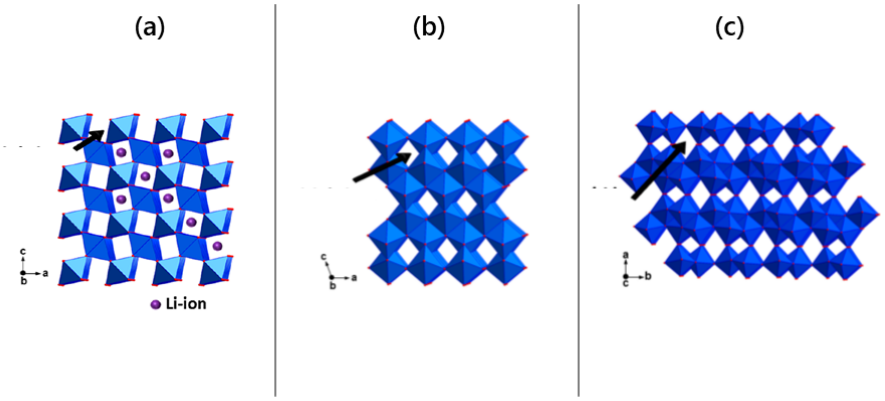


*Figure 2.4 Structure of (a) rutile, (b) anatase and (c) $TiO_2$-B. Interstitial sites which can accommodate lithium are highlighted by black arrows* [29].

Though, the main drawback is the low electrical conductivity, which requires the combination of $TiO_2$ to a conductive phase. Great interest is currently addressed to produce nanostructured combined materials based on $TiO_2$ and graphene. Combining defective graphenes to nanostructured titania has been reported as a successful strategy to improve the electrochemical performance of LIBs. The growth of nanostructures is expected to be promoted by the presence of reactive defects of graphene surface. Therefore, a widely distribution of nanostructures on graphene can improve the Li intercalation/extraction, thanks to the conductive network created by graphene [22,29,36–38].

## 2.6 From research to a successful application

The growing interest in developing successfully materials as anodes in LIBs has led to a wide investigation of graphene-based composite materials and their properties to overcome drawbacks related to cyclability and safety. The combination of graphene advantages, in terms of high electrical conductivity and flexibility, with the electrochemical performance of transition metal oxides, has proven to be effective in increasing the electrochemical properties of LIBs, in terms of cyclability, life-cycle and safety conditions. Among transition metal oxides, $TiO_2$ is a promising candidate, thanks to its low toxicity, chemical stability and abundancy. Anatase is expected to be the best option, since nanocrystals synthesis with the smallest size usually gives anatase particles.

The research presented here has been focused on the production of composite $TiO_2$-graphene nanostructured materials to be tested in lithium-ion half-cells. A thermally exfoliated graphite oxide has been used as graphene material, to take advantage of the defective structure for an *in situ* synthesis of anatase $TiO_2$ nanoparticles onto graphene surface. The improvement in electrochemical performance thanks to the presence of graphene will be discussed in the next chapters.

## References


[1] J.M. Tarascon, M. Armand, Issues and challenges facing rechargeable lithium batteries, Nature. 414 (2001) 359–367. https://doi.org/10.1142/9789814317665_0024.

[2] J. Wen, Y. Yu, C. Chen, A review on lithium-ion batteries safety issues: Existing problems and possible solutions, Mater. Express. 2 (2012) 197–212. https://doi.org/10.1166/mex.2012.1075.

[3] G. Zubi, R. Dufo-López, M. Carvalho, G. Pasaoglu, The lithium-ion battery: State of the art and future perspectives, Renew. Sustain. Energy Rev. 89 (2018) 292–308. https://doi.org/10.1016/j.rser.2018.03.002.

[4] B. Scrosati, J. Garche, Lithium batteries: Status, prospects and future, J. Power Sources. 195 (2010) 2419–2430. https://doi.org/10.1016/j.jpowsour.2009.11.048.

[5] Jurgen O. Besenhard, Hand book of battery material, John Wiley & Sons, 1999.

[6] M.S. Whittingham, Lithium Batteries and Cathode Materials, Chem. Rev. 104 (2004) 4271–4302. https://doi.org/10.1021/acs.chemmater.7b00809.

[7] K. Mizushima, P.C. Jones, P.J. Wiseman, J.B. Goodenough, LixCoO2 (0<x<-1): A new cathode material for batteries of high energy density, Mater. Res. Bull. 15 (1980) 783–789. https://doi.org/10.1016/0025-5408(80)90012-4.

[8] J.W. Fergus, Recent developments in cathode materials for lithium ion batteries, J. Power Sources. 195 (2010) 939–954. https://doi.org/10.1016/j.jpowsour.2009.08.089.

[9] W. Van Schalkwijk, B. Scrosati, Advances in Lithium-Ion Batteries, Springer, 2002.

[10] A.M. Stephan, Review on gel polymer electrolytes for lithium batteries, Eur. Polym. J. 42 (2006) 21–42. https://doi.org/10.1016/j.eurpolymj.2005.09.017.

[11] F. Orsini, A. Du Pasquier, B. Beaudoin, J.M. Tarascon, M. Trentin, N. Langenhuizen, E. De Beer, P. Notten, In situ Scanning Electron Microscopy (SEM) observation of interfaces within plastic lithium batteries, J. Power Sources. 76 (1998) 19–29. https://doi.org/10.1016/S0378-7753(98)00128-1.

[12] E. Peled, S. Menkin, Review — SEI : Past , Present and Future, 164 (2017). https://doi.org/10.1149/2.1441707jes.

[13] M. Winter, J.O. Besenhard, M.E. Spahr, P. Novak, Insertion electrode materials for rechargeable lithium batteries, Adv. Mater. 10 (1998) 725–763. https://doi.org/10.1002/(SICI)1521-4095(199807)10:10<725::AID-ADMA725>3.0.CO;2-Z.

[14] J.C. Pramudita, D. Pontiroli, G. Magnani, M. Gaboardi, M. Riccò, C. Milanese, H.E.A. Brand, N. Sharma, Graphene and Selected Derivatives as Negative Electrodes in Sodium- and Lithium-Ion Batteries, ChemElectroChem. 2 (2015) 600–610. https://doi.org/10.1002/celc.201402352.

[15] X. Huang, Z. Zeng, Z. Fan, J. Liu, H. Zhang, Graphene-based electrodes, Adv. Mater. 24 (2012) 5979–6004. https://doi.org/10.1002/adma.201201587.

[16] J.A. Teprovich, J.A. Weeks, P.A. Ward, S.C. Tinkey, C. Huang, J. Zhou, R. Zidan, P. Jena, Hydrogenated C 60 as High-Capacity Stable Anode Materials for Li Ion Batteries, ACS Appl. Energy Mater. 2 (2019) 6453–6460. https://doi.org/10.1021/acsaem.9b01040.

[17] B.J. Landi, M.J. Ganter, C.D. Cress, R.A. DiLeo, R.P. Raffaelle, Carbon nanotubes for lithium ion batteries, Energy Environ. Sci. 2 (2009) 638–654.

https://doi.org/10.1039/b904116h.
[18] V. Aravindan, Y.S. Lee, R. Yazami, S. Madhavi, TiO2 polymorphs in 'rocking-chair' Li-ion batteries, Mater. Today. 18 (2015) 345–351. https://doi.org/10.1016/j.mattod.2015.02.015.
[19] A.S. Aricò, P. Bruce, B. Scrosati, J.-M. Tarascon, W. Van Schalkwijk, Nanostructured materials for advanced energy conversion and storage devices:, Nat. Mater. Mater. 4 (2005) 366–377. https://doi.org/10.1007/978-3-662-56364-9_18.
[20] P.L. Taberna, S. Mitra, P. Poizot, P. Simon, J.M. Tarascon, High rate capabilities Fe3O4-based Cu nano-architectured electrodes for lithium-ion battery applications, Nat. Mater. 5 (2006) 567–573. https://doi.org/10.1038/nmat1672.
[21] C.J. Patrissi, C.R. Martin, Improving the Volumetric Energy Densities of Nanostructured V 2O 5 Electrodes Prepared Using the Template Method, J. Electrochem. Soc. 148 (2001) 1247–1253. https://doi.org/10.1149/1.1407831.
[22] D. Wang, D. Choi, J. Li, Z. Yang, Z. Nie, R. Kou, D. Hu, C. Wang, L. V Saraf, J. Zhang, I.A. Aksay, J. Liu, Self-Assembled TiO2–Graphene Hybrid Nanostructures for Enhanced Li-Ion Insertion, ACS Nano. 3 (2009) 907–914. https://doi.org/10.1021/nn900150y.
[23] D. Wang, R. Kou, D. Choi, Z. Yang, Z. Nie, J. Li, L. V. Saraf, D. Hu, J. Zhang, G.L. Graff, J. Liu, M.A. Pope, I.A. Aksay, Ternary self-assembly of ordered metal oxide-graphene nanocomposites for electrochemical energy storage, ACS Nano. 4 (2010) 1587–1595. https://doi.org/10.1021/nn901819n.
[24] G. Zhou, D.W. Wang, F. Li, L. Zhang, N. Li, Z.S. Wu, L. Wen, G.Q. Lu, H.M. Cheng, Graphene-wrapped Fe 3 O 4 anode material with improved reversible capacity and cyclic stability for lithium ion batteries, Chem. Mater. 22 (2010) 5306–5313. https://doi.org/10.1021/cm101532x.
[25] C.P. Sandhya, B. John, C. Gouri, Lithium titanate as anode material for lithium-ion cells: A review, Ionics (Kiel). 20 (2014) 601–620. https://doi.org/10.1007/s11581-014-1113-4.
[26] J. Wang, J. Polleux, J. Lim, B. Dunn, Pseudocapacitive contributions to electrochemical energy storage in TiO 2 (anatase) nanoparticles, J. Phys. Chem. C. 111 (2007) 14925–14931. https://doi.org/10.1021/jp074464w.
[27] M.O. Guler, O. Cevher, T. Cetinkaya, U. Tocoglu, H. Akbulut, High capacity TiO2 anode materials for Li-ion batteries, Energy Convers. Manag. 72 (2013) 111–116. https://doi.org/10.1016/j.enconman.2012.11.026.
[28] A.R. Armstrong, G. Armstrong, J. Canales, P.G. Bruce, TiO 2 -B nanowires, Angew. Chemie - Int. Ed. 43 (2004) 2286–2288. https://doi.org/10.1002/anie.200353571.
[29] M. Madian, A. Eychmüller, L. Giebeler, Current advances in Tio 2 -based nanostructure electrodes for high performance lithium ion batteries, Batteries. 4 (2018). https://doi.org/10.3390/batteries4010007.
[30] M.V. Koudriachova, N.M. Harrison, de L. S.W., Diffusion of Li-ions in rutile. An ab initio study, Solid State Ionics. 157 (2003) 35–38. https://doi.org/10.1103/PhysRevB.71.214109.
[31] M. Wagemaker, G.J. Kearley, A.A. Van Well, H. Mutka, F.M. Mulder, Multiple Li positions inside oxygen octahedra in lithiated TiO2 anatase, J. Am. Chem. Soc. 125 (2003) 840–848. https://doi.org/10.1021/ja028165q.

[32] Z. Yang, D. Choi, S. Kerisit, K.M. Rosso, D. Wang, J. Zhang, G. Graff, J. Liu, Nanostructures and lithium electrochemical reactivity of lithium titanites and titanium oxides: A review, J. Power Sources. 192 (2009) 588–598. https://doi.org/10.1016/j.jpowsour.2009.02.038.

[33] P. Kubiak, T. Fröschl, N. Hüsing, U. Hörmann, U. Kaiser, R. Schiller, C.K. Weiss, K. Landfester, M. Wohlfahrt-Mehrens, TiO2 anatase nanoparticle networks: Synthesis, structure, and electrochemical performance, Small. 7 (2011) 1690–1696. https://doi.org/10.1002/smll.201001943.

[34] J.Y. Shin, D. Samuelis, J. Maier, Sustained lithium-storage performance of hierarchical, nanoporous anatase TiO2 at high rates: Emphasis on interfacial storage phenomena, Adv. Funct. Mater. 21 (2011) 3464–3472. https://doi.org/10.1002/adfm.201002527.

[35] H. Zhang, J.F. Banfield, Understanding polymorphic phase transformation behavior during growth of nanocrystalline aggregates: Insights from TiO2, J. Phys. Chem. B. 104 (2000) 3481–3487. https://doi.org/10.1021/jp000499j.

[36] S. Ding, J.S. Chen, D. Luan, F.Y.C. Boey, S. Madhavi, X.W. Lou, Graphene-supported anatase TiO2 nanosheets for fast lithium storage, Chem. Commun. 47 (2011) 5780–5782. https://doi.org/10.1039/c1cc10687b.

[37] J.S. Chen, Z. Wang, X.C. Dong, P. Chen, X.W. Lou, Graphene-wrapped TiO2hollow structures with enhanced lithium storage capabilities, Nanoscale. 3 (2011) 2158–2161. https://doi.org/10.1039/c1nr10162e.

[38] H.C. Tao, L.Z. Fan, X. Yan, X. Qu, In situ synthesis of TiO 2-graphene nanosheets composites as anode materials for high-power lithium ion batteries, Electrochim. Acta. 69 (2012) 328–333. https://doi.org/10.1016/j.electacta.2012.03.022.

*This page intentionally left blank*

# 3 Supercapacitors

Supercapacitors are electrochemical energy storage devices (EESDs) which can store energy by electrostatic charge accumulation and through redox reactions. Compared to batteries, their specific energy is lower, with typical values of few Wh/kg, but they achieve far higher specific power, up to 10 kW/kg in short times of few seconds. In addition, they ensure a longer life-cycle than batteries, sustaining up to millions of cycles. They can replace or complement batteries in energy storage applications which requires high current density [1].

## 3.1 Basic concepts of supercapacitors

Supercapacitors, also called Electrochemical Double Layer Capacitors (EDLCs) or ultracapacitors, are promising devices for electrical energy storage. The charge storage mechanism is mainly based on (1) electrostatic charge accumulation, known as non-Faradaic electrical energy storage, and in certain kind of supercapacitors also on (2) Faradaic effects, including pseudocapacitive effects, arising from a charge-transfer process. A supercapacitor is composed of two porous carbon electrodes, which are in direct contact with the current collector and they are separated from each other by a thin porous film soaked in an electrolyte [1–3].

The charge separation mechanism was first described by the Helmholtz model (Figure 3.1a) [4]. When an electric potential is applied between the two electrodes, the charge carriers in each polarized electrode are electrically balanced by ions of opposite sign. The charge neutrality is ensured by anions and cations from the electrolyte which diffuse to the interface between the electrode and the electrolyte, forming the so-called Helmholtz layer, typically few nanometres thick. The Helmholtz layer at each interface recalls the structure of a conventional parallel-plate capacitor and the capacitance $C_H$ is thus defined by the:

$$C_H = \varepsilon_0 \varepsilon_r \frac{S}{d} \qquad (3.1)$$

where $\varepsilon_0$ is the vacuum permittivity ($\varepsilon_0$=8.85·10$^{-12}$ F/m), $\varepsilon_r$ the relative permittivity of the electrolyte, $S$ the surface area of the electrode and $d$ the thickness of the double-layer, consisting in the distance between the electrode charged surface and the counter-ion layer, approximated as the Debye length.

Given that porous carbon electrodes can provide specific surface area (SSA) up to 3000 m$^2$/g and the Debye length is in the atomic range dimension, the capacitance of a supercapacitor results much higher than that of a conventional capacitor.

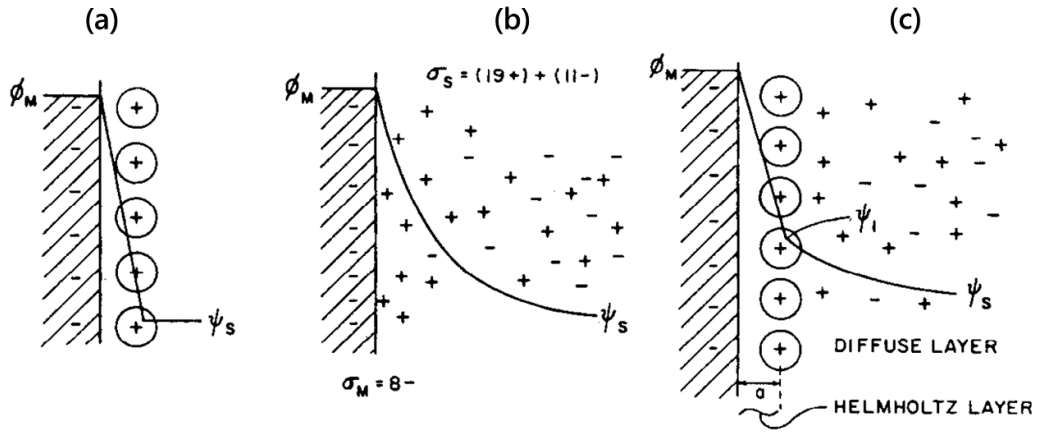


*Figure 3.1 Models of the double layer: (a) Helmholtz model; (b) Gouy-Chapman model; (c) Stern model. Specific charge per unit area (σ) are indicated for anions and cations, as an example* [3].

In the Helmholtz model, the charges on the electrodes are fully screened by the opposite sign ions in the Helmholtz layer. However, diffusion of the ions in the electrolyte solution is not considered. A *diffuse* double layer model was proposed by Gouy and Chapman [5,6], introducing a thermal fluctuation factor for ions in the solution, whose distribution follows the Boltzmann distribution (Figure 3.1b). The electric potential decreases exponentially from the electrode to the bulk layer.

Up to now, the models assume that the ions are point charges. The overestimated double-layer capacitance from the Gouy-Chapman model was corrected by the Stern theory [7], which combines the previous models, considering both the Helmholtz layer and the diffuse region, and accounts the finite size of the ions, including the solvation shell (Figure 3.1c).

Consequently, the two regions can be considered as two capacitors in series, described by an equivalent circuit

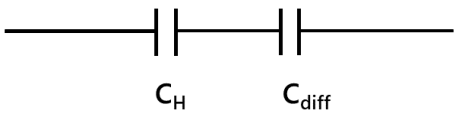


The resulting capacitance $C_{DL}$ of the electrode is given by the:

$$\frac{1}{C_{DL}} = \frac{1}{C_H} + \frac{1}{C_{diff}} \qquad (3.2)$$

where the capacitance $C_H$ is referred to the Helmholtz layer and the $C_{diff}$ to the diffuse region.

Considering the double-layer structure of the supercapacitor (Figure 3.2), the system is equivalent to two capacitors in series, one in each electrode. The capacitance $C$ (F/g) of an EDLC is given by the:

$$\frac{1}{C} = \frac{1}{C_+} + \frac{1}{C_-} \qquad (3.3)$$

where $C_+$ and $C_-$ are the capacitance of the positive and negative electrode, respectively.

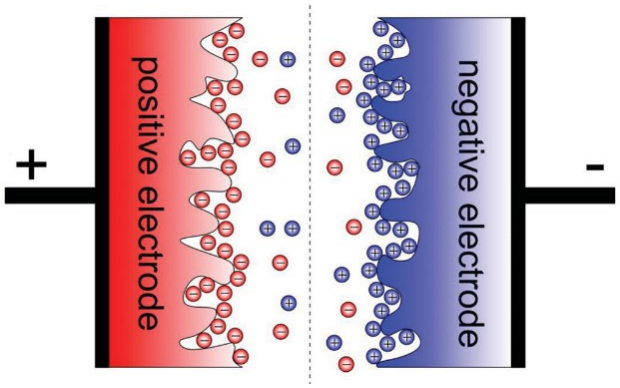


*Figure 3.2 Representation of the charged state of a symmetrical supercapacitor with porous electrodes* [2].

## 3.2 Types of supercapacitors

Three categories of supercapacitors can be identified, depending on the charge storage mechanism and on the material of the electrodes,: (1) electrochemical double-layer capacitors (EDLCs), (2) pseudocapacitors and (3) hybrid electrochemical capacitors (HECs) [8].

To obtain a high-power supercapacitor, ideal features of the electrode materials are: high specific surface area (SSA), to give high specific capacitance, according to the equation 3.1; appropriate pore structure in order to ensure both the access of the electrolyte ions and their transport in the bulk electrode; high electrical conductivity; electroactive sites to favour the pseudocapacitive effects; high corrosion resistance; long-term chemical stability; high-temperature stability; environmental compatibility; low cost materials.

### 3.2.1 Electrochemical Double-Layer Capacitors

Electrochemical Double-Layer Capacitors (EDLCs) are based on two symmetric electrodes impregnated by the electrolyte solution, usually made of salts in organic or aqueous solvents. As described in section 3.1, EDLCs store energy accumulating charges on the double-layer at each electrode/electrolyte interface.

A promising candidate material for the electrodes, having the listed above characteristics, is porous carbon, for its inexpensiveness and good resistance during charge/discharge processes. Providing SSA values up to 2000-3000 $m^2/g$, activated porous carbon are widely constituting the main part of the electrodes [9–11]. Other materials being used are carbon nanotubes [12,13]. Graphene-based materials are as well good structure to increase specific capacitance, thanks to its theoretical SSA value of 2630 $m^2/g$ [14–16].

In addition to a high SSA, mainly originated by the porosity of the carbon structure, a high specific capacitance can be further promoted by a regularly interconnected porosity in the electrode material. According to the IUPAC definition [17], three groups of pores are identified: micropores with diameters smaller than 2 nm, mesopores between 2 and 50 nm, macropores bigger than 50 nm (Figure 3.3). To optimize the charge storage, the ideal structure of pores should be adapted to the size of the solvated ions of the electrolyte. A mesoporosity is thus encouraged with pore size about twice the size of the solvated ions (i.e., in the 3-5 nm range, being 1-2 nm the average size of the solvated ions in organic electrolytes), to guarantee ion adsorption on both pore walls. However, a large increase in

specific capacitance has been observed for pore size less than 1 nm, caused by the distortion of the solvation shell and partial de-solvation of the ions, which favours the access of the ions into pores of similar sizes to those of the bare ions [18]. Hence, an interconnected pore network can guarantee both the electrolyte wetting and a rapid ion motion inside the electrode.

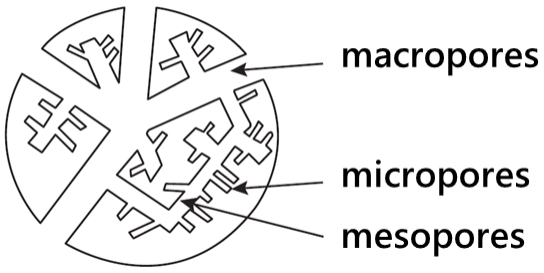


*Figure 3.3 Representation of pores created inside a carbon particle of about 10 µm in diameter* [19].

The use of porous carbon materials with an optimized pore structure makes the EDLCs a promising high-power energy source.

### 3.2.2 Pseudocapacitors

Pseudocapacitors are another category of supercapacitors, being between a secondary battery and an EDLC. They also consist of two electrodes impregnated by the electrolyte solution. The charge storage mechanism is given by reduction-oxidation (redox) reactions, which occur at the electrodes with electron charge-transfer between electrolyte and electrode. The chemical affinity between the adsorbed ions and the electrode materials is fundamental to produce pseudocapacitive effects. The most adequate materials for pseudocapacitors are transition metal oxides ($RuO_2$, $MnO_2$, $V_2O_5$, $TiO_2$), which can give high specific capacitance, thanks to multiple oxidation states that they can vary in the redox processes [20–24]. In addition, good pseudocapacitive materials are also conducting polymers (polyaniline, polypyrrole, polyacetylene), with high conductivity that can assure high capacitance [25]. Materials such as carbon enriched in heteroatoms [26–28] and microporous carbons with electrosorbed hydrogen also give rise to pseudocapacitance [29].

The pseudocapacitive behaviour can result from three types of mechanism: (1) underpotential deposition, (2) redox reactions and (3) intercalation processes. Underpotential deposition occurs when a monolayer of metal ions is deposited onto a different metal electrode surface at a higher reduction potential than that when it is deposited onto itself. A typical example is represented by the deposition of lead onto a gold electrode (Figure 3.4a). Redox pseudocapacitance arises from redox reactions between electrolyte and electrode with a Faradaic charge-transfer. The first discovered material exhibiting pseudocapacitance was ruthenium oxide (hydrated), which accepts protons from the electrolyte and changes its oxidation state from +4 to +3 (Figure 3.4b). Intercalation pseudocapacitance results from the insertion of ions into the bulk layers of the electrode. The reaction involves Faradaic charge-transfer without changes in the crystallographic phase. The most investigated materials in intercalation pseudocapacitive processes is $Nb_2O_5$ (Figure 3.4c) [3,8,24].

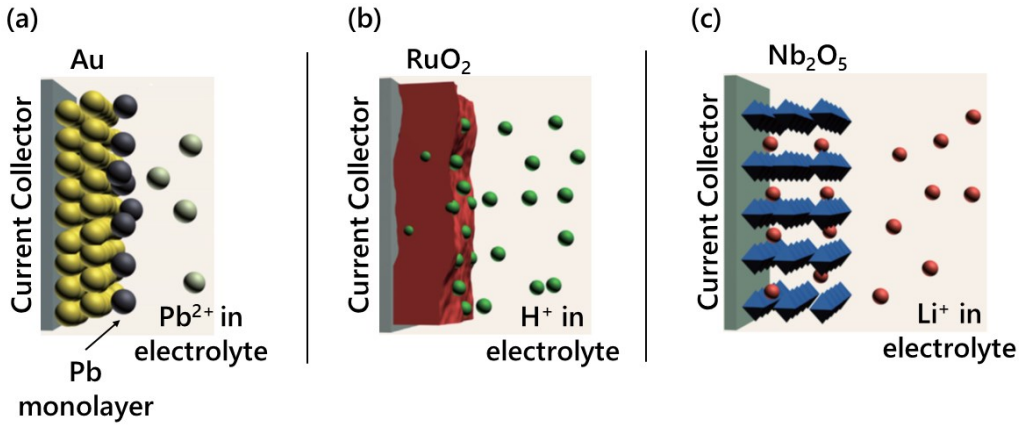


*Figure 3.4 Different mechanisms that give rise to pseudocapacitance: (a) underpotential deposition, (b) redox pseudocapacitance and (c) intercalation pseudocapacitance* [24].

### 3.2.3 Hybrid Electrochemical Capacitors

Hybrid Electrochemical Capacitors (HECs) combine the other two types of supercapacitors with the attempt to improve the performance compared to the pristine EDLCs and pseudocapacitors. HECs storage charge mechanism involve both Faradaic and non-Faradaic processes. Three groups can be identified based on the electrode materials: (1) asymmetric hybrids, (2) battery type hybrids and (3) composite hybrids. Asymmetric systems consist of two different electrodes which are made of different materials. They combine an EDLC electrode, usually made of carbon-based materials, with a pseudocapacitive

electrode, being transition metal oxides or conducting polymers. The charge storage involves both electrostatic adsorption-desorption at the carbon electrode (non-Faradaic process) and fast pseudocapacitive reactions at the surface of the other electrode (Faradaic process). Since the specific capacitance of the Faradaic electrode (*C(+)*) is usually higher than that of the carbon electrode (*C(-)*), the total specific capacitance in asymmetric devices is mostly influenced by the *C(-)*, giving $C \approx C(-)$. Hence, the value results almost doubled compared to a symmetric EDLC, whose capacitance is given by the equivalent capacitance of two capacitors. In symmetrical EDLCs, with both the electrodes being formed by carbon-based material, the equivalent capacitance results $C = C(-)/2$. Thanks to this coupling, better cycling stability, higher specific energy and specific power are achieved [30]. In battery type hybrid capacitors, the strategy to utilize both the high power of supercapacitors and the high energy of batteries consists of the combination of one ECDL-like electrode with a battery electrode. As lithium-ion batteries (LIBs) are the state-of-art in batteries, the lithium-ion capacitors (LICs) represent the most investigated hybrid capacitors in the category. Typically, a porous activated carbon (AC) is used as the positive electrode and a lithium-ion intercalating carbon material as the negative electrode. Since graphite is the most common anode material in LIBs, it is usually used also in LICs, while some carbon blacks and graphene have been recently proposed for the positive electrode to replace AC and increase the specific capacitance [31,32]. During the charge/discharge processes, lithium ion intercalation/extraction occurs at the negative electrode whereas anion adsorption/desorption forms the electrical double-layer structure on the surface of the positive electrode. The advantages of a battery in terms of specific energy are coupled with the high-power, longer life-cycle and fast recharging times of a supercapacitor. Finally, in composite hybrid supercapacitors two materials are incorporated into each other within a single electrode, being usually carbon-based materials on one hand and conducting polymers or transition metal oxides on the other hand. Physical and chemical charge storage mechanisms are both involved in the same electrode [33]. A representation of the combination of hybrid supercapacitors is shown in Figure 3.5.

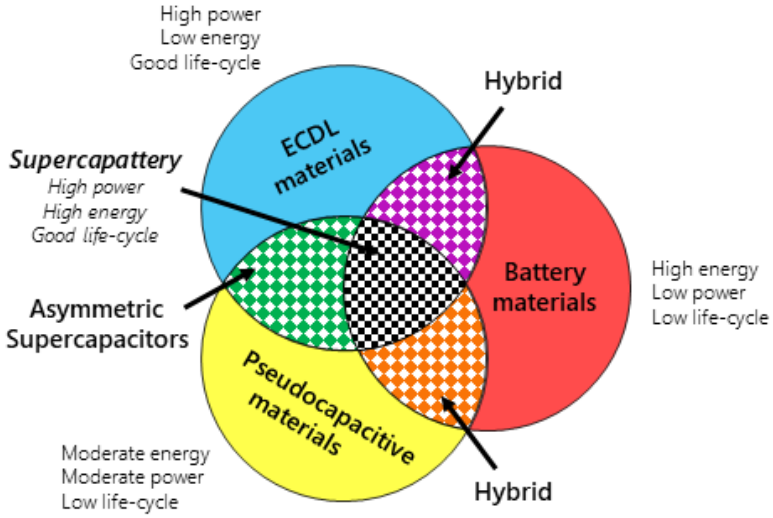


*Figure 3.5 Representation of the characteristics of hybrid supercapacitors* [8]

## 3.3 Electrolytes

Electrolytes, which are composed of a salt dissolved in a solvent, play an important role in the performance of supercapacitors. Two main key features are recommended: a large electrochemical stability window and a high ionic conductivity [2,34]. The electrochemical stability window of the electrolyte is one of the most influencing parameters for the working voltage window, in addition to the degradation of the electrode. The choice of this voltage is then reflected both on the energy stored in the supercapacitors, since it is proportional to the square of the maximum applied voltage, and on power density, depending on energy density. Regarding the ionic conductivity, this parameter plays a fundamental role in the equivalent series resistance (ESR) of the supercapacitor, which is determined also by the ionic resistance of the electrolyte. The ionic conductivity is dependent on the salt concentration up to a maximum value, above which additional salt ions do not increase the conductivity of the electrolyte [25]. In addition to these crucial characteristics, other aspects are important in the choice of the electrolytes. Pure electrolytes are advised, since residual impurities can lower the electrochemical stability of the potential window and introduce a self-discharge. The matching between the electrolyte and the electrode should be optimized, as described in section 3.2.1, to obtain a hierarchical porous structure in the electrode, which favours the accessibility of electrolyte ions and their diffusion in the electrode material. Extending the operating temperature range is required for several

electrochemical supercapacitors applications, e.g. the high working temperature in fuel cell vehicles or the low temperature related to space avionics applications.

Electrolytes are classified into aqueous, organic, ionic liquids, solid-state and redox-active electrolytes [34].

### 3.3.1 Aqueous electrolytes

Aqueous electrolytes are widely used thanks to their low cost and low toxicity. Typically, aqueous electrolytes have a good ionic conductivity (up to ~1 S/cm), even higher than that of organic and ionic liquid electrolytes. Though, the electrochemical stability window is narrow due to the water decomposition potential of 1.23 V at room temperature. To avoid that the gas evolution causes the break of the cell, the operating potential is usually up to 1 V and the stored energy is thus limited. Among aqueous electrolytes, acid, alkaline and neutral solutions can be identified and $H_2SO_4$, KOH and $Na_2SO_4$ based electrolytes are the most extensively used, respectively [36–38]. Acidic electrolytes usually give rise to higher specific capacitance, thanks to their higher ionic conductivity and consequently lower ESR [36]. Typically, $H_2SO_4$ gives a conductivity of 0.7-0.8 S/cm [39]. However, the interaction between the electrode and the electrolyte is crucial in the choice of the electrolyte. For example, pseudocapacitive effects can be enhanced by the nature of the electrolyte because of different behaviour of surface functionalities with different electrolytes [40]. Typically, aqueous acidic and alkaline electrolytes determine a faster degradation of the electrodes than organic ones, leading to a shorter life-cycle of supercapacitors. On the other hand, neutral electrolytes give rise to less corrosive effects. In addition, they can admit a larger potential stability window because the equilibrium $H^+|OH^-$ is not shifted in one direction and these ions are not favoured to react with the appropriate electrodes. The larger electrochemical stability makes neutral electrolytes promising candidates in enhanced energy density [41].

### 3.3.2 Organic electrolytes

Organic electrolytes are dominating the market, thanks to their high potential stability window, typically in the range of 2.5-2.8 V [34]. However, they have higher cost, smaller specific capacitance, lower conductivity and safety concerns about flammability, volatility and toxicity. They are composed of conductive salts dissolved in a solvent, usually

acetonitrile (ACN) or propylene carbonate (PC). Among the conductive salts, tetraethylammonium tetrafluoroborate ($TEABF_4$), $LiPF_6$, $NaPF_6$ , $LiClO_4$ are typically used. Since different salts usually contain ions with different bare and solvated ion sizes, the matching between the pores size of the electrode material and the electrolyte ions should be optimized. The usually larger size of the solvated ions compared to ions in aqueous electrolytes gives rise to lower specific capacitance. Working with large potential windows can lead to the degradation of electrodes, e.g. with the formation of cracks, exfoliation of the electrode material or film deposit onto the electrode surface. Degradation sources are unremoved or residual water from the electrode, which is released into the electrolyte; electrochemical oxidation and reduction of the surface electrode functional groups which are released as gaseous products (CO and $CO_2$); electrochemical oxidation and reduction of the electrolyte solvent [42]. About the ionic conductivity, organic electrolytes show lower values compared to those for aqueous electrolytes. For the commonly used $TEABF4_4$/ACN, it is 0.06 S/cm [39]. The lower ionic conductivity has an impact on ESR and, consequently, on power density.

### 3.3.3 Ionic liquid-based electrolytes

Ionic liquid-based electrolytes are salts with melting points below 100°C and in some cases even below room temperature. They are composed of a large organic cation combined with an organic or inorganic anion. They are grouped in aprotic, protic and zwitterionic types. They usually have low ionic conductivity ($10^{-4}$-$10^{-2}$ S/cm at room temperature) and high viscosity, which both influence the internal electrical resistance. Other drawbacks are related to their high hygroscopicity and expensive cost. However, they have the greatest advantage of being solvent-free, solving safety concerns related to organic solvents [34,43,44].

### 3.3.4 Solid-state electrolytes

Solid-state electrolytes have recently attracted great attention with the increasing interest in portable, flexible, wearable electronics and micro-electronics. The solid-state electrolytes serve both as ionic conducting electrolytes and as electrode separators. Most of them are based on polymer electrolytes, which can be in the dry (solid polymer electrolytes, known as *SPE*) [45] or gel (gel polymer electrolytes, known as *GPE* as well as ionogel) state [46] (Figure 3.6). Thanks to the presence of a liquid phase, GPEs have usually higher ionic

conductivity. On the other hand, the mechanical strength is relatively poor and the operative temperature range is limited due to the use of water as solvent. Dominating the solid-state products, GPEs are composed of a polymer matrix and a liquid electrolyte, whose presence makes them called as quasi-solid-state electrolytes in some studies [47]. The most used materials for polymer matrix are poly(vinyl alcohol) (PVA), poly(ethyl oxide) (PEO), poly(acrylic acid) (PAA), poly(methylmethacrylate) (PMMA), poly(ether ether ketone) (PEEK). Water is typically used as solvent, as well as organic solvents such as PC, ethylene carbonate (EC), dimethylformamide (DMF) and their mixtures. In the case of PVA, it is generally combined with electrically conductive acidic (e.g. $H_2SO_4$ or $H_3PO_4$), alkaline (e.g. KOH) or neutral (e.g. LiCl) aqueous solutions [48]. Organic gel electrolytes have been studied to increase the working cell voltage [46,49].

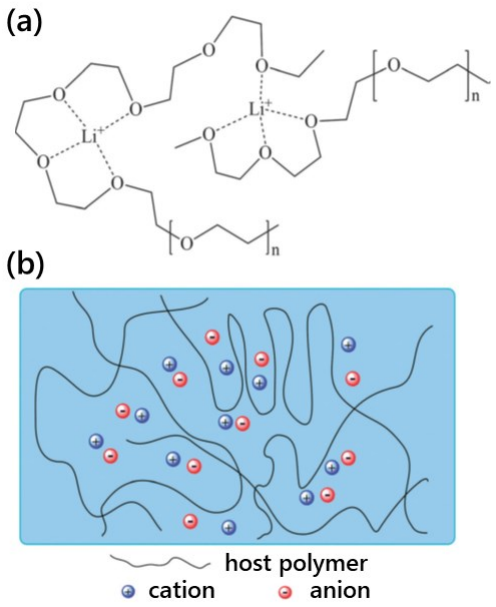


*Figure 3.6 Representation of (a) dry solid-state electrolyte (e.g. PEO/$Li^+$) and (b) gel polymer electrolyte* [34].

### 3.3.5 Redox-active electrolytes

Redox-active electrolytes have been recently investigated to increase supercapacitors performance by adding an extra pseudocapacitance from Faradaic reactions occurring in the electrolyte. As an example, electrolytes based on iodide aqueous solution (e.g. KI, NaI, RbI, LiI) induce redox reactions at the electrode/iodide interface due to the various oxidation

states of the iodine from -1 to +5. Thus, the iodide ions work both as good ionic conductor and as a source of pseudocapacitive effects. Then, good cycling is preserved by the reversibility of different iodine redox couples [50]. Pseudocapacitive sources have been found also in redox mediators, such as heteropoly acids or organic compounds as hydroquinone and various dyes (e.g. methylene blue, indigo), which have a high proton conductivity. To reduce the self-discharge observed in the presence of redox-active electrolytes, an ion exchange membrane (e.g. Nafion) can be introduced as a separator, preventing the migration of redox-active electrolytes between the electrodes. To minimize the self-discharge, the choice of the electrolyte itself should be addressed to species which could be converted into insoluble species during the charge-discharge process [51].

## 3.4 Towards micro-supercapacitors

Recent advances in supercapacitors have been focused on miniaturization, due to the increasing demand of micropower sources and small-scale energy storage devices [52]. Micropower modules are required in devices such as sensors, portable and wearable electronics, as well as radio frequency identification (RFID), global positioning systems (GPS) or biomedical implants. These systems need self-powdered devices, which can work wirelessly and independently of an external source of power. As a new sustainable technology, they can harvest energy from the environment (known as *random energy*), coming from irregular vibrations, light airflow, noise and human activity [53]. Wireless network sensors find widespread applications in environmental, health and military fields as well as agriculture and industrial monitoring up to home automation [54]. As of today, self-powdered devices widely consist of small-scale batteries. Though, they show some disadvantages related to the need of changing batteries at the end of their life or resulting from the request of high spike of current in the application. Supercapacitors may represent a promising option to replace or complement batteries, as they can provide the stored energy in a very short time, due to their high power density and they can operate for millions of cycles. In addition, supercapacitors are well suitable to being miniaturized, since conventional supercapacitors are too large for the microelectronics devices. The main miniaturization requirements are the integration of small-scale devices and the direct positioning on a chip [52].

To this extent, miniaturized supercapacitors, also called micro-supercapacitors or electrochemical micro-capacitor, have been recently explored. A micro-supercapacitor (MSC) is a miniaturized supercapacitor that is employed as a power source or an energy storage unit in microelectronic devices. Its total footprint area is in the range of square

millimetre or, at maximum, square centimetre scale and the power in the scale of microwatts. The required energy density depends on the application, relying on the period of time the micro-supercapacitors can deliver the power [52]. The design of a micro-supercapacitor is fundamental for obtaining a good combination among the components and for satisfying the appropriate energy and power densities. As in conventional supercapacitors, crucial parameters are a high surface area with a hierarchical pore network structure and a good conductivity of the electrodes [2]. The first "architecture" of micro-supercapacitors resembles the planar 2D configuration of thin film micro-batteries, where the electrodes are made of thin films (less than 10 μm) facing each other and the solid electrolyte is placed between them, making a *sandwich* structure, as depicted in Figure 3.7a.

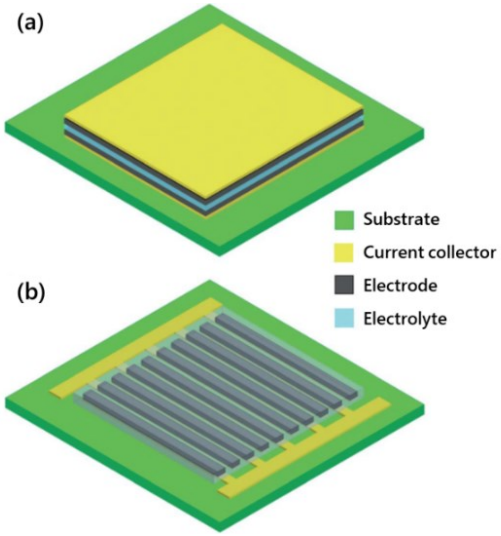


*Figure 3.7 Scheme of micro-supercapacitors with (a) conventional 2D architecture and (b) in-plane interdigital electrode architecture* [52].

To optimize energy and power densities, a different architecture has been tested, consisting of various microelectrodes built on a substrate in an interdigitated arrangement. The two electrodes result in an in-plane configuration, instead of a vertical stack (Figure 3.7b). Several advantages result from this architecture: since the distance between the electrodes can be controlled, small ion diffusion path can be reached, promoting an easier ion transport from the electrolyte to the electrode; in addition, the access of electrolyte ions is favoured by the increased accessibility of the electrode sides which promote the complete use of the electrode surface (Figure 3.8a), whereas in the stacked configuration some

regions are inaccessible (Figure 3.8b); higher specific capacitance can be achieved reducing the spacing between the electrode fingers and increasing their number [52].

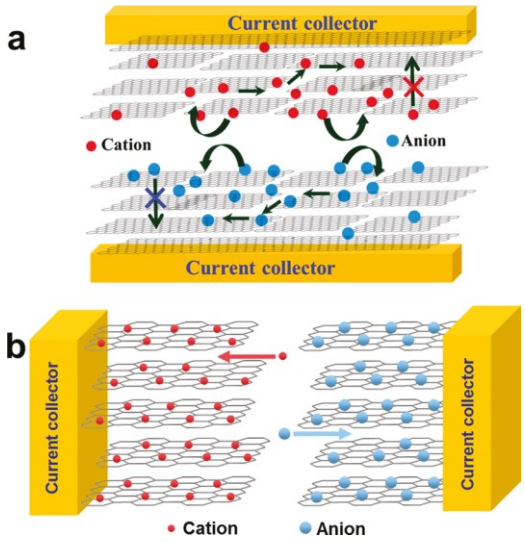


*Figure 3.8 Schematic representation of (a) stacked architecture and (b) in-plane architecture of micro-supercapacitors* [55].

## 3.5 Micro-supercapacitors: highlights

Besides the architecture, other factors can be handled in the production of the electrodes in a micro-supercapacitor, in order to optimize the electrochemical performance: high SSA electrodes with highly accessible surfaces; low contact resistance between the electrode and the current collector; binder-free electrodes.

A reduced resistance between the electrode and the current collector can be obtained bridging them with graphene layers, which can be placed perpendicular to the current collector surface, since the in-plane conductivity of graphene is higher than that out-of-plane [56]. Making the electrodes of graphene itself is also a promising strategy to increase the energy density, due to its high SSA and its open planar structure, which facilitates the electrolyte ion diffusion. Though, a restack of the graphene sheets can occur during the electrode production, preventing the complete accessibility of the electrode surface to the electrolyte ions. The introduction of spacers between graphene layers (e.g. carbon nanotubes) can minimize their restacking [57,58]. The creation of binder-free electrodes

should improve the energy performance, due to the lack of an organic binder, which can introduce a resistance in the access of electrolyte ions in the active material [59,60].

Other than electrodes configuration, the choice of the electrolyte is important for the electrochemical performance, as for traditional supercapacitors. Ionic conductivity, electronic insulation and electrochemical potential stability are still required in micro-supercapacitors [52]. Among them, gel polymer electrolytes have been attracted a great interest, thanks to the increasing trend in producing portable and flexible devices, which can achieve better packaging and reduce the electrolyte leakage [60–62].

## 3.6 Micro-supercapacitors: methods of production

Micro-supercapacitors are usually produced in thin film electrodes, made of high surface area carbon-based materials as well as pseudocapacitive materials or composites. Several traditional methods are employed to produce them: lithography, sputtering, chemical vapour deposition, layer-by-layer deposition, ink-jet printing, electrochemical and electrophoretic deposition, spray deposition [52,58,59,63]. Beside them, innovative unconventional methods have been recently tested to take advantages of the in-plane configuration. The peculiarity is based on a patterning process through which the active material composes the interdigitated electrodes, without requiring a multi-step process. These innovative methods use the laser light to convert precursor materials into the electrode active materials by means of the creation of micro-electrodes patterning. The interdigitated patterned parts compose the electrodes, whereas the spaces between them serve as separator. Different laser sources have been examined, such as a $CO_2$ laser in the infrared range (9.3-10.6 μm) [64], a femtosecond laser [65], or an infrared DVD burner laser (780 nm) [60,66,67].

One of the most outstanding advantage of the direct laser writing is the *one-step* process which promotes the creation of up to 100 micro-supercapacitors in a short period of time in the range of few tens of minutes. This peculiarity makes the laser writing methods as an extremely promising low-cost and scalable technique in micro-supercapacitors production.

### 3.6.1 LightScribe® technology

The growing trend of miniaturized electronics has recently led to the development of innovative techniques to build micro-supercapacitors. The use of direct laser writing is a challenging approach, thanks to its several advantages compared to the mentioned methods in section 3.6. Flexibility, lightness and portability of energy storage devices are in great demand properties to produce micro-electronics products. Several laser sources have been investigated, both in continuous and pulsed mode, varying in the excitation wavelength from the infrared to the ultraviolet range. One of the most promising methods is the LightScribe® technique, which uses the infrared laser light of a DVD burner to induce the conversion of precursor reagents into active materials constituting the micro-electrodes.

LightScribe® technology, introduced by Hewlett-Packard in 2004, was created to produce labels onto the upward surface of a disc by means of the DVD burner laser. Compared to the burning direction, the LightScribe disc is put upside down into the DVD burner. The LightScribe discs surface is coated with a dye-based coating, which changes its colour when absorbs the infrared light of the DVD burner laser. During the process, the disc is rotating in the DVD drive while the laser acts on the surface in concentric circles, starting from the centre of the disc and moving outward. The technology promoted the creation of labels or shapes onto LightScribe disc surfaces. As of today, LightScribe technology is not developed by HP, yet it is still applicable with a LightScribe drive and LightScribe DVDs.

By exploiting this technique, El Kady and Kaner have recently employed a LightScribe DVD drive to build micro-electrodes. The reactive material coating the disc consists of graphite oxide, which is deposited in aqueous solution onto a flexible plastic substrate, glued onto the surface of a LightScribe DVD [60]. The excitation source is the infrared laser of a DVD burner, which works with the same mechanism used for the creation of LightScribe labels on DVD. A LightScribe DVD drive, combined with a LightScribe labeling software, supports LightScribe discs on which labels can be written as well as micro-electrodes. By the burning process, the same surface of a DVD disc can be decorated with interdigitated planar patterns converted in micro-electrodes. Thus, the LightScribe technology proves to be effective in scalability of the products, thanks to the high number of micro-supercapacitors, which can be obtained after each burning round. It is worth recalling that the typical area of micro-supercapacitors is in the range of square millimetres. In a few tens of minutes, up to a hundred interdigitated electrodes can be created on a single DVD disc [60]. The main advantage of this technique is shown in the *one-pot* burning process, which does not require any additional action afterwards for the creation of the micro-electrodes. To this

extent, the LightScribe method results inexpensive and competitive compared to conventional methods, which usually require additional processes or sophisticated steps.

In addition, the LightScribe process also meets the high demand of portable and flexible devices. Micro-supercapacitors with bending and twisting properties can be obtained, without affecting the structural integrity of the device.

The production process of *laser-scribed* micro-supercapacitors is reported in figure 3.9.

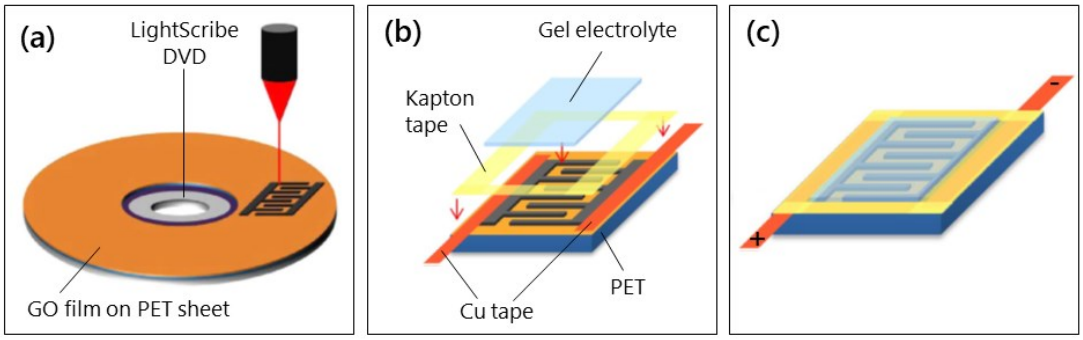


*Figure 3.9 Schematic representation of the production process of a laser-scribed micro-supercapacitor* [60].

A graphite oxide (GO) film is deposited onto PET sheet, glued on the LightScribe DVD. The LightScribe mask is created by the DVD burner laser, according to the drawing in the LightScribe software. Interdigitated patterns are produced in correspondence of the drawn patterns, where GO is converted into black laser-scribed graphene (Figure 3.9a). The micro-supercapacitor is assembled by using the interdigitated patterns both as electrodes and current collectors, whereas the unchanged spaces between them serve as separator. The device is contacted with copper tape along the edges of the patterns and the Kapton tape defines its interdigitated area. Above it, a gel electrolyte is added (Figure 3.9b). Gel electrolytes are recommended to ensure the device flexibility. Finally, in figure 3.9c the planar micro-supercapacitor is shown. The electrochemical performance of laser-scribed MSCs results in a specific capacitance of 2.23 mF $cm^{-2}$ at a current density of 16.8 A $cm^{-3}$, with a 60% capacity retention at ultrahigh current density (18.4 A $cm^{-3}$). An excellent power density of ~200 W $cm^{-3}$ is achieved, making laser-scribed MSCs a promising candidate in enhancing supercapacitors properties [60].

## 3.7 Laser Induced Graphene

Laser-scribing techniques usually convert carbonaceous materials into graphene derivative products, which are typically known as laser-induced graphene (*LIG*) [66,68] or laser-scribed graphene (*LSG*) [60] or laser-derived graphene (*LDG*) [69], even if they are not strictly composed of single monolayer of $sp^2$-carbon atoms.

During the laser treatment, a carbonaceous material, typically with $sp^3$-carbons, undergoes a photothermal reaction and converts into a $sp^2$-carbon lattice, creating a 3D porous graphene-based material. Since the first production of LIG starting from polyimide (Kapton, PI) by Tour and his group in 2014 [66], several carbonaceous sources have been investigated, such as graphite oxide and graphene oxide [60,64,67,70], poly(ether ether ketone) (SPEEK) [71], lignin-containing woods [72] or even natural materials and foods (e.g. coconuts, bread, potatoes skin) [73].

Despite the electronic properties of LIGs are lower than graphenes obtained by chemical methods, the laser-scribed materials are found to be particularly suitable for applications requiring 3D graphene patterns, in several fields such as energy storage, sensoristics, electrocatalysis and biomedical electronics [69]. LIGs are characterized by a defective structure, deriving from the thermal expansion of the material caused by laser irradiation, which results in the formation of wrinkly ripples due to the folding of graphene layers. Laser-scribed materials can have heptagons and pentagons in the lattice, locally replacing the hexagonal honeycomb carbon network, determining a curvature in the material and a resulting porous structure. The presence of these defects can be regarded as a strength in the material functionalization for energy storage applications. Since the growth of nanoparticles (NPs) can be promoted onto a defective structure [74,75], composite materials based on graphene derivatives combined with NPs are highly recommended for the enhancement of the electrochemical performance of micro-supercapacitors. In addition, defects can result theirselves responsible for the increase of electrochemical properties [66].

## 3.8 From research to a successful application

The recent trend toward miniaturization of electronics devices has attracted great attention in developing promising configurations for the build of flexible, portable and small-scale devices. Micro-supercapacitors have been recently investigated, as they can be easily miniaturized and integrated in electronics equipment. Thanks to their longer life-cycle

compared to batteries and their high-power density, which is crucial in applications requiring high spike of current, micro-supercapacitors represent interesting candidates to replace or complement batteries in energy storage applications.

Facing the multi-step processes of expensive procedures to synthesize graphene, innovative technologies are focusing on producing cost-effective graphene-based materials, combining large-scale synthesis and patterning to make electronic devices with a straightforward process. Through laser-scribing techniques, a successful combination of material synthesis and device production is achieved. Among several laser sources, LightScribe® technology is one of the most promising methods, since it can produce patterned graphene-based materials in interdigitated electrodes in a *one-step* process with a scalable approach. Graphene-based materials can be created starting from carbonaceous sources, by using the DVD burner laser. Graphite oxide, being widely used as precursor, is particularly suitable for the process, especially in the preparation of the reagents. In particular, graphite oxide obtained by the Hummers' method is recommended for its hydrophilicity, which ensures a homogeneous aqueous dispersion in the preparation of disc coating. Graphene derivatives, as obtained by the laser treatment, can promote the growth of nanoparticles on their defective structure. Combined materials, made of nanoparticles decorating graphene-based materials, are expected to enhance the electrochemical performance of micro-supercapacitors. To this extent, $TiO_2$ is found to be a competitive candidate, thanks to its chemical stability, low toxicity, abundancy and low cost. Obtaining nanostructured materials, consisting of $TiO_2$ nanoparticles on graphene-based products is found to increase the electrochemical performance of micro-supercapacitors.

The research presented here has been focused on the production of micro-supercapacitors by using the LightScribe technology and on the evaluation of their electrochemical properties. The goal of simultaneously producing both graphene derivatives and $TiO_2$ nanoparticles by using the LightScribe technique has proven to be a successful strategy.

## References


[1] P. Simon, Y. Gogotsi, Materials for electrochemical capacitors, Nat. Mater. 7 (2008) 845–854. https://doi.org/10.1038/nmat2297.

[2] F. Béguin, V. Presser, A. Balducci, E. Frackowiak, Carbons and electrolytes for advanced supercapacitors, Adv. Mater. 26 (2014) 2219–2251. https://doi.org/10.1002/adma.201304137.

[3] B.E. Conway, Electrochemical supercapacitors: scientific fundamentals and technological applications, Plenum Publishers: Kluwer New York, 1999.

[4] H. Helmholtz, Ueber einige Gesetze dcr Vertheilung elektrischer Striime in kiirperlichen Leitern, mit Anwendung au f die thierisch -elektrischen Versuche, Ann. Der Phys. Und Chemie. 165 (1853) 353–377. https://doi.org/10.1002/andp.18531650702.

[5] M. Gouy, Sur la constitution de la charge électrique à la surface d'un électrolyte, J. Phys. Théorique Appliquée. 9 (1910) 457–468. https://doi.org/10.1051/jphystap:019100090045700.

[6] D.L. Chapman, LI. A contribution to the theory of electrocapillarity, London, Edinburgh, Dublin Philos. Mag. J. Sci. 25 (1913) 475–481. https://doi.org/10.1080/14786440408634187.

[7] O. Stern, ZUR THEORIE DER ELEKTROLYTISCHEN DOPPELSCHICHT, Zeitschrift Für Elektrochemie Und Angew. Phys. Chemie. 30 (1924) 508–516. https://doi.org/10.1002/bbpc.192400182.

[8] A. Afif, S.M. Rahman, A. Tasfiah Azad, J. Zaini, M.A. Islan, A.K. Azad, Advanced materials and technologies for hybrid supercapacitors for energy storage – A review, J. Energy Storage. 25 (2019) 100852. https://doi.org/10.1016/j.est.2019.100852.

[9] D. Pontiroli, S. Scaravonati, G. Magnani, L. Fornasini, D. Bersani, G. Bertoni, C. Milanese, A. Girella, F. Ridi, R. Verucchi, L. Mantovani, A. Malcevschi, M. Riccò, Super-activated biochar from poultry litter for high-performance supercapacitors, Microporous Mesoporous Mater. 285 (2019) 161–169. https://doi.org/10.1016/j.micromeso.2019.05.002.

[10] T.E. Rufford, D. Hulicova-Jurcakova, Z. Zhu, G.Q. Lu, Nanoporous carbon electrode from waste coffee beans for high performance supercapacitors, Electrochem. Commun. 10 (2008) 1594–1597. https://doi.org/10.1016/j.elecom.2008.08.022.

[11] J. Gamby, P.L. Taberna, P. Simon, J.F. Fauvarque, M. Chesneau, Studies and characterisations of various activated carbons used for carbon/carbon supercapacitors, J. Power Sources. 101 (2001) 109–116. https://doi.org/10.1016/S0378-7753(01)00707-8.

[12] D.N. Futaba, K. Hata, T. Yamada, Y. Hayamizu, Shape-Engineerable and Highly Densely Packed Single-Walled Carbon Nanotubes and Their Application as Super-Capacitor Electrodes, Nat. Mater. 5 (2006) 987–994. https://doi.org/10.1038/nmat1782.

[13] C. Niu, E.K. Sichel, R. Hoch, D. Moy, H. Tennent, High power electrochemical capacitors based on carbon nanotube electrodes electrodes, Appl. Phys. Lett. 70 (1997) 1480–1482. https://doi.org/10.1063/1.118568.

[14] G. Moreno-Fernández, J.L. Gómez-Urbano, M. Enterría, T. Rojo, D. Carriazo, Flat-

shaped carbon-graphene microcomposites as electrodes for high energy supercapacitors, J. Mater. Chem. A. 7 (2019) 14646–14655. https://doi.org/10.1039/c9ta03295a.
[15] X. Du, P. Guo, H. Song, X. Chen, Graphene nanosheets as electrode material for electric double-layer capacitors, Electrochim. Acta. 55 (2010) 4812–4819. https://doi.org/10.1016/j.electacta.2010.03.047.
[16] L. Jiang, Z. Ren, S. Chen, Q. Zhang, X. Lu, H. Zhang, G. Wan, Bio-derived three-dimensional hierarchical carbon-graphene-TiO2 as electrode for supercapacitors, Sci. Rep. 8 (2018) 1–9. https://doi.org/10.1038/s41598-018-22742-7.
[17] T. Sing, K.S.W., Everet, D. H., Haul, R.A.W., Moscou, L, Pierotti, R.A., Rouquérol, J., Siemieniewska, Reporting physisorption data for gas/solid systems with special reference to the determination of surface area and porosity, Pure Appl. Chem. 57 (1985) 603–619. https://doi.org/10.1351/pac198557040603.
[18] J. Chmiola, Y. Chmiola, Y. Gogotsi, C. Portet, P. Simon, P.-L. Taberna, Anomalous Increase in Carbon Capacitance at Pore Sizes Less than 1 Nanometer, Sci. Mag. 313 (2006) 1760–1763. https://doi.org/10.1126/science.1132195.
[19] P. Simon, Y. Gogotsi, Charge storage mechanism in nanoporous carbons and its consequence for electrical double layer capacitors, Philos. Trans. R. Soc. A Math. Phys. Eng. Sci. 368 (2010) 3457–3467. https://doi.org/10.1098/rsta.2010.0109.
[20] V. Augustyn, P. Simon, B. Dunn, Pseudocapacitive oxide materials for high-rate electrochemical energy storage, Energy Environ. Sci. 7 (2014) 1597–1614. https://doi.org/10.1039/c3ee44164d.
[21] M. Toupin, T. Brousse, D. Bélanger, Charge storage mechanism of MnO2 electrode used in aqueous electrochemical capacitor, Chem. Mater. 16 (2004) 3184–3190. https://doi.org/10.1021/cm049649j.
[22] J. Kim, W.H. Khoh, B.H. Wee, J.D. Hong, Fabrication of flexible reduced graphene oxide-TiO2 freestanding films for supercapacitor application, RSC Adv. 5 (2015) 9904–9911. https://doi.org/10.1039/c4ra12980f.
[23] J.P. Zheng, T.R. Jow, A New Charge Storage Mechanism for Electrochemical Capacitors, J. Electrochem. Soc. 142 (1995) 60–62. https://doi.org/10.1149/1.2043984.
[24] J. Wang, S. Dong, B. Ding, Y. Wang, X. Hao, H. Dou, Y. Xia, X. Zhang, Pseudocapacitive materials for electrochemical capacitors: From rational synthesis to capacitance optimization, Natl. Sci. Rev. 4 (2017) 71–90. https://doi.org/10.1093/nsr/nww072.
[25] A.M. Bryan, L.M. Santino, Y. Lu, S. Acharya, J.M. D'Arcy, Conducting Polymers for Pseudocapacitive Energy Storage, Chem. Mater. 28 (2016) 5989–5998. https://doi.org/10.1021/acs.chemmater.6b01762.
[26] H.M. Jeong, J.W. Lee, W.H. Shin, Y.J. Choi, H.J. Shin, J.K. Kang, J.W. Choi, Nitrogen-doped graphene for high-performance ultracapacitors and the importance of nitrogen-doped sites at basal planes, Nano Lett. 11 (2011) 2472–2477. https://doi.org/10.1021/nl2009058.
[27] D. Hulicova-Jurcakova, M. Kodama, S. Shiraishi, H. Hatori, Z.H. Zhu, G.Q. Lu, Nitrogen-enriched nonporous carbon electrodes with extraordinary supercapacitance, Adv. Funct. Mater. 19 (2009) 1800–1809. https://doi.org/10.1002/adfm.200801100.
[28] H. Oda, A. Yamashita, S. Minoura, M. Okamoto, T. Morimoto, Modification of the

oxygen-containing functional group on activated carbon fiber in electrodes of an electric double-layer capacitor, J. Power Sources. 158 (2006) 1510–1516. https://doi.org/10.1016/j.jpowsour.2005.10.061.
[29] C. Vix-Guterl, E. Frackowiak, K. Jurewicz, M. Friebe, J. Parmentier, F. Béguin, Electrochemical energy storage in ordered porous carbon materials, Carbon N. Y. 43 (2005) 1293–1302. https://doi.org/10.1016/j.carbon.2004.12.028.
[30] A. Laforgue, P. Simon, J.F. Fauvarque, M. Mastragostino, F. Soavi, J.F. Sarrau, P. Lailler, M. Conte, E. Rossi, S. Saguatti, Activated carbon/conducting polymer hybrid supercapacitors, J. Electrochem. Soc. 150 (2003) 1–8. https://doi.org/10.1149/1.1566411.
[31] M.D. Stoller, S. Murali, N. Quarles, Y. Zhu, J.R. Potts, X. Zhu, H.W. Ha, R.S. Ruoff, Activated graphene as a cathode material for Li-ion hybrid supercapacitors, Phys. Chem. Chem. Phys. 14 (2012) 3388–3391. https://doi.org/10.1039/c2cp00017b.
[32] S.R. Sivakkumar, A.G. Pandolfo, Evaluation of lithium-ion capacitors assembled with pre-lithiated graphite anode and activated carbon cathode, Electrochim. Acta. 65 (2012) 280–287. https://doi.org/10.1016/j.electacta.2012.01.076.
[33] W.H. Low, P.S. Khiew, S.S. Lim, C.W. Siong, C.H. Chia, E.R. Ezeigwe, Facile synthesis of graphene-Zn 3 V 2 O 8 nanocomposite as a high performance electrode material for symmetric supercapacitor, J. Alloys Compd. 784 (2019) 847–858. https://doi.org/10.1016/j.jallcom.2019.01.137.
[34] C. Zhong, Y. Deng, W. Hu, J. Qiao, L. Zhang, J. Zhang, A review of electrolyte materials and compositions for electrochemical supercapacitors, Chem. Soc. Rev. 44 (2015) 7484–7539. https://doi.org/10.1039/c5cs00303b.
[35] M. Ue, Chemical Capacitors and Quaternary Ammonium Salts, Electrochemistry. 75 (2007) 565–572. https://doi.org/10.5796/electrochemistry.75.565.
[36] D. Jiménez-Cordero, F. Heras, M.A. Gilarranz, E. Raymundo-Piñero, Grape seed carbons for studying the influence of texture on supercapacitor behaviour in aqueous electrolytes, Carbon N. Y. 71 (2014) 127–138. https://doi.org/10.1016/j.carbon.2014.01.021.
[37] K. Torchała, K. Kierzek, J. Machnikowski, Capacitance behavior of KOH activated mesocarbon microbeads in different aqueous electrolytes, Electrochim. Acta. 86 (2012) 260–267. https://doi.org/10.1016/j.electacta.2012.07.062.
[38] V. Khomenko, E. Raymundo-Piñero, E. Frackowiak, F. Béguin, High-voltage asymmetric supercapacitors operating in aqueous electrolyte, Appl. Phys. A Mater. Sci. Process. 82 (2006) 567–573. https://doi.org/10.1007/s00339-005-3397-8.
[39] M. Galiński, A. Lewandowski, I. Stepniak, Ionic liquids as electrolytes, Electrochim. Acta. 51 (2006) 5567–5580. https://doi.org/10.1016/j.electacta.2006.03.016.
[40] H.A. Andreas, B.E. Conway, Examination of the double-layer capacitance of an high specific-area C-cloth electrode as titrated from acidic to alkaline pHs, Electrochim. Acta. 51 (2006) 6510–6520. https://doi.org/10.1016/j.electacta.2006.04.045.
[41] K. Fic, G. Lota, M. Meller, E. Frackowiak, Novel insight into neutral medium as electrolyte for high-voltage supercapacitors, Energy Environ. Sci. 5 (2012) 5842–5850. https://doi.org/10.1039/c1ee02262h.
[42] S. Ishimoto, Y. Asakawa, M. Shinya, K. Naoi, Degradation responses of activated-carbon-based EDLCs for higher voltage operation and their factors, J. Electrochem.

Soc. 156 (2009) 563–571. https://doi.org/10.1149/1.3126423.
[43] J. Yan, Q. Wang, T. Wei, Z. Fan, Recent advances in design and fabrication of electrochemical supercapacitors with high energy densities, Adv. Energy Mater. 4 (2014). https://doi.org/10.1002/aenm.201300816.
[44] J. Le Bideau, L. Viau, A. Vioux, Ionogels, ionic liquid based hybrid materials, Chem. Soc. Rev. 40 (2011) 907–925. https://doi.org/10.1039/c0cs00059k.
[45] H. Gao, K. Lian, High rate all-solid electrochemical capacitors using proton conducting polymer electrolytes, J. Power Sources. 196 (2011) 8855–8857. https://doi.org/10.1149/1.3647852.
[46] S.N. Syahidah, S.R. Majid, Super-capacitive electro-chemical performance of polymer blend gel polymer electrolyte (GPE) in carbon-based electrical double-layer capacitors, Electrochim. Acta. 112 (2013) 678–685. https://doi.org/10.1016/j.electacta.2013.09.008.
[47] A.A. Łatoszyńska, G.Z. Zukowska, I.A. Rutkowska, P.L. Taberna, P. Simon, P.J. Kulesza, W. Wieczorek, Non-aqueous gel polymer electrolyte with phosphoric acid ester and its application for quasi solid-state supercapacitors, J. Power Sources. 274 (2015) 1147–1154. https://doi.org/10.1016/j.jpowsour.2014.10.094.
[48] Q. Chen, X. Li, X. Zang, Y. Cao, Y. He, P. Li, K. Wang, J. Wei, D. Wu, H. Zhu, Effect of different gel electrolytes on graphene-based solid-state supercapacitors, RSC Adv. 4 (2014) 36253–36256. https://doi.org/10.1039/c4ra05553e.
[49] Y.D. Chiou, D.S. Tsai, H.H. Lam, C.H. Chang, K.Y. Lee, Y.S. Huang, Cycle stability of the electrochemical capacitors patterned with vertically aligned carbon nanotubes in an LiPF6-based electrolyte, Nanoscale. 5 (2013) 8122–8129. https://doi.org/10.1039/c3nr01980b.
[50] G. Lota, E. Frackowiak, Striking capacitance of carbon/iodide interface, Electrochem. Commun. 11 (2009) 87–90. https://doi.org/10.1016/j.elecom.2008.10.026.
[51] L. Chen, H. Bai, Z. Huang, L. Li, Mechanism investigation and suppression of self-discharge in active electrolyte enhanced supercapacitors, Energy Environ. Sci. 7 (2014) 1750–1759. https://doi.org/10.1039/c4ee00002a.
[52] M. Beidaghi, Y. Gogotsi, Capacitive energy storage in micro-scale devices: Recent advances in design and fabrication of micro-supercapacitors, Energy Environ. Sci. 7 (2014) 867–884. https://doi.org/10.1039/c3ee43526a.
[53] Z.L. Wang, Toward self-powered sensor networks, Nano Today. 5 (2010) 512–514. https://doi.org/10.1016/j.nantod.2010.09.001.
[54] I.F. Akyildiz, W. Su, Y. Sankarasubramaniam, E. Cayirci, Wireless sensor networks a survey, Comput. Networks. 38 (2002) 393–422. https://doi.org/10.1016/S1389-1286(01)00302-4.
[55] J.J. Yoo, K. Balakrishnan, J. Huang, V. Meunier, B.G. Sumpter, A. Srivastava, M. Conway, A.L. Mohana Reddy, J. Yu, R. Vajtai, P.M. Ajayan, Ultrathin planar graphene supercapacitors, Nano Lett. 11 (2011) 1423–1427. https://doi.org/10.1021/nl200225j.
[56] Z. Bo, W. Zhu, W. Ma, Z. Wen, X. Shuai, J. Chen, J. Yan, Z. Wang, K. Cen, X. Feng, Vertically oriented graphene bridging active-layer/current-collector interface for ultrahigh rate supercapacitors, Adv. Mater. 25 (2013) 5799–5806. https://doi.org/10.1002/adma.201301794.
[57] Q. Cheng, J. Tang, J. Ma, H. Zhang, N. Shinya, L.C. Qin, Graphene and carbon

nanotube composite electrodes for supercapacitors with ultra-high energy density, Phys. Chem. Chem. Phys. 13 (2011) 17615–17624. https://doi.org/10.1039/c1cp21910c.
[58] M. Beidaghi, C. Wang, Micro-supercapacitors based on interdigital electrodes of reduced graphene oxide and carbon nanotube composites with ultrahigh power handling performance, Adv. Funct. Mater. 22 (2012) 4501–4510. https://doi.org/10.1002/adfm.201201292.
[59] D. Pech, M. Brunet, H. Durou, P. Huang, V. Mochalin, Y. Gogotsi, P.L. Taberna, P. Simon, Ultrahigh-power micrometre-sized supercapacitors based on onion-like carbon, Nat. Nanotechnol. 5 (2010) 651–654. https://doi.org/10.1038/nnano.2010.162.
[60] M.F. El-Kady, R.B. Kaner, Scalable fabrication of high-power graphene micro-supercapacitors for flexible and on-chip energy storage, Nat. Commun. 4 (2013) 1475–1479. https://doi.org/10.1038/ncomms2446.
[61] S. Wang, Z.S. Wu, S. Zheng, F. Zhou, C. Sun, H.M. Cheng, X. Bao, Scalable Fabrication of Photochemically Reduced Graphene-Based Monolithic Micro-Supercapacitors with Superior Energy and Power Densities, ACS Nano. 11 (2017) 4283–4291. https://doi.org/10.1021/acsnano.7b01390.
[62] Z. Niu, L. Zhang, L. Liu, B. Zhu, H. Dong, X. Chen, All-solid-state flexible ultrathin micro-supercapacitors based on graphene, Adv. Mater. 25 (2013) 4035–4042. https://doi.org/10.1002/adma.201301332.
[63] D. Pech, M. Brunet, P.L. Taberna, P. Simon, N. Fabre, F. Mesnilgrente, V. Conédéra, H. Durou, Elaboration of a microstructured inkjet-printed carbon electrochemical capacitor, J. Power Sources. 195 (2010) 1266–1269. https://doi.org/10.1016/j.jpowsour.2009.08.085.
[64] W. Gao, N. Singh, L. Song, Z. Liu, A.L.M. Reddy, L. Ci, R. Vajtai, Q. Zhang, B. Wei, P.M. Ajayan, Direct laser writing of micro-supercapacitors on hydrated graphite oxide films, Nat. Nanotechnol. 6 (2011) 496–500. https://doi.org/10.1038/nnano.2011.110.
[65] Y. Zhang, L. Guo, S. Wei, Y. He, H. Xia, Q. Chen, H.B. Sun, F.S. Xiao, Direct imprinting of microcircuits on graphene oxides film by femtosecond laser reduction, Nano Today. 5 (2010) 15–20. https://doi.org/10.1016/j.nantod.2009.12.009.
[66] J. Lin, Z. Peng, Y. Liu, F. Ruiz-Zepeda, R. Ye, E.L.G. Samuel, M.J. Yacaman, B.I. Yakobson, J.M. Tour, Laser-induced porous graphene films from commercial polymers, Nat. Commun. 5 (2014) 1–8. https://doi.org/10.1038/ncomms6714.
[67] F. Cai, C.A. Tao, Y. Li, W. Yin, X. Wang, J. Wang, Effects of amount of graphene oxide and the times of LightScribe on the performance of all-solid-state flexible graphene-based micro-supercapacitors, Mater. Res. Express. 4 (2017). https://doi.org/10.1088/2053-1591/aa65fb.
[68] R. Ye, D.K. James, J.M. Tour, Laser-Induced Graphene: From Discovery to Translation, Adv. Mater. 31 (2019) 1–15. https://doi.org/10.1002/adma.201803621.
[69] N. Kurra, Q. Jiang, P. Nayak, H.N. Alshareef, Laser-derived graphene: A three-dimensional printed graphene electrode and its emerging applications, Nano Today. 24 (2019) 81–102. https://doi.org/10.1016/j.nantod.2018.12.003.
[70] A. Longo, R. Verucchi, L. Aversa, R. Tatti, A. Ambrosio, E. Orabona, U. Coscia, G. Carotenuto, P. Maddalena, Graphene oxide prepared by graphene nanoplatelets and reduced by laser treatment, Nanotechnology. 28 (2017) 224002. https://doi.org/10.1088/1361-6528/aa6c3c.

[71] A. Lamberti, M. Serrapede, G. Ferraro, M. Fontana, F. Perrucci, S. Bianco, A. Chiolerio, S. Bocchini, All-{SPEEK} flexible supercapacitor exploiting laser-induced graphenization, 2D Mater. 4 (2017) 35012. https://doi.org/10.1088/2053-1583/aa790e.

[72] R. Ye, Y. Chyan, J. Zhang, Y. Li, X. Han, C. Kittrell, J.M. Tour, Laser-Induced Graphene Formation on Wood, Adv. Mater. 29 (2017) 1–7. https://doi.org/10.1002/adma.201702211.

[73] Y. Chyan, R. Ye, Y. Li, S.P. Singh, C.J. Arnusch, J.M. Tour, Laser-Induced Graphene by Multiple Lasing: Toward Electronics on Cloth, Paper, and Food, ACS Nano. 12 (2018) 2176–2183. https://doi.org/10.1021/acsnano.7b08539.

[74] R. Ye, Z. Peng, T. Wang, Y. Xu, J. Zhang, Y. Li, L.G. Nilewski, J. Lin, J.M. Tour, In Situ Formation of Metal Oxide Nanocrystals Embedded in Laser-Induced Graphene, ACS Nano. 9 (2015) 9244–9251. https://doi.org/10.1021/acsnano.5b04138.

[75] L. Li, J. Zhang, Z. Peng, Y. Li, C. Gao, Y. Ji, R. Ye, N.D. Kim, Q. Zhong, Y. Yang, H. Fei, G. Ruan, J.M. Tour, High-Performance Pseudocapacitive Microsupercapacitors from Laser-Induced Graphene, Adv. Mater. 28 (2016) 838–845. https://doi.org/10.1002/adma.201503333.

*This page intentionally left blank*

# 4 Experimental methods and materials characterization

The combination of $TiO_2$ and graphene was carried out to develop promising materials to be used as electrodes in lithium-ion batteries and micro-supercapacitors.

The first section of the chapter will focus on the experimental procedure to obtain the composite materials and on the production of the devices. The following section will describe the characterization techniques and the electrochemical test conditions.

## 4.1 Materials for anodes of Li-ion batteries

The $TiO_2$-graphene materials were synthesized in order to test their electrochemical performance as active materials in electrode in Li-ion batteries. The enhancement in the performance of the combination of the two materials is compared to that of pristine $TiO_2$. The effects of the use of graphene will be evaluated in the following chapters.

The $TiO_2$-graphene materials have been prepared starting from the graphene synthesis. Afterwards, the decoration of graphene has been obtained through the *in situ* synthesis of $TiO_2$ nanoparticles onto the graphene sheets.

### 4.1.1 Graphene synthesis

Graphene has been synthesized through the thermal exfoliation of graphite oxide, starting from graphite [1,2]. An atomistic model of graphite, graphite oxide and thermally exfoliated graphite oxide is reported in figure 4.1 from [3].

First, graphite was oxidized following the Brodie method [4], using graphite powder as starting material (SGL Carbon, RW-A grade, average size 66 μm), which was mixed with sodium chlorate powder ($NaClO_3$, Sigma-Aldrich Co.) and cooled with an ice-bath in a fume-hood. Fuming nitric acid ($HNO_3$, ≥99.5%, Sigma-Aldrich Co.) was slowly added to the solution under continuous stirring, ensuring that the change in temperature is minimal. The oxidative reaction was carried out under nitrogen flux to avoid the formation of explosive by-products, containing dichlorine monoxide ($Cl_2O$) and chlorites (containing $ClO_2^-$ group). Then, the suspension was heated at 60 °C with a slow thermal ramp (30 °C/h), dwelling time of 8 h and cooled at room temperature (RT). The product, which appeared green, was washed with deionized Milli-Q water and filtered through a Büchner funnel. It was further suspended in a diluted hydrochloric acid solution (HCl, 37%, Sigma-Aldrich Co.) and filtered. An additional washing with deionized Milli-Q water was performed until reaching the final pH of 7 in the solution. Finally, the product was dried at 60 °C overnight. The amount of graphite oxide, obtained after the oxidation process, is about 50% higher than the initial mass of graphite powder, due to the insertion of functional groups into graphite atomic planes, such as hydroxyl, epoxy and carboxyl groups, as depicted in figure 4.1b.

To produce graphene, the obtained graphite oxide (GO) was exposed to a thermal exfoliation at high temperature under dynamic vacuum. Powdered GO was put in a quartz vial under dynamic vacuum ($10^{-4}$ mbar) and quickly put into a tube furnace at 1150 °C for 30 minutes. The sudden thermal shock promotes the detachment and the decomposition of functional groups, which are converted in gaseous CO and $CO_2$. The production of these gases leads to the separation of graphite planes, visible from a volume expansion of the powder. This synthesis method can produce gram-scale of Thermally Exfoliated Graphite Oxide (hereafter called *TEGO*), made up of fluffy flakes (figure 4.2), with an high amount of reactive defects [5], such as carbon vacancies in the graphene surface or line defects (figure 4.3) [6,7]. After the exfoliation, graphene was removed from the quartz tube under oxygen- and moisture-free conditions in an argon filled glove-box (<0.5 ppm of $O_2$ and $H_2O$) (MBraun Labmaster 130), in order to avoid undesired reactions of the defects with oxygen or water.

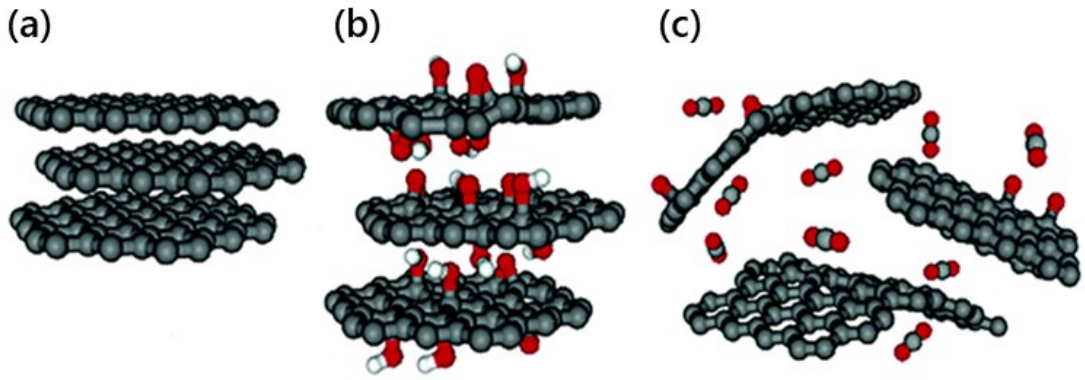


*Figure 4.1 Schematic representation of (a) graphite, (b) graphite oxide and (c) thermally exfoliated graphite oxide* [3].

*Figure 4.2 TEGO flakes*

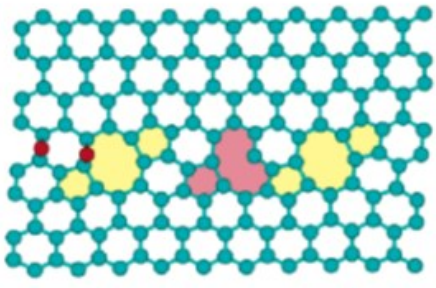

*Figure 4.3 Atomistic representation of graphene with line defects: a single carbon vacancy with the formation of a pentagon ring is highlighted in pink; the 5-8-5 defects created by the coalescence of two single carbon vacancies are highlighted in yellow; in red two epoxy groups are also shown* [6].

### 4.1.2 $TiO_2$-decorated graphene synthesis

The $TiO_2$-TEGO materials were obtained from two different approaches: a chemical route for the growth of $TiO_2$ nanoparticles onto the graphene sheets (TEGO), via hydrothermal synthesis and a solid-state grinding of $TiO_2$ nanoparticles and graphene, through high-energy ball milling.

#### 4.1.2.1 Hydrothermal synthesis

The hydrothermal synthesis has been carried out to synthesize $TiO_2$ nanoparticles onto graphene (TEGO) surface in order to obtain $TiO_2$-TEGO materials to be tested as electrode material in Li-ion batteries. In figure 4.4 a schematic representation of the synthesis procedure is illustrated.

In the hydrothermal synthesis, graphene (TEGO) and titanium(IV) isopropoxide (TTIP, 97%, Sigma-Aldrich Co.), as titanium dioxide precursor, were used as reagents. Anhydrous tetrahydrofuran (THF, 99.9%) was chosen as organic solvent to promote the dispersion of the reagents.

In the Ar glove-box, graphene flakes were put into a Pyrex glass Rotaflo vial. Besides, degassed anhydrous THF has been prepared into a different Pyrex Rotaflo vial. Taken the vial containing graphene out of the glove-box, it was connected to the vial containing the solvent, under a pressure lower than $10^{-4}$ mbar. To promote the dispersion of TEGO in the solvent, the THF was condensed into the synthesis vial, by immersion in liquid nitrogen, under continuous stirring. When graphene was completely soaked by the solvent, the liquid nitrogen immersion was removed to reach RT.

Besides, in an inert argon atmosphere, TTIP was inserted into a Pyrex Rotaflo vial and dispersed in THF. After a few minutes of sonication, the content of the vial was mixed with TEGO, without air exposure. The mixture was kept under further continuous stirring overnight at RT to ensure the complete dispersion of the reagents. Then, the solvent was condensed from the synthesis vial under the as-above adopted conditions. The black product was recovered from the vial in the glove-box, to avoid air exposure.

An appropriate amount of powder, typically the needed quantity to realize the electrode material (~80 mg), was prepared for the hydrothermal reaction, carried out into a stainless-steel autoclave. The powder was put into a small Pyrex glass vial, standing inside the Teflon

chamber. Deionized Milli-Q water was inserted in the cavity between the Pyrex vial and the Teflon one, avoiding any water contact with the powder. Finally, the autoclave system was sealed through its flanges and taken it out from the glove-box. The hydrothermal reaction was carried out into a furnace at 180 °C for 17 h [8]. Afterwards, the autoclave was naturally cooled at RT and the powder was collected and dried overnight at 60 °C to promote the evaporation of water and residual solvent from the reaction. The final $TiO_2$-TEGO material is black powdered.

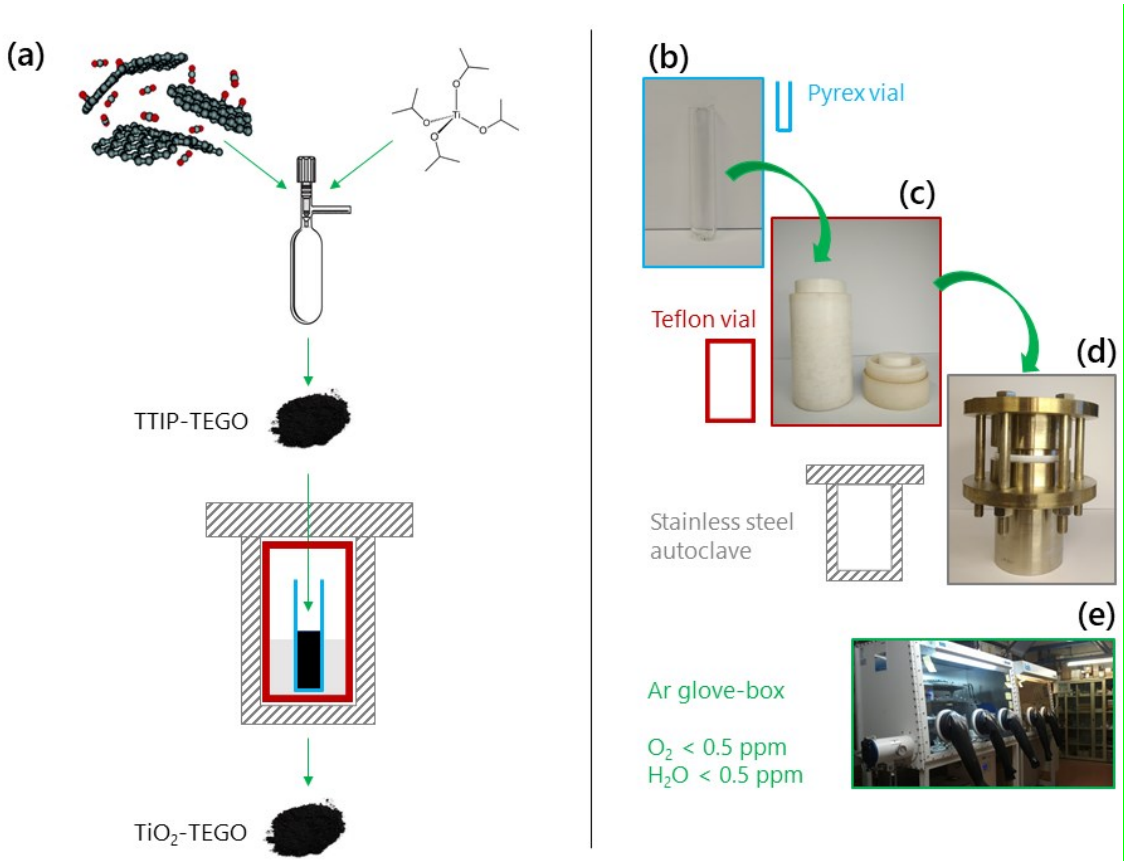


*Figure 4.4 (a) Schematic representation of the hydrothermal synthesis procedure; pictures of the instrumentation: (b) Pyrex vial, (c) Teflon vial, (d) stainless steel autoclave and (e) Ar filled glove-box.*

The $TiO_2$-TEGO material was synthesized in two different $TiO_2$:TEGO relative concentrations, in order to test its electrochemical performance as electrode in Li-ion batteries. The $TiO_2$:TEGO weight percentages (wt%) of 99:1 and 80:20 were compared.

Pristine $TiO_2$ was synthesized as a reference, without the use of graphene. The synthesis of $TiO_2$ was also performed via the hydrothermal method, without mixing it with TEGO. TTIP was directly inserted into the small Pyrex glass vial and the autoclave was assembled in the same conditions, as for the $TiO_2$-TEGO synthesis. Reaction settings were maintained as the previous ones. The as-prepared pristine hydrothermally synthesized $TiO_2$ will be henceforth called *$TiO_2$-HT* (HT stands for "HydroThermal").

#### 4.1.2.2 High-energy ball milling treatment

The high-energy ball milling treatment has been exploited to compare a chemically synthesized $TiO_2$-TEGO material with a composite product obtained via a solid-state method. The latter approach promotes the combination of the materials in a straightforward process without using solvents, as a cost-effective method.

The high-energy ball milling treatment was performed inside a 10 ml agate bowl of a FRITSCH Mini-Mill PULVERISETTE 23 vibratory mill, equipped with three agate balls. Graphene (TEGO) and Aeroxide $TiO_2$ P25 (Evonik) were used as reagents.

Since TEGO is made up of fluffy flakes, the volume of TEGO flakes was first reduced through dispersion in THF, as previously described in section 4.1.2.1, obtaining a black powder with a smaller volume. Then, TEGO and $TiO_2$ P25 were inserted in the agate bowl in the $TiO_2$:TEGO weight ratio of 80:20, for a total amount of powder of about 100 mg. The sample underwent milling treatment at 30 Hz frequency for 30 minutes, leaving 5 minutes rest every 10 minutes of milling. Then, the black product was recovered from the agate bowl.

## 4.2 Li-ion half cells production

$TiO_2$-TEGO materials obtained from the above-mentioned preparations were tested as electrode in lithium ion batteries in half cells, in order to evaluate the electrochemical performance of the materials.

The production of the electrodes was performed by casting a wet slurry on an aluminium foil substrate. The slurries were prepared by mixing $TiO_2$-TEGO with conductive carbon black (CB, Timcal, Super 65) and polyvinylidene fluoride binder (PVDF, Solvay, Solef® 5310) in the weight proportion of 80:10:10. The reagents were thoroughly crushed in a mortar and N-methyl-pyrrolidone (NMP, anhydrous 99.5%, Sigma-Aldrich Co.) was dropwise added to

obtain a dense slurry. Then, the mixture was spread onto an aluminium foil by a notch bar (0.3 mm thickness). Evaporation of the solvent was first performed on a 70 °C hot plate for a few minutes, then in a 70 °C vacuum oven overnight. The obtained film was pressed in a hydraulic press, then punched in discs of 7 mm diameter. The round electrodes were further dried at 70 °C overnight.

The electrodes were tested in half-cell configuration assembled in stainless steel coin-cells (CR2032, Tmax Battery Equipments) (figure 4.5). The assembly of the cell was made in glove-box, to avoid any water and oxygen contamination. The liquid electrolyte, as well prepared in glove-box, consists of a 1 M lithium hexafluorophosphate ($LiPF_6$, ≥99.99%, battery grade, Sigma Aldrich Co.) solution in ethyl carbonate (EC) and dimethyl carbonate (DMC) 1:1 %v/v. The electrode, containing about 1-2 mg of active material, was placed on the positive case. Above it, the Celgard separator was added and wetted with a few drops of the electrolyte solution. On top of them, a punched 7 mm disc of metal Li (Li ribbon, 99.9%, Sigma-Aldrich Co.) was placed as counter-electrode. Then, the coin-cell was sealed with the spacer, the spring and the negative case. The sealed cell was clamped in a vice and taken it out of the glove-box and further pressed in a hydraulic press [9].

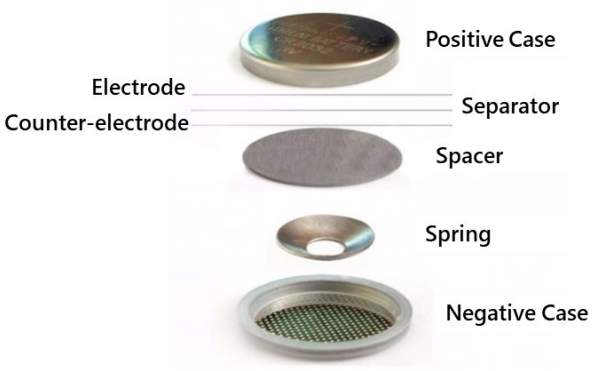


*Figure 4.5 Schematic representation of the architecture of a CR2032 coin cell.*

It is worth noting that in half-cell configuration, the counter electrode, which is made up of lithium metal, represents the anode of the device, due to its lowest reduction potential (-3.04 V vs SHE, Standard hydrogen electrode). Conversely, the $TiO_2$-TEGO based electrode is considered as cathode in this configuration. However, it should be mentioned that $TiO_2$-

graphene based materials are typically used as anode in LIBs, combined with conventional cathode materials, having higher reduction potential.

Here, the general term *electrode* will be used referring to the electrode containing $TiO_2$-TEGO combined material, whereas the *counter-electrode* to lithium metal.

## 4.3 Materials for electrodes of micro-supercapacitors

The combination of $TiO_2$ and graphene was investigated to develop electrode materials for micro-supercapacitors, in the attempt to improve the electrochemical performance of pristine graphene-based electrodes, through the introduction of Faradaic effects by $TiO_2$.

Here, as previously mentioned in section 3.6.1, LightScribe® technology was used as a straightforward method for the production of the composite material, namely consisting of nanostructured $TiO_2$ and graphene-based material.

### 4.3.1 LightScribe mask production

Micro-supercapacitors (MSCs) were obtained by the Lightscribe® technique introduced by Kaner and his group [10] with a planar structure, in which both the electrodes are made of Laser-Scribed Graphite Oxide (LSGO) combined with $TiO_2$ nanoparticles. Compared to the technique used by Kaner, here a novel approach has been exploited to promote the simultaneous synthesis of a composite material, based on nanocrystalline $TiO_2$ and graphene.

$TiO_2$-LSGO micro-supercapacitors (MSCs) were produced with a *one pot* formation of $TiO_2$ nanoparticles (NPs) and Laser-Scribed Graphite Oxide (LSGO) patterns, using a LightScribe DVD burner laser. The preparation of the reagents is here described.

An aqueous dispersion of graphite oxide (GO-V50, Standard Graphene) with a concentration of 2 mg/ml was kept under sonication for 8 h (30 minutes rest every 30 minutes of sonication in order to avoid heating effect). Afterwards, titanium(IV) isopropoxide (TTIP, 97%, Sigma-Aldrich Co.) was added as $TiO_2$ precursor in a TTIP:GO weight ratio of 1.2:1. The dispersion was kept under sonication for 30 min, then it was kept under continuous stirring for 3 h, under argon atmosphere. A volume of 5 ml of the dispersion was then drop-cast on a polyethylene terephthalate (PET) disc (0.1 mm thick) and

let it dry overnight under argon atmosphere, forming a film ~10 µm thick. Then, the PET disc was glued to the surface of a LightScribe DVD disc. The TTIP-GO-coated disc was laser-scribed by the infrared laser of the LightScribe DVD burner. Interdigitated patterns were drawn using the LightScribe *Nero CoverDesigner* software and they were written (*laser-scribed*) on the coated PET disc in a scribing time of about 20 minutes. To ensure that the patterns were fully laser-scribed, the number of laser-scribe times was adjusted to two or three. The schematic representation of the LightScribe mask production is illustrated in figure 4.6. In the LightScribe® process the infrared light of the DVD burner laser (λ=780 nm) simultaneously converts the GO-V50 and the TTIP precursors into LSGO and $TiO_2$ NPs, respectively, in correspondence of the interdigitated patterns. The spaces between the patterns are not converted, remaining unchanged. The $TiO_2$-LSGO patterns obtained by the LightScribe® process are shown in figure 4.7.

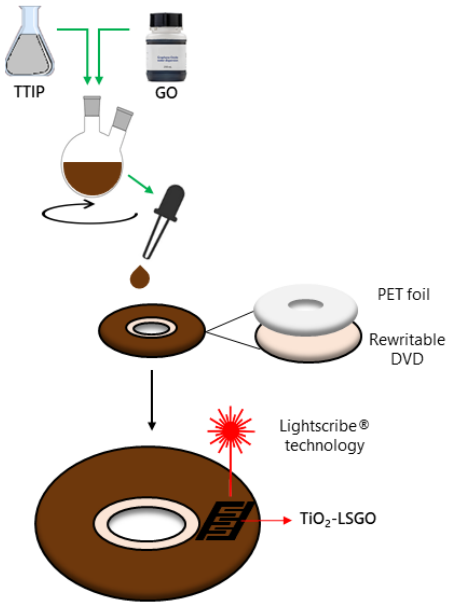


*Figure 4.6 Scheme of the preparation of LightScribe mask. Sections pointed by green arrows were performed under argon atmosphere.*

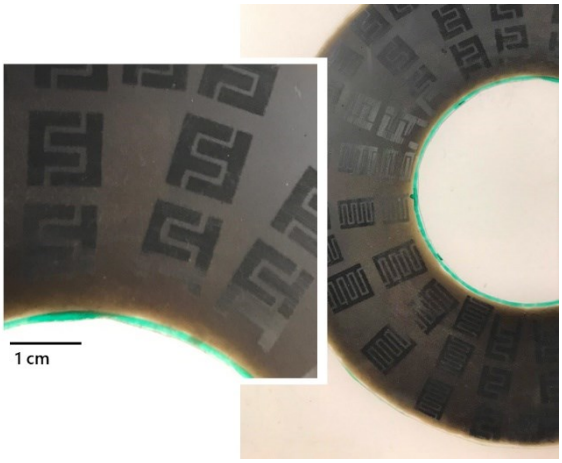


*Figure 4.7 Picture of a Laser-Scribed DVD. In the square, a detail of the DVD shows the interdigitated patterns.*

## 4.4 $TiO_2$-LSGO micro-supercapacitors production

The $TiO_2$-LSGO patterns were used as micro-supercapacitors electrodes, whereas the unconverted parts served as separator. To investigate the electrochemical performance of the micro-devices, copper tape was glued to the edge of the electrodes using silver paint. The interdigitated area was bordered by Teflon® tape to keep separate the contacts from the electrolyte. A hydrogel polymer electrolyte was used. The electrolyte was prepared with an aqueous solution of water:acid:polymer in the mass ratio of 84:8:8, respectively. Two different gel electrolytes were tested, using $H_2SO_4$/polyvinyl alcohol (PVA) and $H_3PO_4$/PVA (Sigma-Aldrich Co.). The concentrated acid and deionized Milli-Q water were mixed and PVA powder was added under continuous stirring. The solution was heated to about 85 °C until it became clear. The electrolyte was drop-cast onto the surface of the interdigitated area and let it dry overnight to make the excess water evaporate. Thus, the $TiO_2$-LSGO MSCs were obtained. The schematic production of $TiO_2$-LSGO MSCs is depicted in figure 4.8.

To investigate the effect of $TiO_2$ nanoparticles on the devices, micro-supercapacitors without $TiO_2$ were prepared following the same procedure. The aqueous dispersion was prepared with graphite oxide (GO-V50, Standard Graphene) as previously described in section 4.3.1, without the addition of the $TiO_2$ precursor. Then, the same production process was followed for LSGO MSCs production.

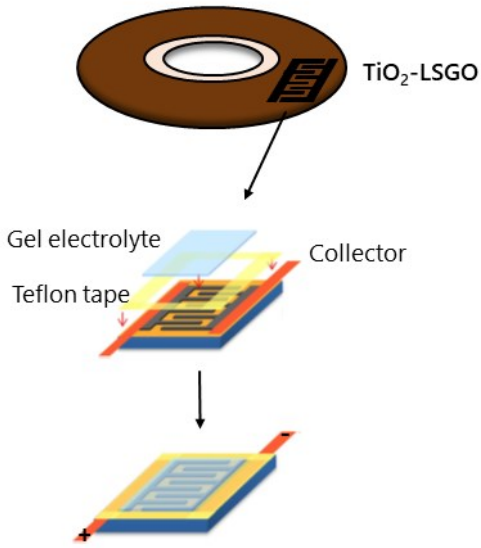


*Figure 4.8 Scheme of the production of $TiO_2$-LSGO MSCs* [10].

## 4.5 Characterization of the materials

The micro-structure of the materials was analyzed in order to obtain morphological and structural information. Specifically, the investigation in $TiO_2$ were aimed at the identification of crystalline phases and determination of their weight fractions, as well as their morphology and nanoscale structure. Regarding the graphene-based materials, structural properties, chemical composition and electrical properties were investigated.

The micro-structure of the combined $TiO_2$-TEGO materials were analyzed by powder X-ray diffraction, transmission electron microscopy and Raman spectroscopy, whereas the micro-structure of $TiO_2$-LSGO materials were investigated by X-ray photoelectron spectroscopy, transmission electron microscopy and Raman spectroscopy.

The electrical properties of the graphene-based materials were investigated by electrical resistance measurements by means of four-point probes method.

### 4.5.1 Powder X-Ray Diffraction

Powder X-Ray Diffraction (PXRD) was used as a powerful technique to determine the crystalline phases in the materials. In addition, for nanostructured materials, PXRD was employed to obtain information about the crystallite size.

The total broadening of the diffraction reflections depends both on the broadening due to micro-structural factors such as crystallite size and lattice disorder, as well as on the instrumental broadening.

Nanocrystalline size and micro-strains produce peaks broadening in powder X-ray diffraction patterns. As the crystallite size decreases, the coherence of scattered X-rays is reduced. The fewer crystallographic planes in small crystals induce a slight phase shift in the scattered radiation which is not suppressed, as in ideally infinite crystals, by destructive interference effects due to atomic planes from the bulk (figure 4.9). The resulting phase shift determines the broadening of Bragg peaks [11].

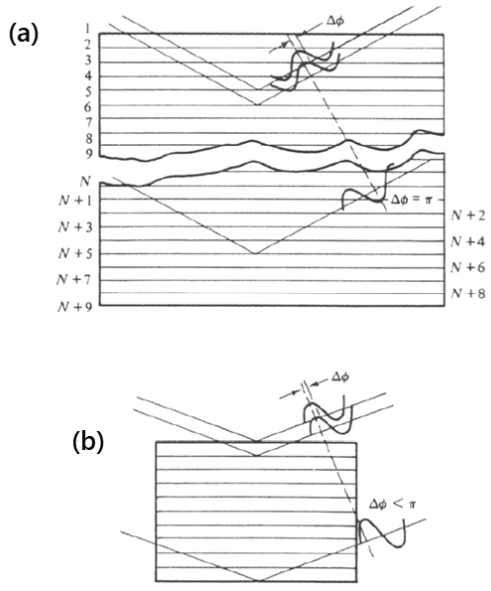


*Figure 4.9 Origin of diffraction peak broadening with the comparison between (a) large crystal and (b) finite crystal* [11].

Several methods can be used to estimate the average crystallite size from the analysis of the broadening of the diffraction peak. Among them, the semi-empirical relation between the crystallite size and the peak broadening is expressed by the Scherrer equation:

$$d_{hkl} = \frac{k\lambda}{B\cos\theta} \qquad (4.1)$$

The average crystallite size $d_{hkl}$ normal to the plane (*hkl*) is estimated from the structural broadening *B* of the peak profile, where $\lambda$ is the X-ray wavelength, *k* is the Scherrer constant, considering the crystals shape, and $\theta$ is the Bragg diffraction angle (expressed in radians) [12]. The total broadening of peak profile $B_{total}$, measured by using the full width at half maximum of the (*hkl*) diffraction peak, is affected by both the structural broadening *B* of the sample and the instrumental broadening $B_{inst}$, according to the following:

$$B^2 = B_{total}^2 - B_{inst}^2 \qquad (4.2)$$

Besides, inhomogeneous strains are common in nanocrystalline materials. Inhomogeneous strains, which are caused by structural defects, interstitial and vacant atoms, dislocations and faultings, also affects the peak broadening. In strained crystallites, the interplanar spaces is changed, resulting in smaller or larger spacings in the case of compressive or tensile stresses. If the strain is inhomogeneous, namely different spacing occurs in the crystallites, a distribution of values in the Bragg angle is noticed, according to the Bragg law:

$$2d\sin\theta = n\lambda \qquad (4.3)$$

where *d* is the spacing of crystal lattice planes, $\theta$ is the Bragg diffraction angle, *n* is the reflection order and $\lambda$ is the X-ray wavelength. Therefore, this effect results in a peak broadening.

Room temperature powder X-ray diffraction (PXRD) patterns were collected with a Bruker D2 Phaser powder diffractometer, equipped with a Cu $K_\alpha$ radiation (λ=1.54178 Å) and a 1D LYNXEYE detector. Diffraction measurements were performed in a θ-θ focalizing geometry, in the range of 2θ from 15° to 60°, with a 0.018° step, working at 30 kV and 10 mA. The powdered samples were sieved with a 63 μm mesh to homogeneously spread out the sample onto a zero background silicon sample holder. Diffractograms were identified using the Bruker EVA software. The average crystallite size $d_{hkl}$ has been estimated by the Scherrer equation (eq. 4.1) in the spherical approximation, using $k = 0.89$ as shape constant.

### 4.5.2 Transmission Electron Microscopy

Transmission Electron Microscopy (TEM) investigations were carried out to analyze the morphology of the $TiO_2$-graphene based materials and to cross-check the crystallite size evaluated by PXRD and Raman spectroscopy.

TEM observations were performed with a high-resolution field emission JEM-2200FS microscope (JEOL Ltd., Japan), equipped with a Schottky gun working at 200 kV (point resolution 0.19 nm), an in-column energy filter (Ω-type), a CCD high resolution camera, STEM detectors, and an EDX detector. A small amount of sample was dispersed in isopropanol and a droplet of the suspension was deposited onto holey carbon films on copper grids. For $TiO_2$-TEGO materials, the powder obtained from the preparation was used, whereas for $TiO_2$-LSGO the material was scratched from the laser-scribed disc. Scanning transmission electron microscopy (STEM) images with strong Z-contrast were used to analyze the nanoparticles size distribution, by using the *ImageJ* software.

### 4.5.3 Micro-Raman spectroscopy

Micro-Raman spectroscopy was used first for the identification of the compounds in the composite $TiO_2$-graphene based materials as a confirmation of results from other techniques. In addition, changes in the shape of $TiO_2$ Raman spectra were strongly correlated with nanocrystals dimension.

In a perfect and infinite crystal, the Raman scattering involves only center-zone phonons. This is due to the conservation of momentum law $K_0 = K_i \pm Q$, where *Ko* and *Ki* are the momentum of the scattered and incoming photons and Q is the phonon momentum. This means that the maximum momentum *Q* of the involved phonon is *2Ko*, in backscattering geometry. Using visible light, the maximum value of *Q* is then in the order of $10^{-5}$ $cm^{-1}$, very small respect to the dimension of the Brillouin zone. Only the center-zone frequency is then associated to every phonon during the Raman scattering, producing well defined peaks. This is equivalent to say that the wavelength of the Raman phonons in perfect crystals is infinite (all the cells are vibrating in phase). The phonons are completely delocalized in space but well defined in momentum.

If the periodicity is broken, as in the case of finite size crystals, the phonons are confined. This means that contributions with finite wavelengths (and larger Q) should be taken into account. Not only center-zone phonons are involved in the Raman scattering. The

vibrational Raman peak is then no more a single sharp Lorentzian, as in the case of infinite crystals, but becomes a convolution of many contributions, following the phonon dispersion curve, broadening and shifting. The range of involved Q increases as the size of the crystal decreases. The phonon confinement becomes important, producing visible effects on the Raman spectra, for crystals sizes under 15-20 nm (it depends on the slope of the phonon dispersion curve). In the extreme case, in a completely disordered system as a glass, the intensity of the Raman bands will follow the phonon density of states, involving all possible Q values.

A model to correlate the position and width of the main Raman band of $TiO_2$ anatase was published by Bersani et al. and can be used to estimate the size of titania nanocrystals, in absence of other broadening and shift mechanisms (pressure, disorder, non-stoichiometry) [13].

Micro-Raman spectroscopy was performed with a Horiba LabRam micro-spectrometer (HORIBA Scientific, Kyoto, Japan), equipped with an Olympus microscope (Olympus, Tokyo, Japan), using a 50x objective, in a backscattering geometry. The 473.1 nm line of a doubled Nd:YAG laser and a 632.8 nm line of a He-Ne laser were used as excitation, with a spectral resolution of ~2.0 and ~1.0 $cm^{-1}$, respectively. The 473.1 nm line was used to investigate the graphene derivative bands, whereas the 632.8 nm line was used to detect $TiO_2$ signals with higher resolution.

The uncertainty in the peak position and in the linewidth of $TiO_2$ peaks are considered as half of the spectral resolution, after ensuring that the dispersions of their values, calculated in at least 10 points of the sample, are far lower. Otherwise, the contribution to the shift and the broadening from a dispersion of the crystallites size have been considered.

To avoid heating effects on the samples, the laser excitation power was lowered by means of density filters. The system was calibrated with the 520.6 $cm^{-1}$ Raman band of silicon in the low wavenumber range, while in the high wavenumber range the calibration was made by using spectral lamps. Deconvolution of Raman peaks were performed by the built-in *LabSpec 5* software.

### 4.5.4 X-ray Photoelectron Spectroscopy

Surface characterization has been carried out in an ultra-high vacuum (UHV) apparatus equipped with different surface electron spectroscopy techniques: X-ray Photoelectron

Spectroscopy (XPS), Ultraviolet Photoelectron Spectroscopy (UPS) and Auger Electron Spectroscopy (AES).

XPS was performed on $TiO_2$-graphene based materials to evaluate chemical properties of the surface. In order to preserve the surface, the samples were sealed in vials, and they were opened only when mounted on the surface characterization sample holder, before being introduced into UHV. Powders were supported on a carbon tape (UHV compatible). XPS has been carried out in a UHV apparatus equipped with an X-ray source (Mg $K_\alpha$ photon at 1253.6eV), while photoelectrons are analyzed through a VSW HA100 hemispherical analyzer with a total energy resolution of 0.86 eV. Core level binding energies (BE) have been normalized using as reference the Au 4f7/2 core level signal at 84 eV, acquired from a sputtered gold foil.

### 4.5.5 Electrical measurements

Electrical measurements were performed on graphene-based materials to obtain information about the conductivity. The electrical resistance of graphene derivative materials was measured on a thin sheet by four-point probes method. The measurements were carried out using a Keithley 6221 DC and AC current source and a Keithley 2182A Nanovoltmeter. The four probes consist of gold points aligned. The electrical resistivity $\rho$ was calculated with the:

$$\rho = \frac{\pi}{\ln(2)} \frac{V}{I} s \qquad (4.4)$$

where $s$ is the sheet thickness, $V$ and $I$ are the voltage drop and the current through the sample, respectively [14]. The electrical conductivity $\sigma$ (S/cm) was obtained as the reciprocal of the electrical resistivity, $\sigma = 1/\rho$.

## 4.6 Electrochemical characterization

The electrochemical properties of the combined materials, namely $TiO_2$-TEGO and $TiO_2$-LSGO, were then tested to evaluate their performance in energy storage devices, Li-ion batteries and micro-supercapacitors, respectively. The electrochemical performance was evaluated by cyclic voltammetry and galvanostatic charge-discharge measurements.

### 4.6.1 Electrochemical characterization of $TiO_2$-TEGO Li-ion half-batteries

The enhancement in the performance due to the presence of graphene (TEGO) compared to the pristine $TiO_2$ based electrode was evaluated in Li-ion half-cells.

#### 4.6.1.1 Galvanostatic charge-discharge measurements

Galvanostatic charge-discharge measurements (GCD) were performed at room temperature on the half-cells, with a Landt CT2001A battery testing system by means of charge and discharge cycles at a fixed current level. The half-cells were cycled between 2.5 V and 1 V (vs $Li/Li^+$), at each charge/discharge cycle. Ten charge/discharge cycles were tested at each current rate (*C-rate*). In order to normalize the specific capacity of the half-cell, C-rate were calculated considering that at the 1C rate the discharge current will discharge the half-cell up to 1 V in 1 hour. A rest time of 30 minutes was set between each charge and discharge process to reach the voltage stability.

The specific capacity of the half-cell was obtained from the active material masses, consisting of $TiO_2$-TEGO content and compared with those achieved by pristine $TiO_2$-HT based electrode.

### 4.6.2 Electrochemical characterization of $TiO_2$-LSGO micro-supercapacitors

The electrochemical performance of the $TiO_2$-LSGO micro-supercapacitors (MSCs) was investigated by cyclic voltammetry (CV) and galvanostatic charge-discharge measurements (GCD), in air at room temperature. The enhancement in the performance due to the pseudocapacitive effects induced by $TiO_2$ were evaluated and compared to the results obtained with LSGO MSCs.

### 4.6.2.1 Cyclic voltammetry

Cyclic voltammetry tests were performed with a Keithley Series 2400 Sourcemeter in a two electrodes configuration. A linearly changed electric potential was applied with 1, 5, 10 and 50 mV/s scan rates and the output current was recorded. Since the electrolyte was prepared in an aqueous solution, the operating voltage range was set between 0 and 0.8 V to avoid electrolysis of water at the decomposition potential of 1.23 V at room temperature.

### 4.6.2.2 Galvanostatic charge-discharge measurements

Galvanostatic charge-discharge measurements (GCD) were performed with the same testing system used for Li ion half-cells, as described in section 4.6.1.1. The MSCs were cycled between 0 V and 0.8 V at each charge/discharge cycle. Ten charge/discharge cycles were tested at each current rate. The key performance features of supercapacitors involve specific capacitance (gravimetric capacitance), specific energy (energy density), specific power (power density), capacity retention and cycling stability [15].

To obtain comparable data among different samples, it is useful to provide a specific (gravimetric) capacitance rather than total capacitance. The specific capacitance of a single electrode $C_{SP}$ (F/g) was obtained from the total capacitance $C$ of the micro-supercapacitor:

$$C_{SP} = 4\frac{C}{m_{AM}} \qquad (4.5)$$

where $m_{AM}$ is the total mass of the active material. The specific energy $E$ (Wh/kg) of the MSC was calculated by:

$$E = \frac{CU_{max}^2}{2m_{AM}3600} \qquad (4.6)$$

where $U_{max}$ (V) is the maximum region of electrochemical stability. The maximum specific power $P$ (W/kg) was given by:

$$P = \frac{U_{max}^2}{4\,ESR\,m_{AM}} \qquad (4.7)$$

where *ESR* (Ω) is the equivalent series resistance of the MSC [16].

The experimental specific power was calculated as specific energy *E* per unit time *t*, by:

$$P = \frac{E}{t} \qquad (4.8)$$

For each cycle, the Coulombic efficiency $\eta$ was given by:

$$\eta = \frac{C_d}{C_c} \qquad (4.9)$$

where $C_d$ and $C_c$ are the discharge and charge capacity, respectively.

The capacity retention was evaluated over at least 3000 cycles as the ratio of the specific capacity at each cycle to the specific capacity achieved in the first one (expressed in %).

## References


[1] M. Gaboardi, R. Tatti, G. Bertoni, G. Magnani, R. Della Pergola, L. Aversa, R. Verucchi, D. Pontiroli, M. Riccò, Platinum carbonyl clusters decomposition on defective graphene surface, Surf. Sci. 691 (2020) 121499. https://doi.org/10.1016/j.susc.2019.121499.

[2] M. Gaboardi, A. Bliersbach, G. Bertoni, M. Aramini, G. Vlahopoulou, D. Pontiroli, P. Mauron, G. Magnani, G. Salviati, A. Züttel, M. Riccò, Decoration of graphene with nickel nanoparticles: Study of the interaction with hydrogen, J. Mater. Chem. A. 2 (2014) 1039–1046. https://doi.org/10.1039/c3ta14127f.

[3] M.J. McAllister, J.L. Li, D.H. Adamson, H.C. Schniepp, A.A. Abdala, J. Liu, M. Herrera-Alonso, D.L. Milius, R. Car, R.K. Prud'homme, I.A. Aksay, Single sheet functionalized graphene by oxidation and thermal expansion of graphite, Chem. Mater. 19 (2007) 4396–4404. https://doi.org/10.1021/cm0630800.

[4] B.C. Brodie, On the Atomic Weight of Graphite, Philos. Trans. R. Soc. London. 149 (1859) 249–259. https://doi.org/10.1098/rstl.1859.0013.

[5] M. Riccò, D. Pontiroli, M. Mazzani, M. Choucair, J.A. Stride, O. V. Yazyev, Muons probe strong hydrogen interactions with defective graphene, Nano Lett. 11 (2011) 4919–4922. https://doi.org/10.1021/nl202866q.

[6] H.C. Schniepp, J.L. Li, M.J. McAllister, H. Sai, M. Herrera-Alonson, D.H. Adamson, R.K. Prud'homme, R. Car, D.A. Seville, I.A. Aksay, Functionalized single graphene sheets derived from splitting graphite oxide, J. Phys. Chem. B. 110 (2006) 8535–8539. https://doi.org/10.1021/jp060936f.

[7] C. Cavallari, D. Pontiroli, M. Jiménez-Ruiz, M. Johnson, M. Aramini, M. Gaboardi, S.F. Parker, M. Riccó, S. Rols, Hydrogen motions in defective graphene: The role of surface defects, Phys. Chem. Chem. Phys. 18 (2016) 24820–24824. https://doi.org/10.1039/c6cp04727k.

[8] H. Tian, J. Ma, K. Li, J. Li, Hydrothermal synthesis of S-doped TiO2 nanoparticles and their photocatalytic ability for degradation of methyl orange, Ceram. Int. 35 (2009) 1289–1292. https://doi.org/10.1016/j.ceramint.2008.05.003.

[9] D. Pontiroli, S. Scaravonati, M. Sidoli, G. Magnani, L. Fornasini, C. Milanese, M. Riccò, Fullerene mixtures as negative electrodes in innovative Na-ion batteries, Chem. Phys. Lett. 731 (2019) 136607. https://doi.org/10.1016/j.cplett.2019.136607.

[10] M.F. El-Kady, R.B. Kaner, Scalable fabrication of high-power graphene micro-supercapacitors for flexible and on-chip energy storage, Nat. Commun. 4 (2013) 1475–1479. https://doi.org/10.1038/ncomms2446.

[11] G.A. Waychunas, Structure, aggregation and characterization of nanoparticles, Rev. Mineral. Geochemistry. 44 (2001) 104–166. https://doi.org/10.2138/rmg.2001.44.04.

[12] V. Uvarov, I. Popov, Metrological characterization of X-ray diffraction methods at different acquisition geometries for determination of crystallite size in nano-scale materials, Mater. Charact. 85 (2013) 111–123. https://doi.org/10.1016/j.matchar.2013.09.002.

[13] D. Bersani, P.P. Lottici, X.Z. Ding, Phonon confinement effects in the Raman scattering by TiO2 nanocrystals, Appl. Phys. Lett. 72 (1998) 73–75.

https://doi.org/10.1063/1.120648.
[14] Y. Singh, Electrical Resistivity Measurements: a Review, Int. J. Mod. Phys. Conf. Ser. 22 (2013) 745–756. https://doi.org/10.1142/s2010194513010970.
[15] M.D. Stoller, R.S. Ruoff, Best practice methods for determining an electrode material's performance for ultracapacitors, Energy Environ. Sci. 3 (2010) 1294–1301. https://doi.org/10.1039/c0ee00074d.
[16] F. Béguin, V. Presser, A. Balducci, E. Frackowiak, Carbons and electrolytes for advanced supercapacitors, Adv. Mater. 26 (2014) 2219–2251. https://doi.org/10.1002/adma.201304137.

*This page intentionally left blank*

# 5 $TiO_2$-TEGO nanostructured materials for Li-ion batteries

The micro-structure of the synthesized $TiO_2$-TEGO materials was investigated to reveal the crystalline polymorphic phase of $TiO_2$ nanoparticles on TEGO sheets and to examine their morphometry. The graphene is henceforth called TEGO, as Thermally Exfoliated Graphite Oxide. The investigation was carried out for the characterization of the materials synthesized through the hydrothermal synthesis and those obtained by means of the high-energy ball milling treatment.

$TiO_2$ nanostructures on the TEGO layers are achieved following both the approaches. The investigation of the $TiO_2$-TEGO materials has been carried out both on pristine $TiO_2$, on pristine TEGO and on the composite materials based on $TiO_2$-TEGO.

## 5.1 TEGO graphene

The synthesis of TEGO has been carried out to produce graphene from the thermal exfoliation process. In figure 5.1, the powder X-ray diffraction (PXRD) patterns of graphite, graphite oxide and graphene are shown. The PXRD of the graphite, used as starting material, can be indexed by graphite peaks (PDF 001-0646). The graphite oxide (GO), obtained from the oxidation by the Brodie method, demonstrates the expansion of graphite planes by the (002) reflection at $2\theta=14.4°$, which corresponds to an increase of the interplanar distance to 0.615 nm, compared to the 0.335 nm of pristine graphite (corresponding to the reflection at 26.6° for graphite). The increased spacing is ascribed to the introduction of functional groups on the graphite planes during the oxidation process. Oxygen-containing groups, such as epoxy and hydroxyl groups, are expected to attach on the basal plane in GO, while carboxyl groups have been generally found on the edges, as proposed by Lerf et al. [1] (figure 5.2). After the thermal exfoliation of graphite oxide, the main reflections of graphite oxide are no longer observed, suggesting that oxygen-

containing groups have been removed during the exfoliation. A broad band appears at 2θ~25°, as indicative feature of a loss of long-range order in TEGO [2].

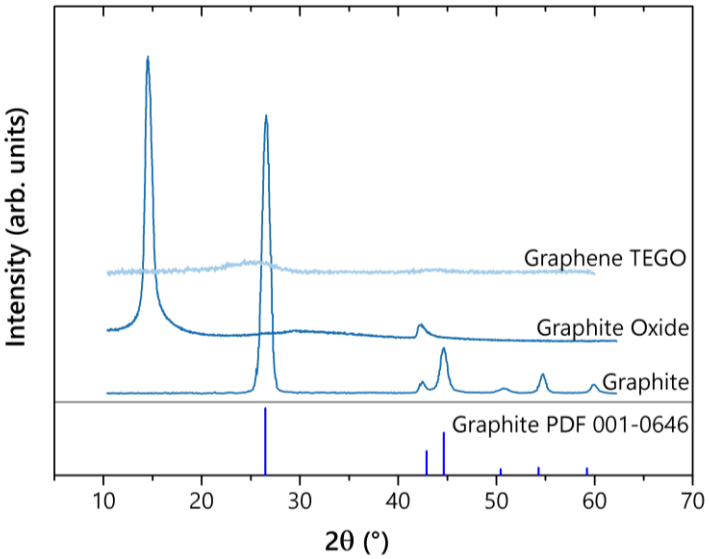


*Figure 5.1 PXRD patterns of graphite, graphite oxide from Brodie method and TEGO graphene after thermal exfoliation. The reference pattern of graphite (PDF 001-0646) is shown.*

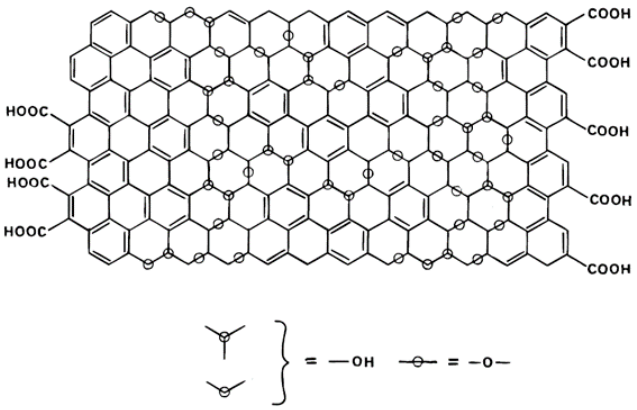


*Figure 5.2 Schematic representation of the structural model of graphite oxide and oxygen-containing functional groups* [1].

## 5.2 Pristine hydrothermally $TiO_2$

The as-prepared pristine $TiO_2$ was obtained through the hydrothermal synthesis. Pristine hydrothermally $TiO_2$ is henceforth called $TiO_2$-HT. It was synthesized to be used as reference material in electrode, in order to compare the electrochemical performance of $TiO_2$-TEGO materials and pristine $TiO_2$.

$TiO_2$-HT consists of $TiO_2$ crystalline nanoparticles, mainly in anatase phase, with a minor brookite phase content. The peaks of the PXRD pattern can be indexed by anatase (PDF 00-021-1272) and brookite (PDF 00-029-1360) phases, as shown in figure 5.3.

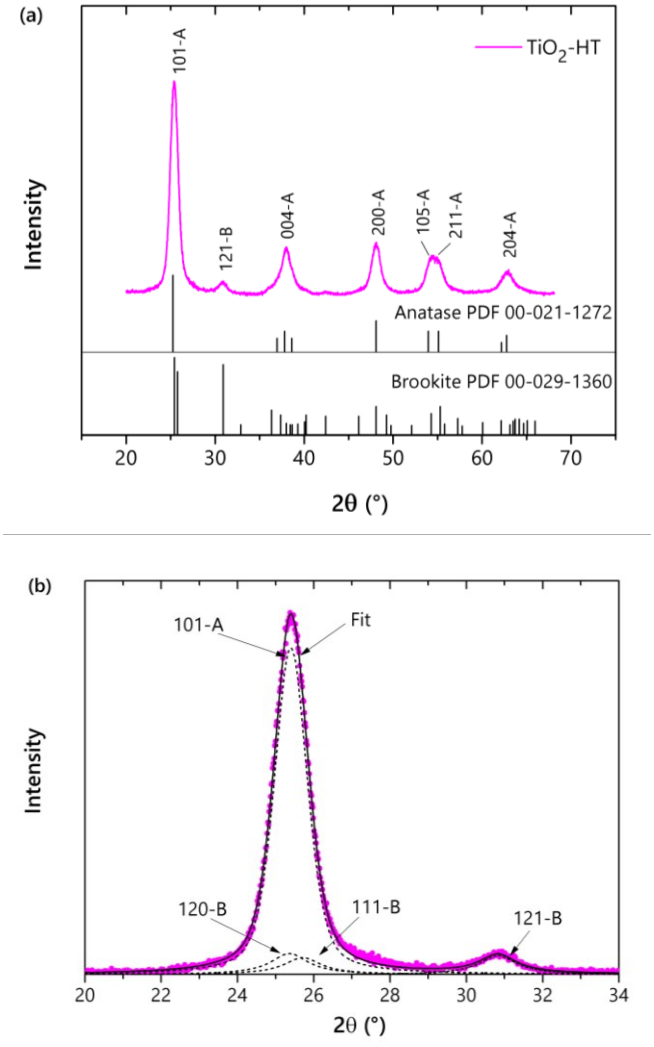


*Figure 5.3 (a) PXRD pattern of pristine hydrothermally synthesized $TiO_2$ with anatase (PDF 00-021-1272) and brookite (PDF 00-029-1360) references. The crystallographic planes of the two $TiO_2$ polymorphs are shown: (A) anatase, (B) brookite. (b) Deconvolution of the anatase (101) and brookite (120), (111), (121) crystallographic planes.*

The crystallite size of anatase was calculated from the (101) major reflection by the Scherrer equation, as reported in section 4.5.1. The estimation of the average dimension of crystallite size gives a value of 7.9 ± 0.6 nm. The uncertainty in the average dimension, obtained from the propagation of errors, is mainly influenced by the uncertainty in the peak width, which depends on the instrumental broadening. However, a contribution to the broadening from the dispersion of the crystallite size cannot be excluded. If the material was polydisperse, namely consisting of a heterogeneous particle size distribution, a bigger uncertainty in the crystallite dimension should be considered, far more affected by the non-uniformity of the size distribution than by the instrumental peak broadening.

It is worth noting that, in the crystallite size estimation, the (101) anatase reflection at 2θ=25.28° is overlapping the (120) and (111) brookite peaks at 2θ=25.34° and 2θ=25.69°, respectively. Thus, the brookite contribution was considered in the estimation, fitting with Pseudo-Voigt curves the (101) anatase peak and the (120), (111) and (121) brookite reflections. It was assumed that the three brookite contributions have the same peak broadening and their intensities were fixed at 100/80/90, according to their values in the PDF 00-029-1360, respectively [3]. Figure 5.3b shows the deconvolution of the anatase and brookite crystallographic planes.

In the quantitative phase analysis (QPA) using the Rietveld method, the anatase and the brookite phase fractions have been determined at 0.77 and 0.23, respectively. The weight fractions of the $TiO_2$ polymorphs were confirmed by the method of Zhang and Banfield, within a few percent [3]. The method estimates the weight fractions of anatase ($W_A$) and brookite ($W_B$) through the following relations:

$$W_A = \frac{k_A A_A}{k_A A_A + k_B A_B} \qquad (5.1)$$

$$W_B = \frac{k_B A_B}{k_A A_A + k_B A_B} \qquad (5.2)$$

where $A_A$ and $A_B$ are the integrated intensity of the anatase (101) and the brookite (121) peaks, respectively. The coefficients $k_A$ and $k_B$ have been optimized at 0.886 and 2.721 by the method, respectively. In $TiO_2$-HT, the $TiO_2$ polymorphs weight fraction results in 0.80 for anatase and 0.20 for brookite.

The coexistence of anatase and brookite $TiO_2$ polymorphs was proved by Raman spectroscopy, as shown in figure 5.4. The five Raman peaks of the anatase structure were found at ~148, 201, 400, 518 and 640 $cm^{-1}$, corresponding to the $E_g$, $E_g$, $B_{1g}$, $A_{1g}(B_{1g})$ and $E_g$ Raman modes, respectively [4]. Some of the main features of the brookite phase were also detected at 249, 327, 363 $cm^{-1}$, attributed to $A_{1g}$, $B_{1g}$ and $B_{2g}$ Raman modes, respectively [5].

The main $E_g$ anatase peak in $TiO_2$-HT is shifted and broadened compared to the crystalline anatase, as highlighted in the inset of figure 5.4. Specifically, it is observed at 148.0 ± 0.5 $cm^{-1}$ with a linewidth (FWHM) of 16.9 ± 0.5 $cm^{-1}$ in $TiO_2$-HT and at 142.9 ± 0.6 $cm^{-1}$ with a FWHM of 9.3 ± 0.5 $cm^{-1}$ in crystalline anatase.

It is well established that the main anatase Raman peak at 143 $cm^{-1}$ undergoes a broadening and a shift towards higher wavenumbers as the size of nanocrystal decreases, when pressure or disorder (e.g. non-stoichiometry) effects are not occurring [4,6]. The phonon confinement model describes the shape parameters of the main anatase vibrational mode, in terms of shift and broadening of the Raman peak, as nanocrystal size decreases. The values of peak position and FWHM found for $TiO_2$-HT are in accordance with the model, confirming the nano-crystallinity of the material.

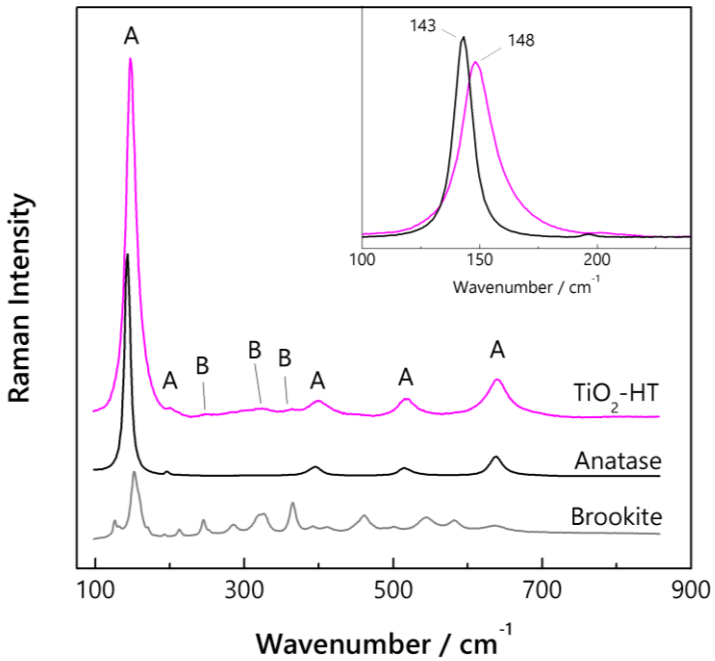


*Figure 5.4 Raman spectra of pristine hydrothermally synthesized $TiO_2$-HT (purple) with anatase (A) and brookite (B) features; crystalline anatase (black) and brookite (gray) reference spectra. In the inset: comparison of the $E_g$ vibrational mode of anatase at 143 $cm^{-1}$ between $TiO_2$-HT and crystalline anatase. Raman spectra were acquired with the excitation laser at 632.8 nm.*

## 5.3 $TiO_2$-TEGO nanostructures

The $TiO_2$-TEGO materials obtained by the hydrothermal synthesis and the high-energy ball milling treatment are discussed and compared here. Two different contents of $TiO_2$ and TEGO were achieved through the hydrothermal method, namely in the $TiO_2$:TEGO ratio of (99:1) and (80:20) wt%, respectively. The $TiO_2$-TEGO material from the ball milling process was compared to the hydrothermally synthesized in the same $TiO_2$:TEGO ratio of (80:20) wt%. The materials were then used to produce the electrodes for Li-ion batteries and their electrochemical performance will be shown in the next chapter.

### 5.3.1 $TiO_2$-TEGO hydrothermally synthesized materials

The $TiO_2$-TEGO nanostructured materials synthesized by the hydrothermal reaction consist of $TiO_2$ nanoparticles (NPs) decorating graphene (TEGO) sheets, in both the two $TiO_2$:TEGO preparations, consisting of 99% $TiO_2$ NPs on 1% TEGO and 80% $TiO_2$ NPs on 20% TEGO, respectively.

In the hydrothermal synthesis, graphene was successfully used as a support for the growth of crystalline $TiO_2$ NPs. The procedure is effective in promoting a wide spread of nanoparticles over TEGO layers, as shown from the HRTEM observations in figure 5.5. The graphene film consists of wrinkly layers, occurring in the entire material. Folded layers are clearly observable from the wrinkles in figure 5.5a and in the upper-right part of figure 5.5b, as indicated by the red arrows. The morphology of TEGO in $TiO_2$-TEGO shows good agreement with the results on pristine TEGO, which is made of flat single layer domains and thicker parts resulting from residual defective graphite oxide with a number of layers ≤5 [7].

The morphology of nanostructured $TiO_2$ resumes the typical shape of anatase crystals, being mostly truncated bipyramid-shaped and consisting of anatase phase, as confirmed by the (101) planes with interplanar spacing of 0.35 nm. In some cases, the octahedral morphology changes in a quasi-spherical shape for anatase nanoparticles with an average diameter of 8 nm or into rod-like particles. The pyramidal nanoparticles show a slight bigger dimension, with an average size of 11 x 8 $nm^2$ (figure 5.5b).

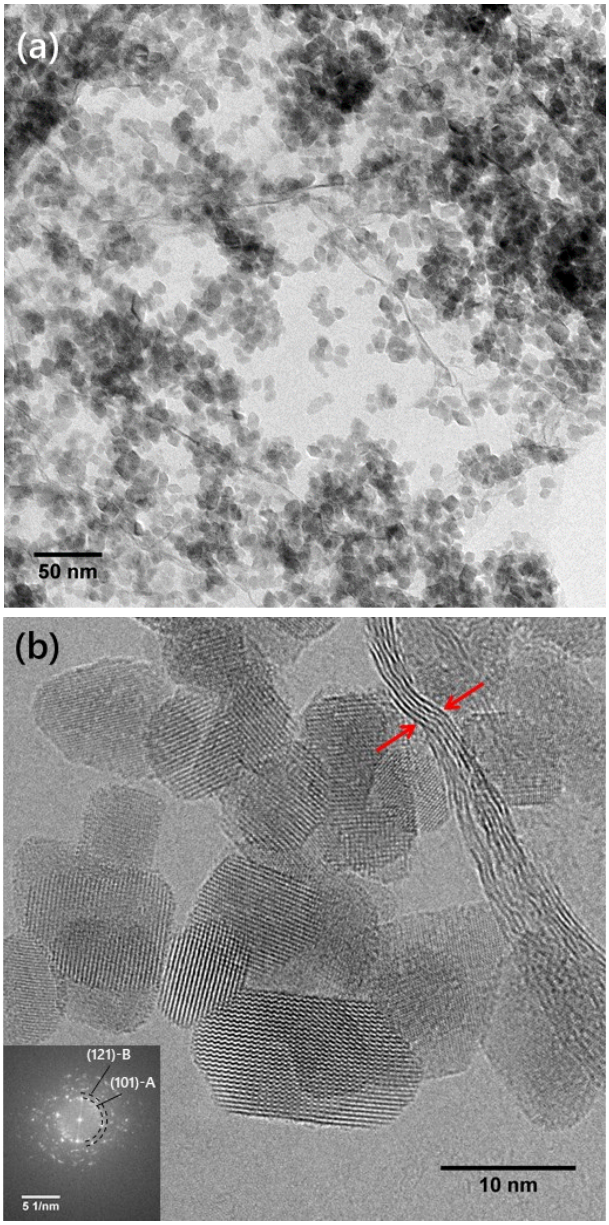


*Figure 5.5 HRTEM images of $TiO_2$-TEGO (99:1) wt%: (a) at low and (b) high magnification. The inset image in (b) shows the FFT. Few folded TEGO layers are highlighted by the arrows.*

Titanium dioxide NPs in $TiO_2$-TEGO (99:1) and (80:20) wt% mainly consists of anatase phase and a small brookite contribution. The crystallographic structure of both the two hydrothermally synthesized samples resumes that of $TiO_2$-HT, as shown in the powder X-ray diffraction pattern (figure 5.6). Specifically, the contribution of brookite appears less intense than in the pristine $TiO_2$ sample. The weight fractions of the two polymorphs were estimated with the already mentioned method by Zhang and Banfield [3], as for $TiO_2$-HT. In the two preparations, the different ratio of $TiO_2$/graphene does not influence the

anatase/brookite content ratio. For both the (99:1) and the (80:20) wt% contents, the weight fraction of anatase is 0.94, whereas the brookite amounts only at 0.06. The estimation of the average crystallite sizes, obtained as previously described, gives 8.0 ± 0.6 nm and 7 ± 0.5 nm for the (99:1) and the (80:20) materials, respectively. Given that $TiO_2$ NPs do not show a homogeneous particle size distribution, a higher uncertainty on the crystallite size dimension should be considered, amounting to ~30% in terms of relative error.

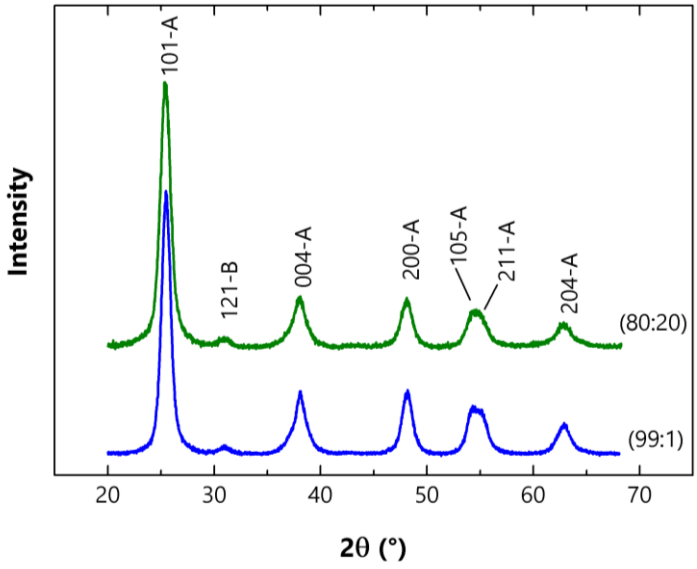


*Figure 5.6 PXRD patterns of hydrothermally synthesized $TiO_2$-TEGO nanostructures with (99:1) and (80:20) wt% contents.*

The nano-crystallinity of $TiO_2$-TEGO (99:1) was confirmed by the Raman spectrum, shown in figure 5.7. The anatase main peaks have been found at ~148, 200, 395, 517 and 640 $cm^{-1}$, whereas the brookite features are hardly visible. As well as observed in the $TiO_2$-HT material, the Raman shift and broadening of the $E_g$ anatase peak are highlighted (inset of figure 5.7). Specifically, the $E_g$ peak has been observed at 148.4 ± 0.7 $cm^{-1}$ with a linewidth (FWHM) of 17.7 ± 0.8 $cm^{-1}$. In the uncertainty in peak position and in linewidth, both the standard deviations of the data and half of the spectral resolution have been taken into consideration, since the contributions are comparable. The values of peak position and FWHM found for $TiO_2$-TEGO (99:1) are in line with those expected by the phonon confinement model [4].

In the high wavenumber region of the spectrum, graphene signals are detected with the characteristic so-called D and G bands, at 1362 $cm^{-1}$ and 1602 $cm^{-1}$, respectively (figure 5.8). It is well known that the G band (G stands for "graphite") is indicative of the in-plane vibration of $sp^2$ carbon hexagonal network with $E_{2g}$ symmetry [8,9]. In case of disordered carbonaceous material, the D band (D stands for "disorder" or "defects") appears, as $A_{1g}$ vibration mode, in addition to the G band. The D band arises from disorder effects or defects in the imperfect crystalline structure, such as carbon vacancy, $sp^3$ carbon content, edges, stacking faults [10]. As expected from graphene obtained by thermal exfoliation, the defective feature of TEGO is fully confirmed by the broad D band, which accounts the contribution of amorphous carbon and structural defects [7].

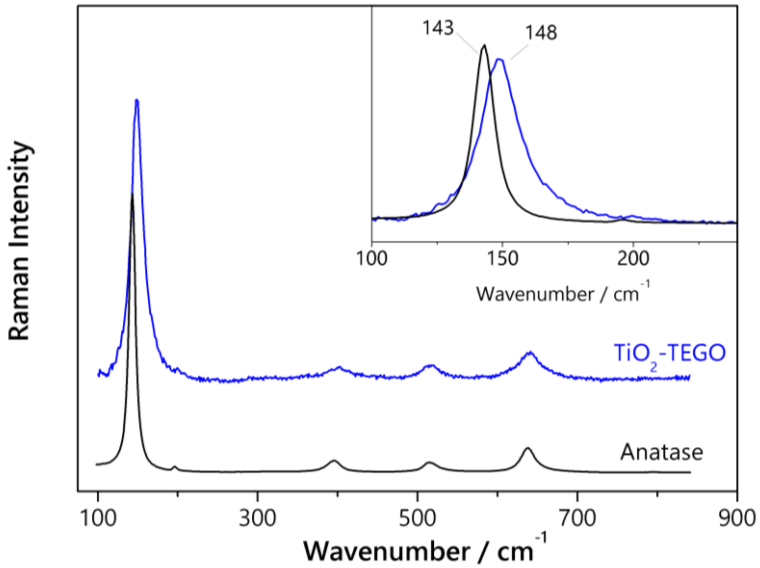


*Figure 5.7 Raman spectra of $TiO_2$-TEGO (99:1) wt% (blue) and crystalline anatase reference spectrum (black). In the inset: comparison of the $E_g$ vibrational mode of anatase at 143 $cm^{-1}$ between $TiO_2$-TEGO (99:1) and crystalline anatase. Raman spectra were acquired with the excitation laser at 632.8 nm.*

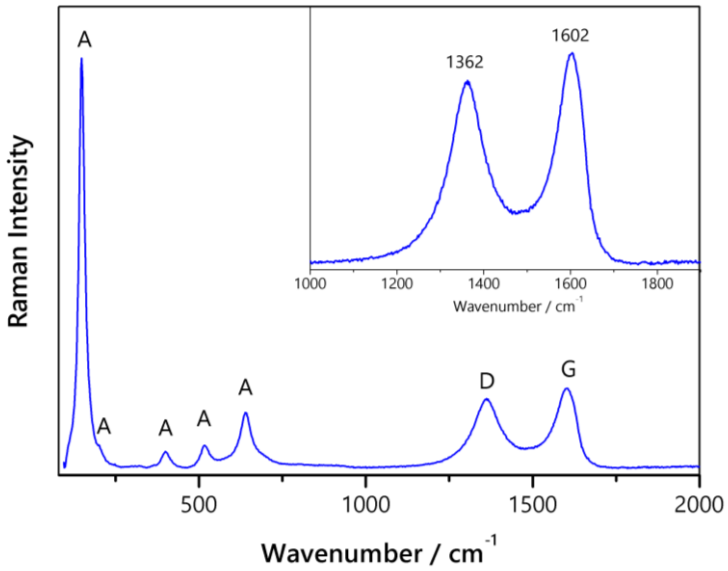


*Figure 5.8 Raman spectrum of $TiO_2$-TEGO (99:1) with anatase and graphene features. In the inset: D and G graphene characteristic bands. Raman spectrum was acquired with the excitation laser at 473.1 nm.*

### 5.3.2 $TiO_2$-TEGO high-energy ball milling treated materials

The ball milled material was obtained starting from TEGO and commercial $TiO_2$ P25 nanoparticles. The material, henceforth called *$TiO_2$-TEGO-BM*, consists of anatase and rutile $TiO_2$ nanoparticles supported onto the graphene layers.

As expected from P25, which is made of crystalline anatase and rutile nanoparticles, both the two $TiO_2$ polymorphs were easily detected by the X-ray diffraction analysis. In PXRD, the anatase and rutile contribution can be indexed by anatase (PDF 00-021-1272) and rutile (PDF 00-01-1292) phases, respectively (figure 5.9). In addition, in the diffraction pattern a small amount of the high-pressure polymorph $TiO_2$ II can be observed, with the most intense reflection at 2θ~31.5°, corresponding to the (101) $TiO_2$ II planes [11]. The $TiO_2$ II formation can be ascribed to the locally high pressure reached in the collisions during the high-energy ball milling treatment. It is known that $TiO_2$ II is formed from anatase at pressure higher than 2.56 GPa [12].

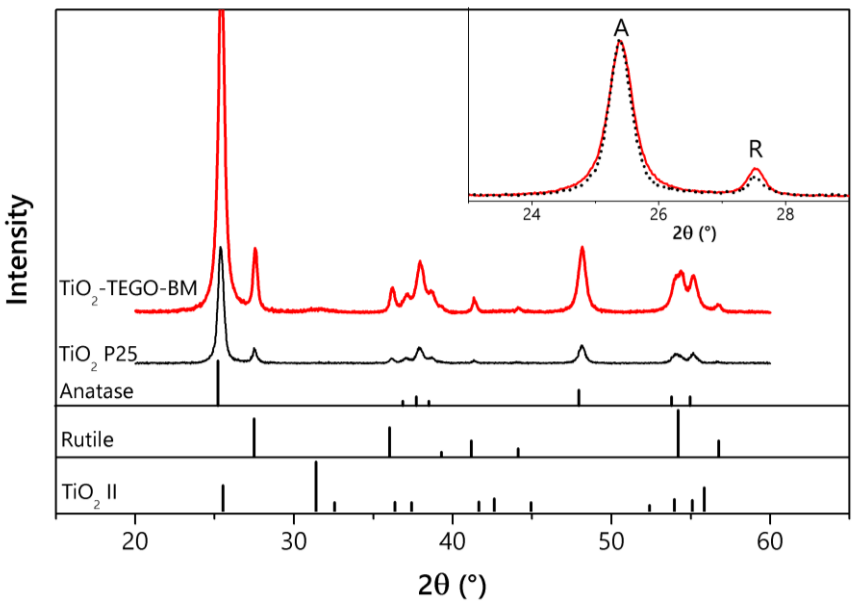


*Figure 5.9 PXRD pattern of $TiO_2$-TEGO-BM (red) with reference patterns (black): $TiO_2$ P25, anatase (PDF 00-021-1272), rutile (PDF 00-01-1292) and $TiO_2$ II reference from* [11]. *In the inset: the main (101) anatase (A) and (110) rutile (R) peaks of $TiO_2$-TEGO-BM (red) and $TiO_2$ P25 (black dots).*

The diffraction pattern shows a slight broadening of the peaks in the $TiO_2$-TEGO-BM material, compared to the pristine $TiO_2$ P25 profile, as expected after the ball milling treatment. The broadening can be observed in the inset of figure 5.9, from the comparison of the main (101) anatase and (110) rutile reflections. An 8-10% broadening of PXRD peaks can be explained by the disorder effects introduced during the high-energy treatment.

This effect can be observed on the morphology in a thin amorphous-like shell around the crystalline NPs, resulting from the grinding, as highlighted in the HRTEM images in figure 5.10. From inside out, a loss of NPs crystallinity has been detected from the loss of periodicity of the interplanar spacing in HRTEM images. However, it cannot be excluded that the outermost layer (few tenths of a nanometre) is made of amorphous carbon.

The shape of the NPs includes elongated and truncated bipyramidal nanoparticles, whose dimensions are close to those obtained from PXRD, in the range of 20-30 nm or even slightly larger for few nanoparticles of 40-50 nm, as shown in figure 5.10a.

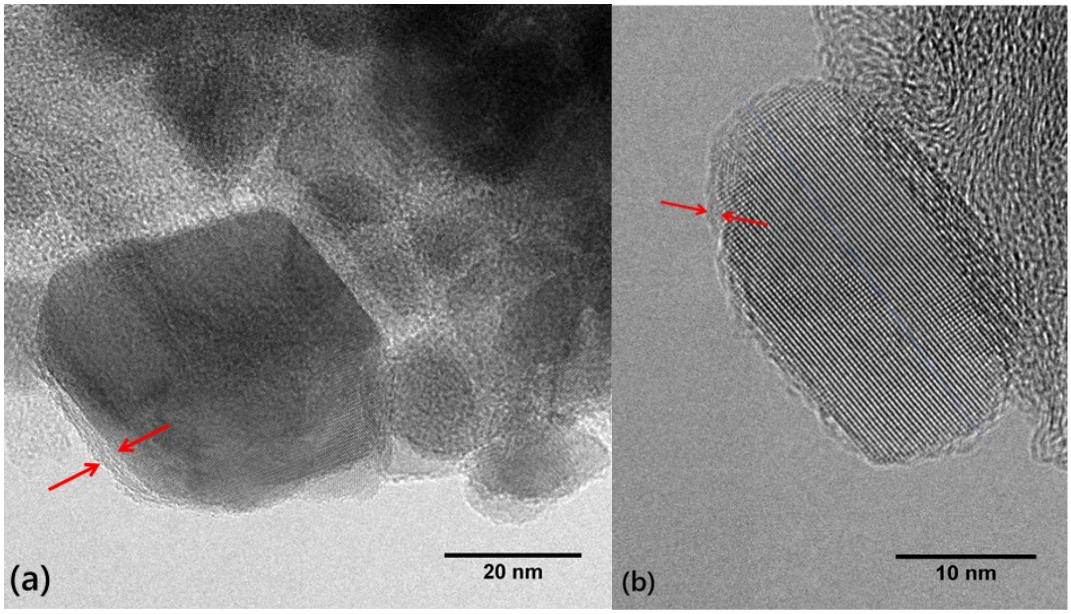


*Figure 5.10 (a) and (b) HRTEM images on $TiO_2$-TEGO-BM showing amorphous-like shell around the nanoparticles (highlighted by arrows).*

The disorder induced by ball milling on the NPs, as observed from HRTEM images, is further confirmed by the band shape parameters of the anatase Raman peaks. Unlike previously observed for the hydrothermally synthesized $TiO_2$ NPs, here the shift and the broadening of the most intense $E_g$ anatase peak are ascribed to the structural disorder rather than to particle size effects, due to the nature of the high-energy ball milling treatment.

Both the peak position and the linewidth of 143 $cm^{-1}$ anatase peak appear shifted and broadened asymmetrically towards higher wavenumber, compared to the pristine $TiO_2$ P25 (figure 5.11). The peak position occurs at 151.3 ± 1.7 $cm^{-1}$ with a full width at half maximum of 20.3 ± 2.1 $cm^{-1}$, whereas in P25 the same anatase peak is found at 143.9 ± 0.5 $cm^{-1}$ with a full width at half maximum of 10.6 ± 0.5 $cm^{-1}$. In commercial $TiO_2$ P25, the uncertainty in the peak position and in the linewidth are considered as half of the spectral resolution. Conversely, for the ball milled material, both the spectral resolution and the standard deviation of the data have been considered and added *in quadrature*, since the dispersion of values is not negligible.

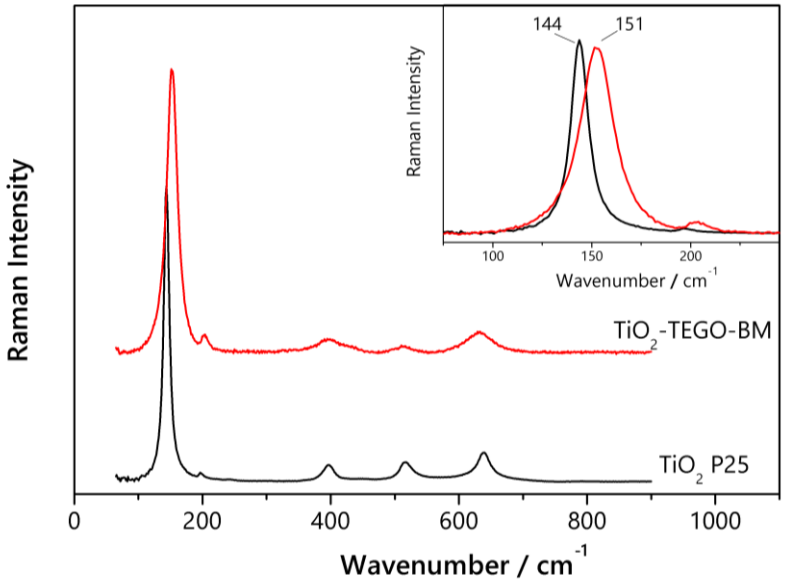


*Figure 5.11 Raman spectra of $TiO_2$-TEGO-BM (red) and pristine $TiO_2$ P25 (black). In the inset: zoom on the main anatase $E_g$ peak. Raman spectra were acquired with the excitation laser at 632.8 nm.*

It is well-known that defects within the material can strongly influence the shifting and the broadening of some Raman peaks. The oxygen stoichiometry of a transition metal oxide material, being here titanium dioxide, is a possible source for those changes in the Raman spectra. Specifically, it was observed that the strongest anatase $E_g$ vibrational mode at 143 $cm^{-1}$ broadens and shifts towards higher wavenumbers, as the O/Ti ratio decreases, due to oxygen deficiency. The variation of the band shape and position found by Parker and Siegel is reported in figure 5.12 [13,14].

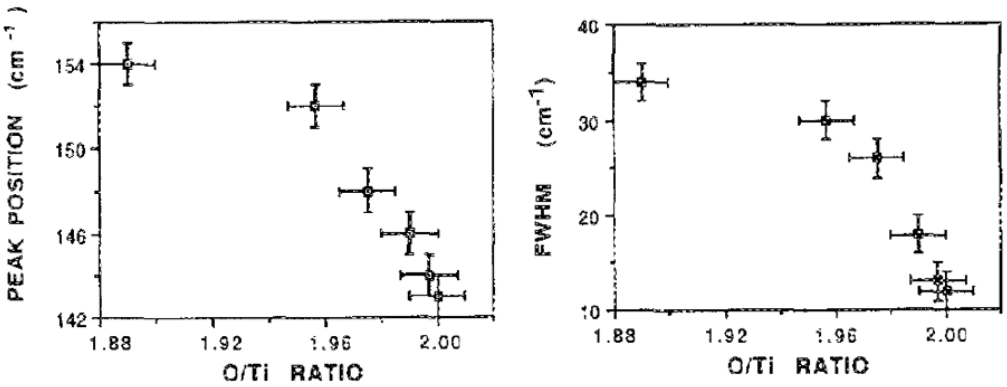


*Figure 5.12 Correlation of the O/Ti ratio with the peak position of the strongest anatase $E_g$ vibrational mode and its full width at half maximum (FWHM)* [13].

A confirmation of the non-stoichiometric $TiO_2$ is given by the chemical composition performed by STEM-EDX (figure 5.13b) in the region shown in figure 5.13a, on the $TiO_2$-TEGO-BM sample. In terms of atom percentage, the $TiO_2$-TEGO-BM material is made up of 40% oxygen, 22% titanium and the remaining 38% carbon, constituted by the TEGO sheets. As a result, the O/Ti ratio gives the value of 1.8, suggesting the oxygen deficiency in $TiO_2$ after the ball milling process.

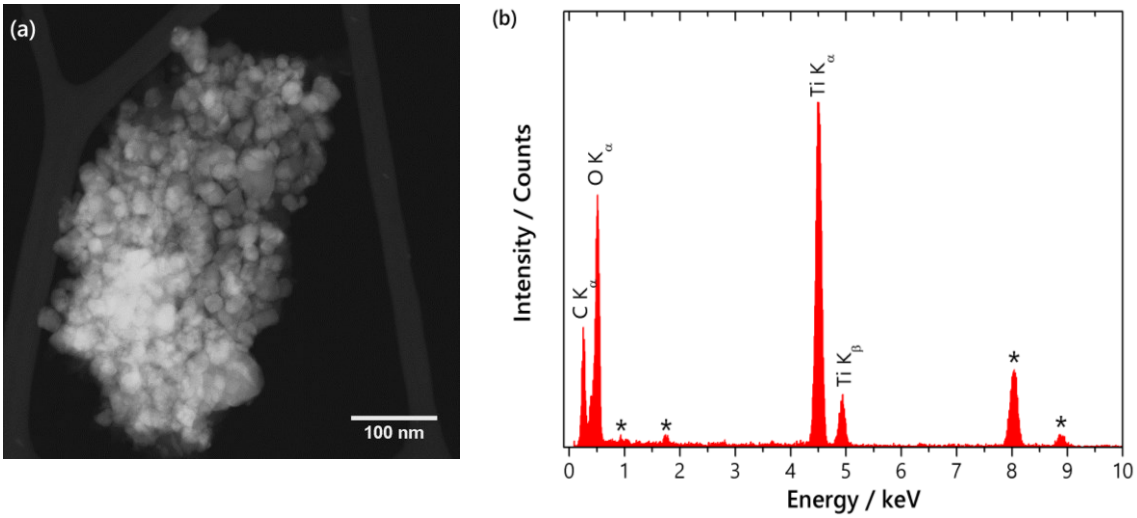


*Figure 5.13 (a) STEM image of $TiO_2$-TEGO-BM and (b) EDX spectrum of the corresponding region in (a). The signals of the copper grid and from the detector are indicated by asterisks.*

### 5.3.3 $TiO_2$-TEGO materials: discussion

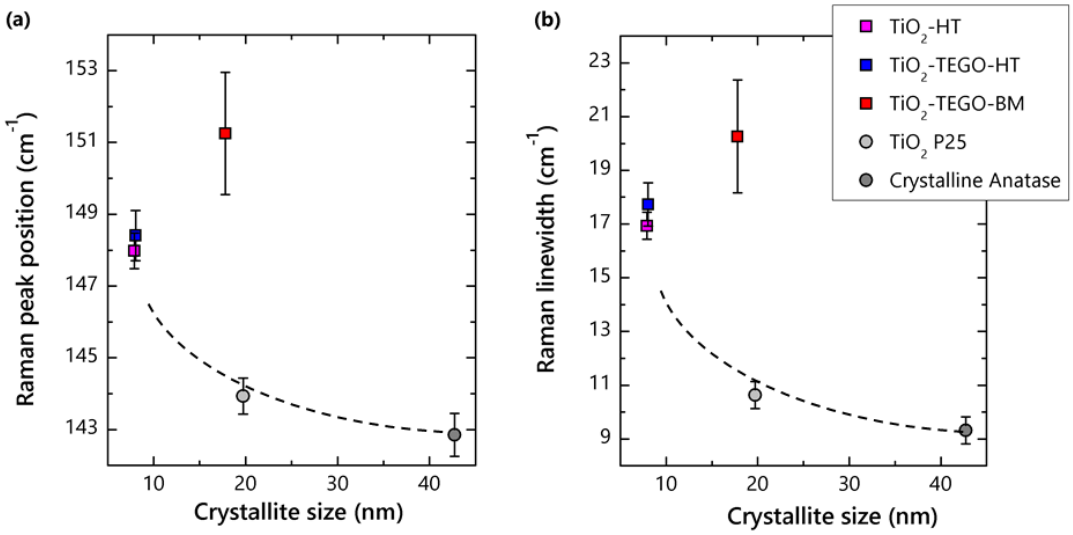


*Figure 5.14 Correlation between the Raman band shape of the 143 $cm^{-1}$ anatase peak and the crystallite size calculated from the (101) anatase reflection of the XPRD pattern among $TiO_2$-TEGO materials: (a) variation in the Raman peak position and (b) variation in the Raman linewidth. Dashed lines are visual lines to show the trend expected from the confinement model.*

The $TiO_2$-TEGO materials obtained by the two different approaches, namely the hydrothermal synthesis and the high-energy ball milling treatment, are compared here. In figure 5.14, the correlation between the crystallite domain size and the Raman band parameters is presented, in terms of Raman position and linewidth of the 143 $cm^{-1}$ $E_g$ anatase peak. Both the hydrothermally synthesized materials and the ball milled product show a shift towards higher wavenumbers and a broadening of the Raman peak, compared to corresponding crystalline anatase parameters (peak position at 142.9 ± 0.6 $cm^{-1}$ with a FWHM of 9.3 ± 0.5 $cm^{-1}$). Though, the two approaches result in a different variation of the parameters.

In the hydrothermally synthesized materials, the Raman band shape changes according to the phonon confinement model. As expected for decreasing crystal size, not only zone-centre optical phonons, but all the phonons of the Brillouin zone are involved in contributing in the Raman spectra. Thus, the phonon dispersion results in a shift and in an asymmetrical broadening of Raman peaks [4,6]. The shift towards higher wavenumbers is

explained by the positive dispersion curve of anatase, as obtained by Bersani et al. [4] and reported in figure 5.15.

In contrast, in the ball milled product, the Raman band shape is affected by a different contribution rather than by the nanocrystals dimension. The observations by TEM and the estimation of the crystallite size from the PXRD pattern are in good agreement in suggesting that the nanoparticles are not smaller than 20 nm. According to these dimensions, the phonon confinement should not predict a visible shift and broadening which have instead been experimentally observed.

It should be highlighted that the high-energy ball milling treatment introduces disorder effects and a deviation from stoichiometry of the material, as observed from the EDX quantification (figure 5.13b). These effects are the main responsible sources for the variation in the shape and position of the anatase peak. It has been proven that the oxygen deficiency in $TiO_2$ causes a shift toward higher wavenumbers and a broadening of the Raman peak [13,14].

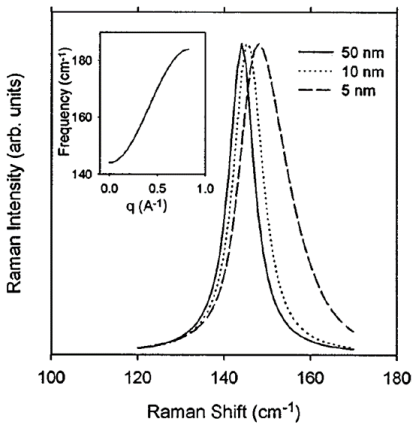


*Figure 5.15 Calculated 144 $cm^{-1}$ anatase Raman peak intensity by phonon confinement model for different nanometre-sized crystals. In the inset: the corresponding anatase dispersion curve from Bersani et al.[4].*

## References


[1] A. Lerf, H. He, M. Forster, J. Klinowski, Structure of Graphite Oxide Revisited, J. Phys. Chem. B. 102 (1998) 4477–4482. https://doi.org/10.1021/jp9731821.

[2] A. Kaniyoor, T.T. Baby, S. Ramaprabhu, Graphene synthesis via hydrogen induced low temperature exfoliation of graphite oxide, J. Mater. Chem. 20 (2010) 8467–8469. https://doi.org/10.1039/c0jm01876g.

[3] H. Zhang, J.F. Banfield, Understanding polymorphic phase transformation behavior during growth of nanocrystalline aggregates: Insights from TiO2, J. Phys. Chem. B. 104 (2000) 3481–3487. https://doi.org/10.1021/jp000499j.

[4] D. Bersani, P.P. Lottici, X.Z. Ding, Phonon confinement effects in the Raman scattering by TiO2 nanocrystals, Appl. Phys. Lett. 72 (1998) 73–75. https://doi.org/10.1063/1.120648.

[5] G.A. Tompsett, G.A. Bowmaker, R.P. Cooney, J.B. Metson, K.A. Rodgers, J.M. Seakins, The Raman spectrum of brookite, TiO2 (Pbca, Z = 8), J. Raman Spectrosc. 26 (1995) 57–62. https://doi.org/10.1002/jrs.1250260110.

[6] S. Kelly, F.H. Pollak, M. Tomkiewicz, Raman spectroscopy as a morphological probe for TiO2 aerogels, J. Phys. Chem. B. 101 (1997) 2730–2734. https://doi.org/10.1021/jp962747a.

[7] M. Gaboardi, A. Bliersbach, G. Bertoni, M. Aramini, G. Vlahopoulou, D. Pontiroli, P. Mauron, G. Magnani, G. Salviati, A. Züttel, M. Riccò, Decoration of graphene with nickel nanoparticles: Study of the interaction with hydrogen, J. Mater. Chem. A. 2 (2014) 1039–1046. https://doi.org/10.1039/c3ta14127f.

[8] F. Tuinstra, J.L. Koenig, Raman Spectrum of Graphite, J. Chem. Phys. 53 (1970) 1126–1130. https://doi.org/10.1063/1.1674108.

[9] M.A. Pimenta, G. Dresselhaus, M.S. Dresselhaus, L.G. Cançado, A. Jorio, R. Saito, Studying disorder in graphite-based systems by Raman spectroscopy, Phys. Chem. Chem. Phys. 9 (2007) 1276–1291. https://doi.org/10.1039/b613962k.

[10] A. Sadezky, H. Muckenhuber, H. Grothe, R. Niessner, U. Pöschl, Raman microspectroscopy of soot and related carbonaceous materials: Spectral analysis and structural information, Carbon N. Y. 43 (2005) 1731–1742. https://doi.org/10.1016/j.carbon.2005.02.018.

[11] P.Y. Simons, F. Dachille, The structure of TiO 2 II, a high-pressure phase of TiO 2, Acta Crystallogr. 23 (1967) 334–336. https://doi.org/10.1107/s0365110x67002713.

[12] T. Ohsaka, S. Yamaoka, O. Shimomura, Effect of hydrostatic pressure on the Raman spectrum of anatase (TiO2), Solid State Commun. 30 (1979) 345–347. https://doi.org/10.1016/0038-1098(79)90648-3.

[13] J.C. Parker, R.W. Siegel, Calibration of the Raman spectrum to the oxygen stoichiometry of nanophase TiO2, Appl. Phys. Lett. 57 (1990) 943–945. https://doi.org/10.1063/1.104274.

[14] J.C. Parker, R.W. Siegel, Raman Microprobe Study of Nanophase TiO2 and Oxidation-Induced Spectral Changes, J. Mater. Res. 5 (1990) 1246–1252. https://doi.org/10.1557/JMR.1990.1246.

*This page intentionally left blank*

# 6 Electrochemical performance of $TiO_2$-TEGO materials in Li-ion half-cells

The chapter will discuss the electrochemical performance of $TiO_2$-TEGO nanostructured materials in electrodes for Li-ion batteries.

The half-cells, assembled as described in section 4.2, were tested by galvanostatic charge-discharge cycles. The enhancement in the performance due to the presence of TEGO compared to the pristine $TiO_2$-based electrode will be investigated in hydrothermally synthesized $TiO_2$-TEGO materials. The two different relative contents of $TiO_2$:TEGO were compared, (99:1) and (80:20) wt%. Along with a chemical route, a solid-state approach was tested to obtain the electrode materials, referred as $TiO_2$-TEGO-BM. The effectiveness of this technique will be evaluated and compared to the results on hydrothermally synthesized materials.

## 6.1 Electrochemical performance of Li-ion half-cells

The lithium insertion/extraction properties in the electrodes based on $TiO_2$-TEGO materials were investigated to prove the effectiveness of graphene in improving the electrochemical performance and the rate capability compared to the pristine $TiO_2$-based electrode.

It is well-known that anatase $TiO_2$ lattice can accommodate $Li^+$ ions through insertion and extraction of positive ions. During charge process, lithium ions are inserted (process known as lithiation) into $TiO_2$ electrode, while an equal number of electrons are taken from the external circuit, in order to preserve the charge neutrality. Conversely, during discharging, lithium ions are extracted from the electrode (de-lithiation) and electrons are transferred into the external circuit to provide the current flow. The lithiation and the de-lithiation reactions of $TiO_2$ occur according to the:

$$TiO_2 + x\,Li^+ + x\,e^- \leftrightarrow Li_xTiO_2 \qquad (6.1)$$

$$0 \leq x \leq 1$$

where *x* is the Li mole fraction per $TiO_2$. $Ti^{4+}$ in anatase undergoes a progressively reduction as x value increases, reaching $Ti^{3+}$ when x=1, which gives a theoretical capacity of 335 mAh/g. However, in order that the reaction is completely reversible, the maximum obtained value is x=0.5, corresponding to a capacity of 168 mAh/g. At x=0.5, the insertion of lithium ions into the octahedral sites is responsible for a structural phase transition from tetragonal anatase $TiO_2$ to orthorhombic $Li_{0.5}TiO_2$ [1–4].

To improve the Li insertion capacity, graphene is a promising material to be combined with $TiO_2$. An enhanced electrical conductivity and a lowered aggregation of $TiO_2$ nanoparticles thanks to the presence of graphene would result in an improved storage charge in LIBs [5].

To this extent, the combination of the thermally exfoliated graphite oxide (TEGO) with the growth of $TiO_2$ nanoparticles, which was discussed in chapter 5, will be demonstrated to be effective in enhancing the electrochemical performance of $TiO_2$-based electrodes. In this chapter the electrochemical results of $TiO_2$-TEGO and $TiO_2$-TEGO-BM electrode materials will be discussed and compared to the results obtained with $TiO_2$-HT as active material.

### 6.1.1 Electrochemical results of $TiO_2$-TEGO electrodes

The electrochemical results on the half-cells are here described. Electrodes made up of $TiO_2$-TEGO (99:1) and $TiO_2$-TEGO (80:20) are discussed and compared to the results of $TiO_2$-HT. The devices underwent charge and discharge cycles between 1 V and 2.5 V (vs $Li/Li^+$) at a fixed current level (C-rate). Several C-rates have been tested to evaluate the rate capability also at high rate.

In order to reach the voltage stability, a rest time of 30 minutes was applied before each charge and discharge cycle. As an example, the voltage profile of charge-discharge cycles at a rate of C/2 for the $TiO_2$-TEGO (99:1) half-cell is shown in figure 6.1 and the rest time regions are highlighted. After charging, the cell voltage first jumps in an ohmic drop, then steadily reaches the equilibrium point. Conversely, after discharging, the voltage quickly rises and then gradually approaches the steady state.

This effect is ascribed to the concentration gradient between the electrolyte and the solid electrode which undergoes a relaxation effect with diffusion process, when the external current is interrupted. In addition, during the rest time, lithium is redistributed from the front to the back of the electrode [6].

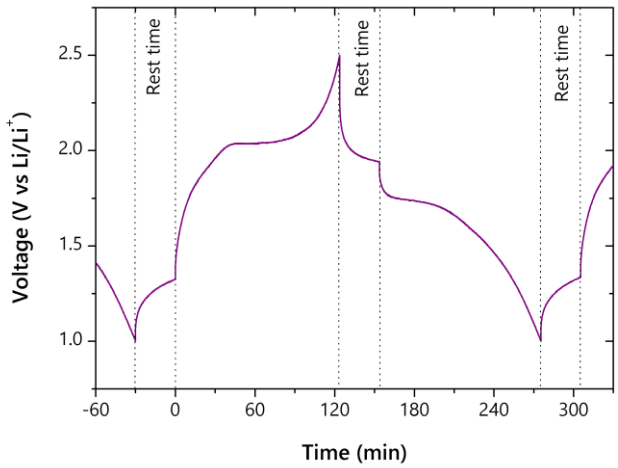


*Figure 6.1 Voltage profile of charge-discharge cycles at a rate of C/2 for $TiO_2$-TEGO (99:1) half-cell with 30 min rest time after each charge and each discharge process.*

Anatase is expected to reversibly accept lithium ions at a voltage of ~1.78-1.80 V vs Li at room temperature and additional lithium can be inserted at 1.56 V vs Li [7]. The lithium insertion was observed for all the investigated samples, as confirmed by the voltage drop to ~1.75-1.80 V, followed by a voltage plateau, during the discharge process. Similarly, the lithium extraction is indicated by the voltage plateau at ~1.90-1.95 V, reached after the fast increase in voltage during the charge process. The figure 6.2 illustrates the galvanostatic discharge-charge profile curves of $TiO_2$-TEGO and $TiO_2$-HT electrode-based materials in half-cell configuration, cycled at a rate of C/5 (5 h for discharging or charging).

Each discharge cycle can be divided into three regions. The first stage consists in a monotonic fast decrease in voltage, which is ascribed to the onset of the lithium insertion. The starting voltage is the value reached after the 30 minutes rest after each charge cycle. The second stage shows the plateau region at ~1.75-1.80 V, in which lithium is inserted into the electrode and two phases coexist. They are forming by lithium intercalation, which results in Li-rich and Li-poor phases corresponding to $Li_xTiO_2$ and anatase, respectively. The voltage decrease in the third region can be characterized by two different storage mechanisms. In one case, the presence of a second plateau (called as pseudo-plateau) is ascribed to a further intercalation of lithium into the bulk structure of the electrode material. The second mechanism can be recognized by a monotonous voltage decrease, corresponding to lithium storage occurring at nanoparticles interfacial surface [2].

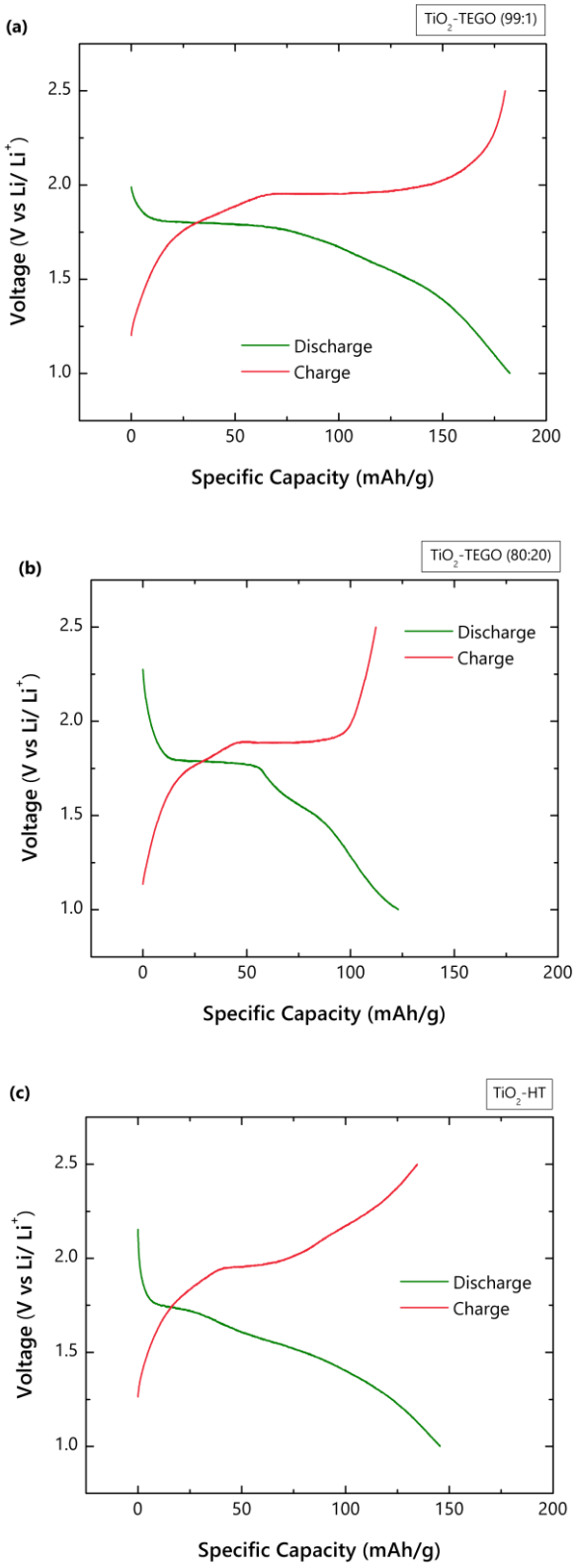


*Figure 6.2 Galvanostatic discharge-charge profiles vs $Li/Li^+$ at the rate of C/5 for half-cells of: (a) $TiO_2$-TEGO (99:1), (b) $TiO_2$-TEGO (80:20), (c) the reference $TiO_2$-HT.*

The rate performance of $TiO_2$-TEGO materials and $TiO_2$-HT are shown in figure 6.3, where specific discharge capacity is plotted against the number of cycles, at each C-rate. Remarkable, a good cycle stability is reached with both the $TiO_2$-TEGO tested materials. Conversely, the $TiO_2$-HT performance shows a very low cycle stability, especially at lower C-rate. At the discharge/charge rate of C/5, a large first specific discharge capacity of 184 mAh/g instantly drops after few cycles, decreasing by 50% at the $10^{th}$ cycle. At the same C-rate condition, in the $TiO_2$-TEGO (99:1) the capacity loss is reduced at 8% after 10 cycles. The behaviour of $TiO_2$-TEGO (80:20) at C/5 is slightly different from $TiO_2$-TEGO (99:1), being characterized by a strong irreversible capacity after the first cycle. However, after the initial capacity loss, a cycle stability is restored within few cycles.

At higher rates, the enhanced electrochemical performance of $TiO_2$-TEGO materials is even more evident from the increased specific capacity values, as shown in table 6.1. At the rate of 2C (30 min for discharging or charging), the specific capacity of both the $TiO_2$-TEGO electrode-based materials is significantly higher than the value obtained for the $TiO_2$-HT reference, without graphene. The half-cells prepared with $TiO_2$-TEGO reveal a specific capacity at least twice as much as the $TiO_2$-HT, confirming the better performance in the TEGO containing half-cells.

Furthermore, at the rate of 30 C (2 min for discharging or charging), the specific capacity of $TiO_2$-TEGO (80:20) is still significantly higher than that obtained with the $TiO_2$ electrode-based material without graphene, reaching 26 mAh/g compared to the almost negligible 8 mAh/g, respectively. For the $TiO_2$-TEGO (99:1) a greater capacity decay compared to the other $TiO_2$ material containing graphene is observed, yet the specific capacity is twice that of $TiO_2$ reference.

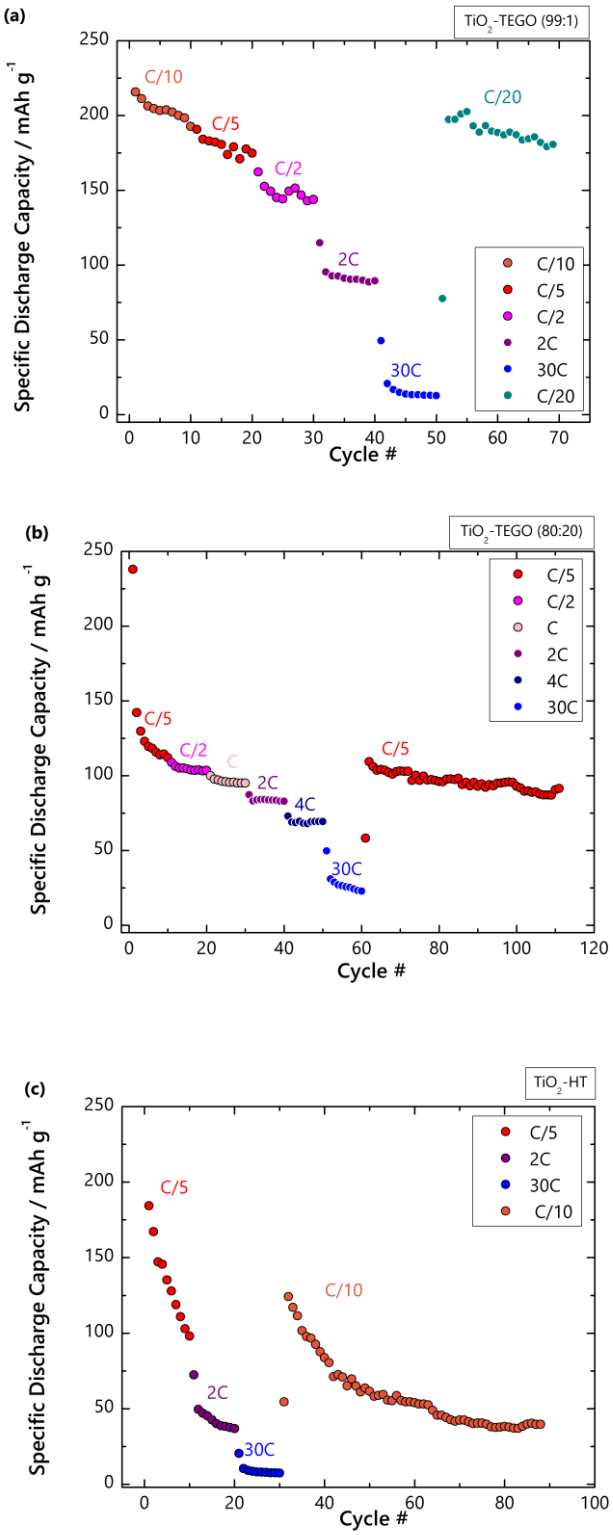


*Figure 6.3 Specific discharge capacity of (a) $TiO_2$-TEGO (99:1), (b) $TiO_2$-TEGO (80:20), (c) $TiO_2$-HT at different C-rates.*

*Table 6.1 Averaged discharge specific capacity values of $TiO_2$-TEGO and $TiO_2$-HT at the same C-rates. Uncertainty are considered from the standard deviation of ten cycles*

| C-rate | $TiO_2$-TEGO (99:1) [mAh/g] | $TiO_2$-TEGO (80:20) [mAh/g] | $TiO_2$-HT [mAh/g] |
|---|---|---|---|
| **C/5** | 180 ± 6 | 121 ± 10 | 134 ± 28 |
| **2C** | 91 ± 2 | 84 ± 1 | 42 ± 5 |
| **30C** | 15 ± 3 | 26 ± 3 | 8 ± 1 |

To study the storage mechanism in correspondence of the third region of the discharge profile, the voltage curves of $TiO_2$-TEGO were compared between the 1st and the 10th cycle at different C-rates. The 1st and the 10th discharge profiles of $TiO_2$-TEGO (99:1) are shown for each C-rate in figure 6.4a and 6.4b, respectively.

It is worth noting that a pseudo-plateau is observed for the slowest rate (C/10) at ~1.6 V, showing that a further lithium intercalation is achieved in the third part of the discharge process. The absence of the pseudo-plateau as the C-rate increases suggest that the dominant storage mechanism at higher rates is the interfacial storage, occurring at the surface of $TiO_2$ nanoparticles, which can store great amount of charge thanks to their high surface to volume ratio. This phenomenon can be promoted by the nanometre-sized of the $TiO_2$-TEGO materials, which was previously described in chapter 5. In the interfacial storage, lithium can be accommodated on the NPs surfaces, with a faster reaction kinetic than the intercalation in the bulk. For that reason, high C-rates are expected to encourage this mechanism, which can even damp the bulk insertion [2].

Comparing the specific capacity achieved at the 1st and at the 10th cycle, the capacity loss for the composite materials is remarkably lower than for the $TiO_2$-HT reference. Only ~10% of the initial capacity is lost after ten cycles for each rate, except for the 2C where a 22% capacity loss is observed. Conversely, in the $TiO_2$-HT based electrode without graphene, a 50% capacity loss occurs both for low and high rates. The improved capacity retention of $TiO_2$-TEGO (99:1) is shown in figure 6.5, where the 1st, 2nd and 10th charge-discharge profiles at the C-rate of C/5 are shown.

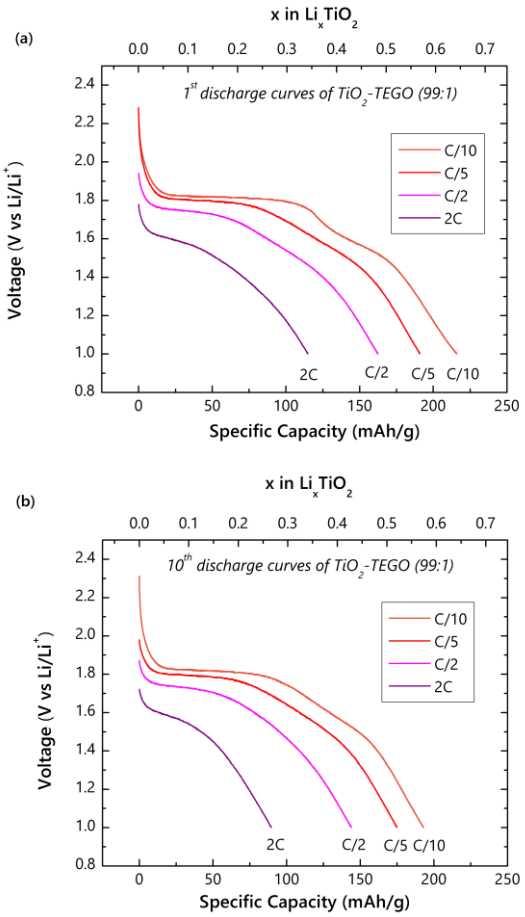


*Figure 6.4 Voltage discharge curves of $TiO_2$-TEGO (99:1) at different C-rates during (a) the 1st and (b) the 10th cycle.*

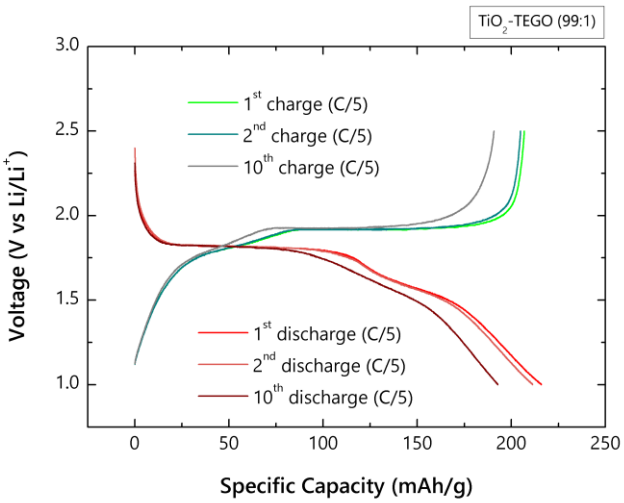


*Figure 6.5 Galvanostatic charge-discharge curves of $TiO_2$-TEGO (99:1) at the rate of C/5. The 1st, 2nd and 10th cycles are shown.*

The voltage discharge profiles were studied for the $TiO_2$-TEGO (80:20) as well, as shown in figure 6.6. At the rate of C/5, a large first discharge capacity is observed, with 238 mAh/g. However, a significant capacity loss is observed from the first and the last discharge curve during the ten cycles at C/5. At a deeper analysis, the initial capacity is not retained after the first discharge, showing an irreversible behaviour with a strong decrease in the subsequent charge capacity (figure 6.7). Then, from the $2^{nd}$ to the $10^{th}$ cycle, the 80% of the capacity is retained.

The irreversible behaviour can be explained with the trapping of $Li^+$ in the $TiO_2$-TEGO matrix during the first discharge process, without its complete extraction during the charge process. It is well known that TEGO shows a strong irreversibility after the first few cycles. Lithium content trapped in TEGO-based electrode amounts to 89% after the first discharge, leaving only 11% Li for the reversible cycles. A portion of the trapped lithium can be associated with the formation of the solid electrolyte interface (SEI) on the graphene surface. Thus, the sites where lithium ions are trapped can be no longer used for the reversible intercalation/de-intercalation process, resulting in a decrease of the stored charge [8].

In $TiO_2$-TEGO (80:20), a content of 20% of TEGO in the electrode can be responsible of this effect, which is negligible when the amount of TEGO is reduced to 1% in $TiO_2$-TEGO (99:1) half-cells. Except for the slowest rate of C/5, the $TiO_2$-TEGO (80:20) half-cell exhibits a high capacity retention at each rate, with a capacity loss after ten cycles amounting to only 5%.

As for $TiO_2$-TEGO (99:1), the pseudo-plateau at ~1.6 V is observed, confirming the further lithiation occurring in the third part of the discharge. The existence of this pseudo-plateau is verified up to higher rate than for the $TiO_2$-TEGO (99:1), vanishing at the rate of 2C. A possible explanation is given by the lithium content intercalated into $TiO_2$, which is lower than in the previous sample. At the rate of 1C, only a small fraction ($x \sim 0.2$) of Li per $TiO_2$ is inserted at the end of the plateau region, suggesting that more ions can be further intercalated before reaching the fraction of fully reversible limit ($x=0.5$). At faster rates, the interfacial storage is preferred, as expected, in accordance with the results for $TiO_2$-TEGO (99:1).

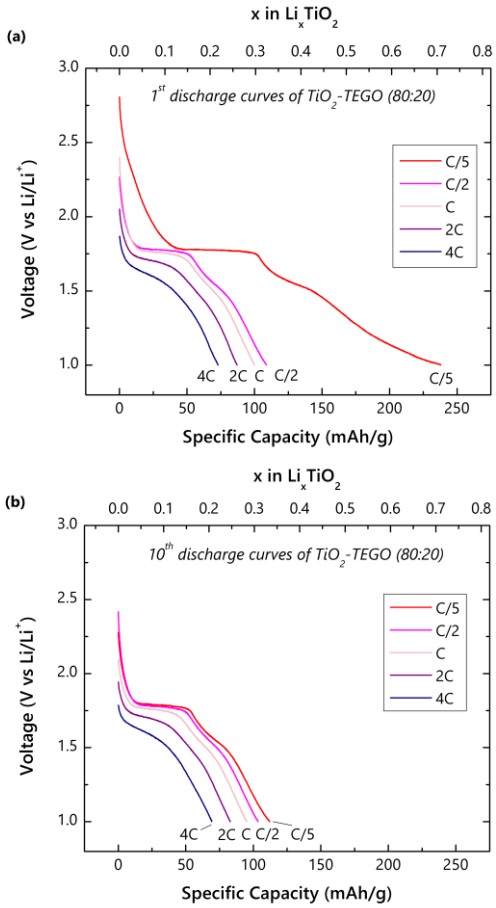


*Figure 6.6 Voltage discharge curves of $TiO_2$-TEGO (80:20) at different C rates during (a) the 1st and (b) the 10th cycle.*

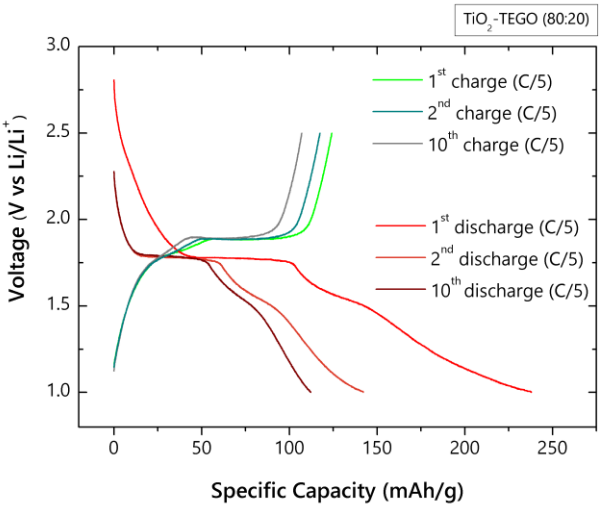


*Figure 6.7 Galvanostatic charge-discharge curves of $TiO_2$-TEGO (80:20) at the rate of C/5. The 1st, 2nd and 10th cycles are shown.*

The excellent capacity retention which are achieved for both the $TiO_2$-TEGO based half-cells can be ascribed to the effectiveness of the graphene (TEGO) support in the electrode material. Thanks to its high conductivity up to ~20 S/cm (corresponding to a resistivity of $\rho \sim 5 \cdot 10^{-2}$ Ω·cm), a conductive network results in the combination of TEGO with $TiO_2$ NPs, achieving a fast transfer of electrons. In addition, the high surface area of TEGO (~500 $m^2/g$) [9] is expected to reduce the NPs agglomeration, ensuring good electrochemical performance. Lastly, even if the total change in volume of the $TiO_2$ cell during lithiation and de-lithiation processes is expected to be low (3-4%) [10], the flexibility of the folded TEGO layers can buffer the irreversible change in volume of NPs.

### 6.1.2 Electrochemical results of $TiO_2$-TEGO-BM electrodes

The half-cells made of $TiO_2$-TEGO-BM as active material in the electrode were tested to investigate the electrochemical performance of the ball milled material. The devices underwent charge and discharge cycles between 1 V and 2.5 V (vs $Li/Li^+$) at a fixed current level (C-rate). Several C-rates have been tested to evaluate the rate capability also at high rate. The results of galvanostatic charge-discharge measurements are here discussed and compared to those obtained for the half-cell containing the $TiO_2$-TEGO (80:20) based electrode, in order to make a comparison among the electrochemical properties of the materials, which were prepared following two different approaches.

The lithium insertion and extraction were confirmed by the voltage profiles shown in figure 6.8. During discharging, the voltage drop is observed up to ~1.78 V, whereas during charging the voltage plateau occurs at ~1.92 V. From the third region of the discharge process it can be inferred that the interfacial storage mechanism is dominant compared to the bulk lithium insertion, as suggested by the monotonous decreasing trend of the curve.

The rate performance of $TiO_2$-TEGO-BM materials is shown in figure 6.9, where specific discharge capacity is plotted against the number of cycles at each C-rate.

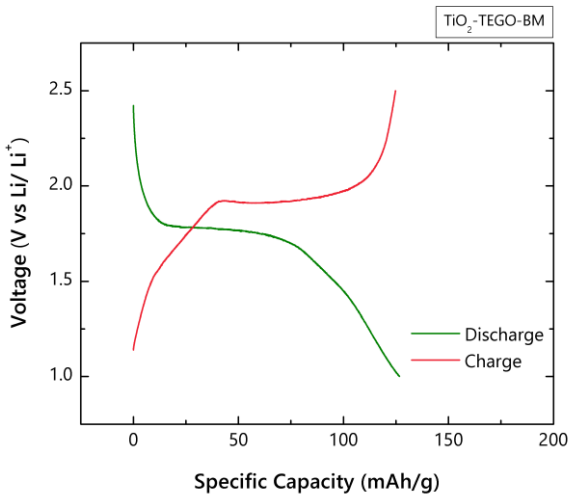


*Figure 6.8 Galvanostatic discharge-charge profile vs $Li/Li^+$ for half-cell of $TiO_2$-TEGO-BM.*

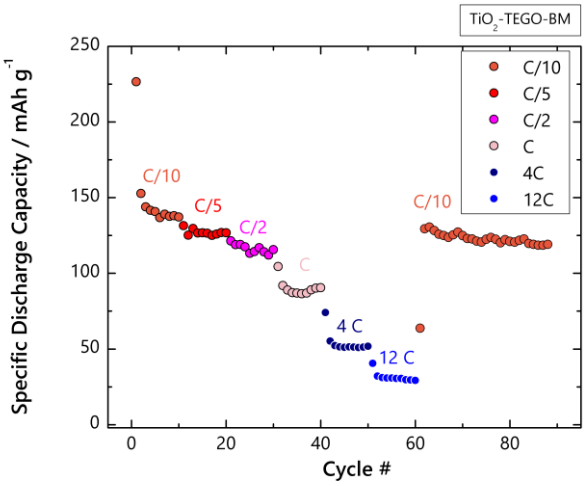


*Figure 6.9 Specific discharge capacity of $TiO_2$-TEGO-BM at different C-rates.*

The half-cell shows good cycle stability at different C-rates. It is worth pointing out that a capacity retention of at least 90% is achieved within the initial ten cycles, except for the lowest C-rate. At C/10, a large first discharge capacity is reached, with 227 mAh/g, yet an irreversible behaviour is observed in the subsequent charge cycle (figure 6.10). However, from the 2$^{nd}$ to the 10$^{th}$ cycle, the 90% of the capacity is retained. This effect can be ascribed to the TEGO graphene content in the electrode, as observed for the electrode containing the hydrothermally synthesized material with a similar $TiO_2$:TEGO content.

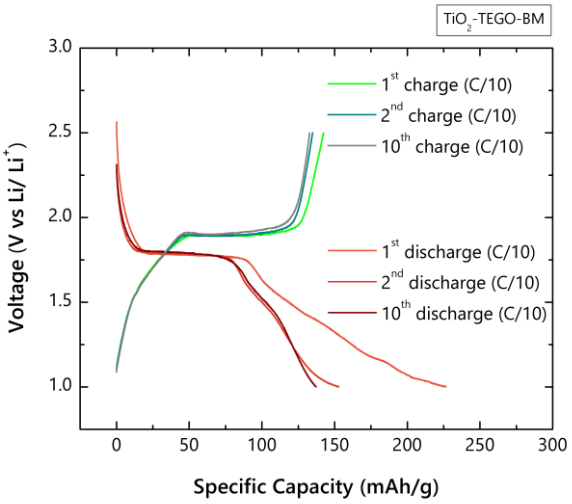


*Figure 6.10 Galvanostatic charge-discharge curves of $TiO_2$-TEGO-BM at the rate of C/10. The 1st, 2nd and 10th cycles are shown.*

The figure 6.11 compares the rate capability of the two kind of materials with similar $TiO_2$:TEGO content, at the same C-rate. The good cyclability achieved with the ball milled material is confirmed, as inferred from the specific discharge values, which are comparable to those related to the chemically synthesized material. However, it is worth noting that the hydrothermal nanostructured material shows a better rate capability at higher C-rates, as seen for the rate 4C in the figure. The averaged specific discharge capacity values are summarized in table 6.2. As a possible explanation of this effect, the different nanocrystals dimension in the materials can be considered. Anatase nanoparticles of about 10 nm in $TiO_2$-TEGO (80:20) are smaller than in the ball milled material, as already observed and discussed in chapter 5. It is known that lithium fraction which can be stored relies on the dimension of nanocrystals in the electrode material. As the nanocrystal size decreases below 10 nm, a higher specific capacity can be achieved thanks to the lithium diffusion, which is supported by the smaller size, and to the greater stored charge occurring at the surface of nanoparticles. In addition, the faster kinetic of surface storage can ensure higher charge and discharge rates to be sustained from the device [2,11]. In figure 6.12 the discharge curves of $TiO_2$-TEGO (80:20) and $TiO_2$-TEGO-BM are compared at the rate of 4C, showing the expansion in the third region of the voltage profile and a resulting higher stored charge for the hydrothermally nanostructured material.

*Table 6.2 Averaged specific discharge capacity values of $TiO_2$-TEGO-BM and $TiO_2$-TEGO (80:20) at the same C-rates.*

| C-rate | $TiO_2$-TEGO-BM [mAh/g] | $TiO_2$-TEGO (80:20) [mAh/g] |
|---|---|---|
| **C/5** | 127 ± 2 | 121 ± 10 |
| **C/2** | 116 ± 3 | 105 ± 2 |
| **C** | 89 ± 2 | 96 ± 2 |
| **4C** | 52 ± 1 | 69 ± 1 |

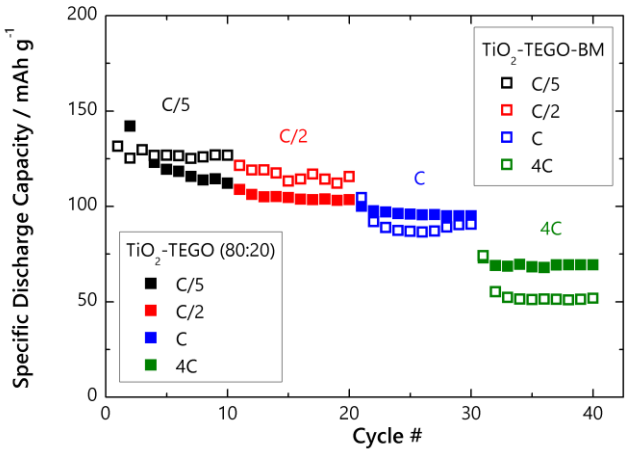


*Figure 6.11 Specific discharge capacity of $TiO_2$-TEGO (80:20) (full squares) and $TiO_2$-TEGO-BM (open squares).*

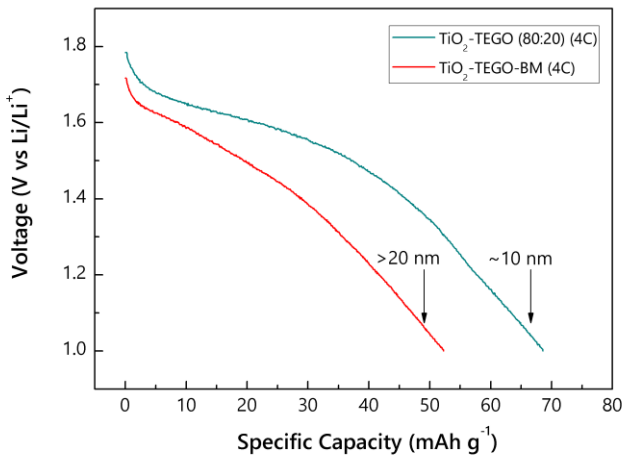


*Figure 6.12 Discharge profiles of $TiO_2$-TEGO-BM and $TiO_2$-TEGO (80:20) at the rate of 4C.*

### 6.1.3 Discussion

The $TiO_2$-TEGO materials, both from the hydrothermal synthesis and the high-energy ball milling treatment, show good electrochemical properties as electrodes for lithium ion batteries.

Regarding the chemically prepared $TiO_2$-TEGO, the combined materials give an evidence of the increased performance compared to that of pristine $TiO_2$-HT based electrode, without TEGO. The effectiveness of graphene sheets is demonstrated by the good cycling stability achieved when TEGO is used as a support for the growth of $TiO_2$ nanoparticles. Secondly, the high electrical conductivity of graphene promotes fast charge transfer, ensuring high rate capabilities for the devices. In addition, the presence of nanostructured materials within the electrode also contributes to fast charge and discharge rates and reduces the irreversibility connected to the trapping of $Li^+$ in graphene matrix. The improved specific capacity in $TiO_2$-TEGO half-cells compared to the $TiO_2$-HT ones demonstrates that graphene can create a conductive network, which both enables an efficient transport of the electrons and prevents the agglomeration of $TiO_2$ nanoparticles.

Specifically, the two different contents of $TiO_2$ and TEGO, which were combined in the nanostructured material, give slightly different electrochemical properties, as seen from the irreversible behaviour connected to the presence of TEGO. Thus, the $TiO_2$-TEGO (99:1) material results in better performance, much higher than the pristine $TiO_2$ based electrodes and even preferable to a considerably higher relative content of graphene.

On the other hand, the attempted route of using high-energy ball milling to combine $TiO_2$ and graphene has been demonstrated to be successful, thanks to the effectiveness of $TiO_2$-TEGO-BM based electrodes. Specifically, comparable performance has been shown by ball milled product with equal $TiO_2$:TEGO content as for hydrothermally materials. The influence of the nanoparticle size on the stored charge has to be stressed in the production of the electrode. Further investigation in combining smaller nanoparticles to graphene with ball milling treatments could give even better electrochemical performance.

## References


[1] M. Madian, A. Eychmüller, L. Giebeler, Current advances in Tio 2 -based nanostructure electrodes for high performance lithium ion batteries, Batteries. 4 (2018). https://doi.org/10.3390/batteries4010007.

[2] J.Y. Shin, D. Samuelis, J. Maier, Sustained lithium-storage performance of hierarchical, nanoporous anatase TiO2 at high rates: Emphasis on interfacial storage phenomena, Adv. Funct. Mater. 21 (2011) 3464–3472. https://doi.org/10.1002/adfm.201002527.

[3] P. Kubiak, T. Fröschl, N. Hüsing, U. Hörmann, U. Kaiser, R. Schiller, C.K. Weiss, K. Landfester, M. Wohlfahrt-Mehrens, TiO2 anatase nanoparticle networks: Synthesis, structure, and electrochemical performance, Small. 7 (2011) 1690–1696. https://doi.org/10.1002/smll.201001943.

[4] H. Lindström, S. Södergren, A. Solbrand, H. Rensmo, J. Hjelm, A. Hagfeldt, S.E. Lindquist, Li+ion insertion in TiO2(anatase). 1. Chronoamperometry on CVD films and nanoporous films, J. Phys. Chem. B. 101 (1997) 7710–7716. https://doi.org/10.1021/jp970489r.

[5] D. Wang, D. Choi, J. Li, Z. Yang, Z. Nie, R. Kou, D. Hu, C. Wang, L. V Saraf, J. Zhang, I.A. Aksay, J. Liu, Self-Assembled TiO2–Graphene Hybrid Nanostructures for Enhanced Li-Ion Insertion, ACS Nano. 3 (2009) 907–914. https://doi.org/10.1021/nn900150y.

[6] T.F. Fuller, M. Doyle, J. Newman, Relaxation Phenomena in Lithium Ion Insertion Cells, J. Electrochem. Soc. 141 (1994) 982–990. https://doi.org/10.1149/1.2054868.

[7] B. Zachau-Christiansen, K. West, J. Jacobsen, S. Atlung, Lithium Insertion in Different TiO2 modifications, Solid State Ionics. 28 (1988) 1176–1182. https://doi.org/10.1016/0167-2738(88)90352-9.

[8] J.C. Pramudita, D. Pontiroli, G. Magnani, M. Gaboardi, M. Riccò, C. Milanese, H.E.A. Brand, N. Sharma, Graphene and Selected Derivatives as Negative Electrodes in Sodium- and Lithium-Ion Batteries, ChemElectroChem. 2 (2015) 600–610. https://doi.org/10.1002/celc.201402352.

[9] M. Gaboardi, A. Bliersbach, G. Bertoni, M. Aramini, G. Vlahopoulou, D. Pontiroli, P. Mauron, G. Magnani, G. Salviati, A. Züttel, M. Riccò, Decoration of graphene with nickel nanoparticles: Study of the interaction with hydrogen, J. Mater. Chem. A. 2 (2014) 1039–1046. https://doi.org/10.1039/c3ta14127f.

[10] M. Wagemaker, G.J. Kearley, A.A. Van Well, H. Mutka, F.M. Mulder, Multiple Li positions inside oxygen octahedra in lithiated TiO2 anatase, J. Am. Chem. Soc. 125 (2003) 840–848. https://doi.org/10.1021/ja028165q.

[11] J. Wang, J. Polleux, J. Lim, B. Dunn, Pseudocapacitive contributions to electrochemical energy storage in TiO 2 (anatase) nanoparticles, J. Phys. Chem. C. 111 (2007) 14925–14931. https://doi.org/10.1021/jp074464w.

# 7 $TiO_2$-LSGO nanostructured materials for micro-supercapacitors

In this chapter the characterization of materials obtained by the LightScribe® technique will be discussed. Their electrochemical performance as electrodes of laser-scribed supercapacitors will be shown in the next chapter. Nanostructured materials based on $TiO_2$-graphene were simultaneously obtained through the LightScribe technique, by using a DVD burner laser. During the laser treatment, both the $TiO_2$ precursor (TTIP) and the graphite oxide (GO) were converted into the combined nanostructured material ($TiO_2$-LSGO, as Laser-Scribed Graphite Oxide).

Recently, as discussed in sections 3.6 and 3.7, the great attention on laser-scribed techniques to produce interdigitated micro-supercapacitors has exploited the promising features of graphene as electrodes material and several investigations to produce graphene-based materials by means of lasers (LIG) have been attempted [1–3]. Among several methods, a scalable and cost-effective process makes use of the LightScribe® technology with a DVD burner laser, as first investigated by Kaner and his group [4]. By this route, up to a hundred of micro-supercapacitors can be built in few minutes, with a planar architecture, consisting of interdigitated patterns.

In this research, the LightScribe technique developed by Kaner's group was further exploited to improve the electrochemical performance of laser-scribed interdigitated electrodes. The greatest advantage of this technique is the possibility to obtain nanostructured materials with a straightforward approach, without involving multi-step process. By means of the addition of a $TiO_2$ precursor to the graphite oxide, an enhancement in the electrochemical properties of the material has been expected and successfully confirmed from the electrochemical results. The novelty of this process consists into the simultaneous synthesis of $TiO_2$ and graphene into a composite nanostructured material.

In order to obtain devices with high-power and high-energy densities, the combination of the graphene properties and the effects introduced by $TiO_2$ has been investigated. The enhancement in the electrochemical properties due to Faradaic effects will be illustrated in the next chapter.

The microstructure of $TiO_2$-graphene based materials will be described here to highlight the formation of $TiO_2$ nanoparticles onto Laser-Scribed Graphite Oxide (LSGO). The nanostructured material will be henceforth called $TiO_2$-LSGO. The characterization of the $TiO_2$-LSGO materials has been carried out both on pristine LSGO and on the composite material.

## 7.1 Laser-scribed interdigitated patterns

As described in section 3.6.1, the LightScribe technology can produce graphene-based materials starting from carbonaceous precursors through a carbon-based coating deposited onto the surface of a LightScribe disc. The laser conversion during the burning process can lead to the formation of graphene-based materials [4].

Here, a coated LightScribe DVD was prepared, as previously described in section 4.3.1. For the LSGO, the GO-coated LightScribe disc underwent the laser-scribe process, by means of the infrared laser at 780 nm of the DVD burner. The shape of the electrodes with interdigitated patterns is drawn using the LightScribe *Nero CoverDesigner* software and then laser-scribed on the disc during the process. The patterns consist of micro-sized lines which were produced by the laser, with a spatial resolution of ~20 μm. It should be noted that between one line and the nearest one, some space is left and the disc coating is not irradiated, resulting composed of pristine materials containing the initial reagents. In contrast, where the laser burns the surface, the transformation of the reagents into products occur. Pictures and optical magnifications of the irradiated patterns are shown in figure 7.1 where they appear as black lines. In correspondence of irradiated patterns, nanostructured materials can be obtained, namely based on $TiO_2$ and Laser-Scribed Graphite Oxide, starting from titanium isopropoxide (TTIP) and graphite oxide (GO) as precursors, respectively.

The non-irradiated parts represent a limit of the LightScribe system, due to the insulating behaviour of pristine GO, as it will be described in the next paragraph. To reduce this intrinsic drawback of the writing system, the interdigitated patterns were radially arranged: since the writing proceeds in concentric circles, this configuration ensures that electrode is

made of approximately parallel irradiated lines. In this way, there is no crosswise interruption of insulating material within each line and the charge can be collected.

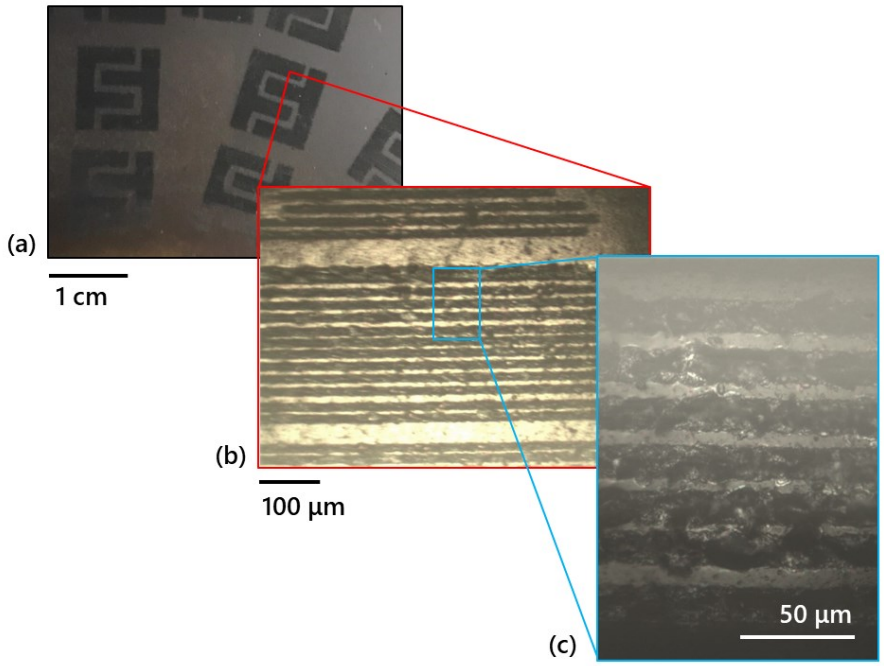


*Figure 7.1 (a) Picture of laser-scribed interdigitated patterns; (b) and (c) optical micrographs of laser-scribed interdigitated patterns.*

In literature, the conversion mechanism operated by the laser is still under discussion. In particular it is not yet clear if consists in a phototermal or photochemical reaction, or both. In this case, a photothermal process is likely to be expected, since the laser wavelength is in the infrared range. The lattice vibration resulting from the absorption of the infrared light can induce thermal effects with locally high temperatures (>$10^3$ °C). At this temperature, the break of C-O and C=O bonds can occur with gaseous release. The irradiated material results in a higher relative content of carbon compared to the pristine one, due to the deoxygenation during the laser scribing process [3,5].

In addition, the thermal heating can produce an expansion in the carbon structure, with the formation of ripples. The resulting curvature of the surface results in the creation of a defective structure, which typically consists of heptagons and pentagons, locally replacing the hexagonal lattice [3]. These defects can promote the functionalization of the material with the growth of nanoparticles, as expected in this case.

## 7.2 Laser-Scribed Graphite Oxide

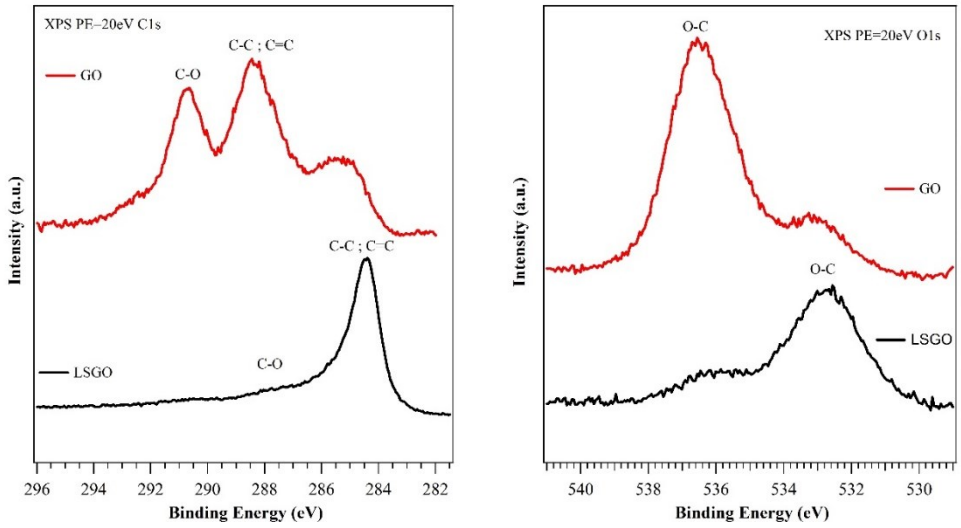


*Figure 7.2 XPS spectra of C1s and O1s core levels of graphite oxide (GO) and laser-scribed graphite oxide (LSGO) samples, PE=20 eV. C1s spectra (on the left) are normalized in peak height; O1s spectra (on the right) are plotted on the same intensity scale.*

Graphite oxide (GO) was used as carbonaceous precursor for producing the laser-induced graphene-based material. A GO by Hummers' method was preferred, due to its hydrophilicity and the resulting possibility to use water as solvent in the preparation of a homogeneous dispersion to coat the LightScribe disc. The graphene-based material obtained with the laser treatment will be hereafter called laser-scribed graphite oxide (LSGO).

To evaluate the effect of the laser treatment, XPS analysis is used to reveal the changes in chemical surface properties. Core levels spectra of C1s and O1s have been acquired at high resolution (PE=20 eV) and they are shown in figure 7.2. Peaks positions for the GO sample are shifted at higher binding energy (BE) by +3.8 eV, due to charge shift phenomena: if the sample is not conductive, the photoelectron generation process gives rise to a residual charge on the surface, that leads to BE shifts not related to changes in the chemical environment. After the laser treatment, this charge shift is not detected and the peak positions are reliable. Peak assignment and charge shift calculation have been performed using internal standards (GO and graphene), confirming that the charge shift is due to charging phenomena [6].

The C1s core level in GO suggests two main species at 288.3 eV and 290.7 eV, and another peak at lower BE, due to contamination (sample exposure to air was minimized, but some contamination is unavoidable): considering the mentioned charge shift, the main peak BE is at 284.5 eV, a value typical of graphene, while the second component at 286.9 eV can be ascribed to C-O bonds, as expected for the graphite oxide. The laser treatment has a deep effect of the surface, as shown in LSGO spectra. The C-O component is almost completely suppressed and the graphene peak, positioned at 284.5 eV, is more defined. O1s core level (shown in the same figure and plotted without normalization, to highlight the intensity difference) follows the same trend, with suppression of the graphite oxide component and charge shift compensation. Some oxygen contamination is found also after the laser treatment.

The conversion of GO into LSGO is also characterized by an increase in the electrical conductivity of three order of magnitude, as shown in figure 7.3. Electrical measurements on a sheet 0.1 mm thick yield an electrical resistance R=39 kΩ for LSGO, corresponding to an electrical conductivity $\sigma \sim 5 \cdot 10^{-4}$ S/cm. Before the laser treatment, the electrical resistance of pristine GO gives R=42 MΩ, with a $\sigma \sim 5 \cdot 10^{-7}$ S/cm. The increase in electrical conductivity confirms the effect of laser treatment, which induces the conversion from graphite oxide, showing insulating behaviour, to laser-scribed graphite oxide, with much higher electrical conductivity. However, the electrical conductivity of LSGO is lower than typical values of graphene (ranging from few S/cm up to $10^2$ S/cm [7,8]). It is known that electrical conductivity strongly depends on the precursor features, including the synthesis condition, as well as on the level of oxidation. The high content of oxygen bonded to the carbon network in GO, as well as defects and vacancies are responsible to the energy band gap of GO. The residual oxygen atoms bonded to carbon network after the laser treatment, as detected by XPS analysis, are expected to contribute to the lower value of conductivity compared to graphene. In addition, the presence of defects, related to the wrinkly structure, should be considered as a limit to achieve outstanding conductivity values [9]. However, the increase in the electrical conductivity from GO to LSGO is significant and the laser-scribed material is suitable for application in supercapacitors.

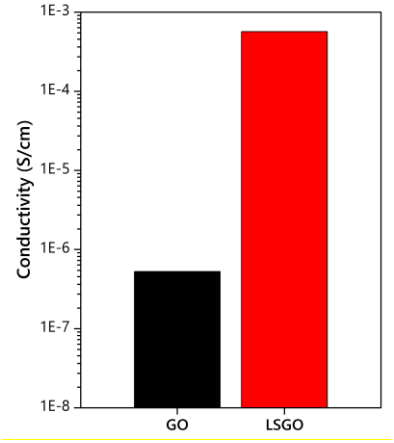


*Figure 7.3 Comparison of electrical conductivity in graphite oxide (GO) and laser-scribed graphite oxide (LSGO).*

## 7.3 $TiO_2$-LSGO

The combined material was obtained with the same method of LSGO, by LightScribe technique. The production of $TiO_2$ nanoparticles onto LSGO ($TiO_2$-LSGO) by LightScribe represents the novelty of the process in the field, compared to the pioneer work of Kaner and his group [4].

$TiO_2$-LSGO has been obtained adding titanium isopropoxide (TTIP) as $TiO_2$ precursor in the preparation of the disc coating. Then, the TTIP-GO-coated LightScribe disc underwent laser-writing process into the DVD burner. Remarkably, the process has successfully promoted the growth of $TiO_2$ nanoparticles (NPs), starting from TTIP, along with the simultaneous conversion of graphite oxide in LSGO. The local increase in temperature as a result of the absorption of laser radiation by graphite oxide promotes the crystallization of NPs, along with the conversion of GO into LSGO.

The composite material reveals the presence of nanostructured $TiO_2$ on the surface of LSGO. A widespread decoration of nanoparticles has been observed on the surface of LSGO, as highlighted in STEM images in figures 7.4a-b. Nanometre-sized crystalline $TiO_2$ particles cover the whole matrix, up to the edges (figure 7.5). In figure 7.6, the extensive distribution of titanium and oxygen is confirmed by the elemental maps performed by STEM-EDX in the region shown in figure 7.6a. It is worth pointing out that no agglomeration of NPs has been observed. However, the nanoparticle size distribution is not fully homogeneous. From a statistical analysis of about 1000 particles, the 90% of NPs reveals a diameter under 9 nm, yet the average diameter is 3 nm, as shown in figure 7.7. The HRTEM images of NPs in figure 7.4c-d show examples of some of the bigger NPs with about 15-25

nm diameter, having a nearly spherical and a slightly elongated shapes, where the interplanar space of 4.8 Å corresponds to the (002) planes of anatase $TiO_2$. The presence of anatase as $TiO_2$ polymorph is confirmed by the main $E_g$ anatase vibrational mode in the Raman spectrum at 144 $cm^{-1}$, shown in figure 7.8. Despite most of the $TiO_2$ NPs have diameter well below 10 nm, the small percentage having bigger dimension determines that the position of the main anatase peak is found at 144 $cm^{-1}$, as expected for crystalline nanoparticles of about 20 nm or larger. Along with the anatase feature, the characteristic D and G bands of graphene-based materials are observed at ~1370 $cm^{-1}$ and ~1600 $cm^{-1}$, respectively. The presence of the broad D band confirms the highly defective structure of LSGO.

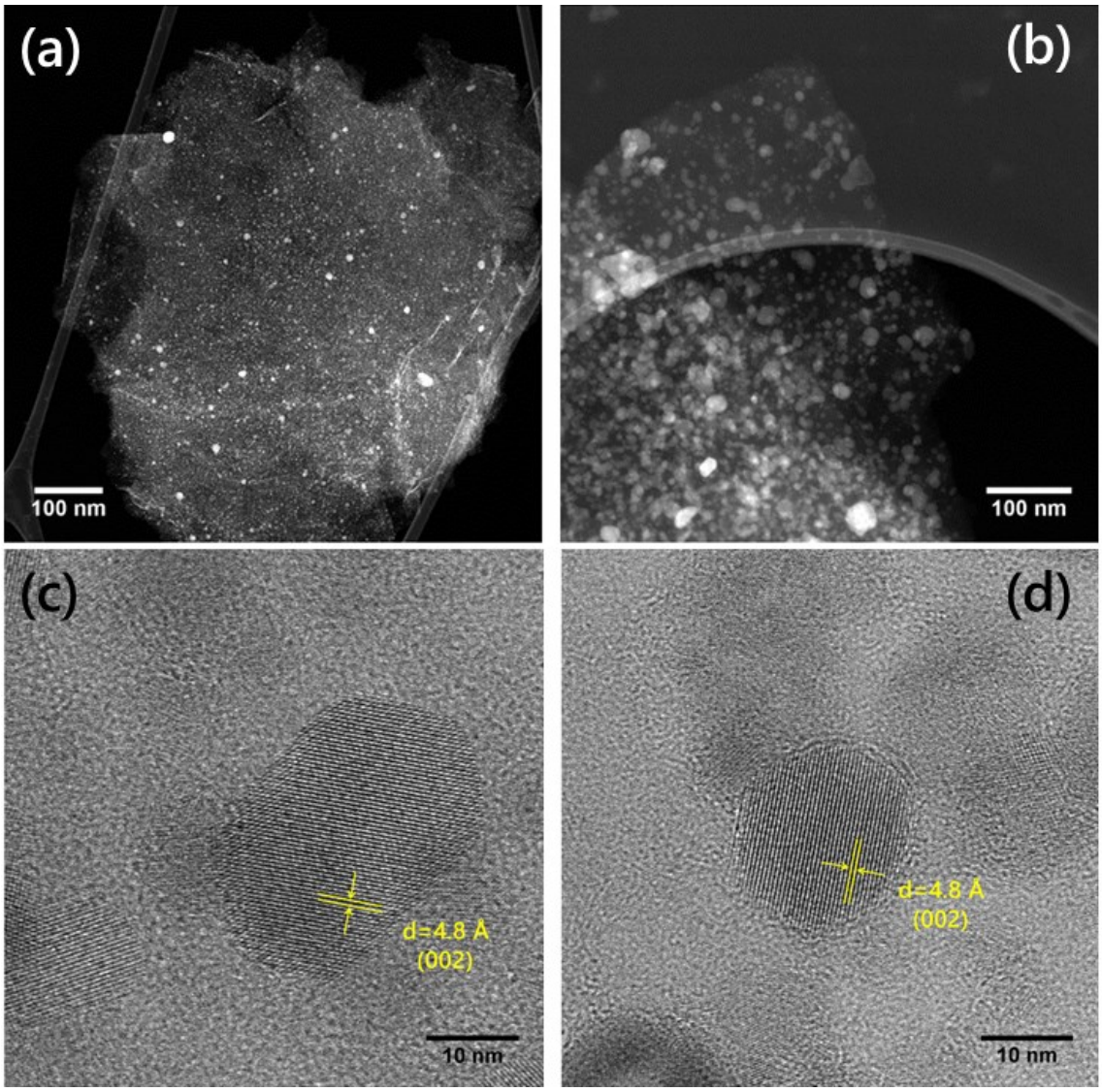


*Figure 7.4 (a-b) STEM images and (c-d) HRTEM images of $TiO_2$-LSGO. The (002) anatase planes are highlighted by the yellow arrows.*

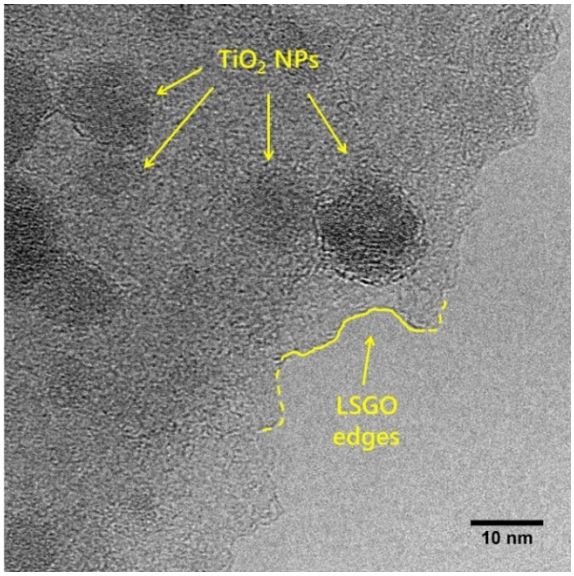


*Figure 7.5 HRTEM image of $TiO_2$-LSGO near the material edges.*

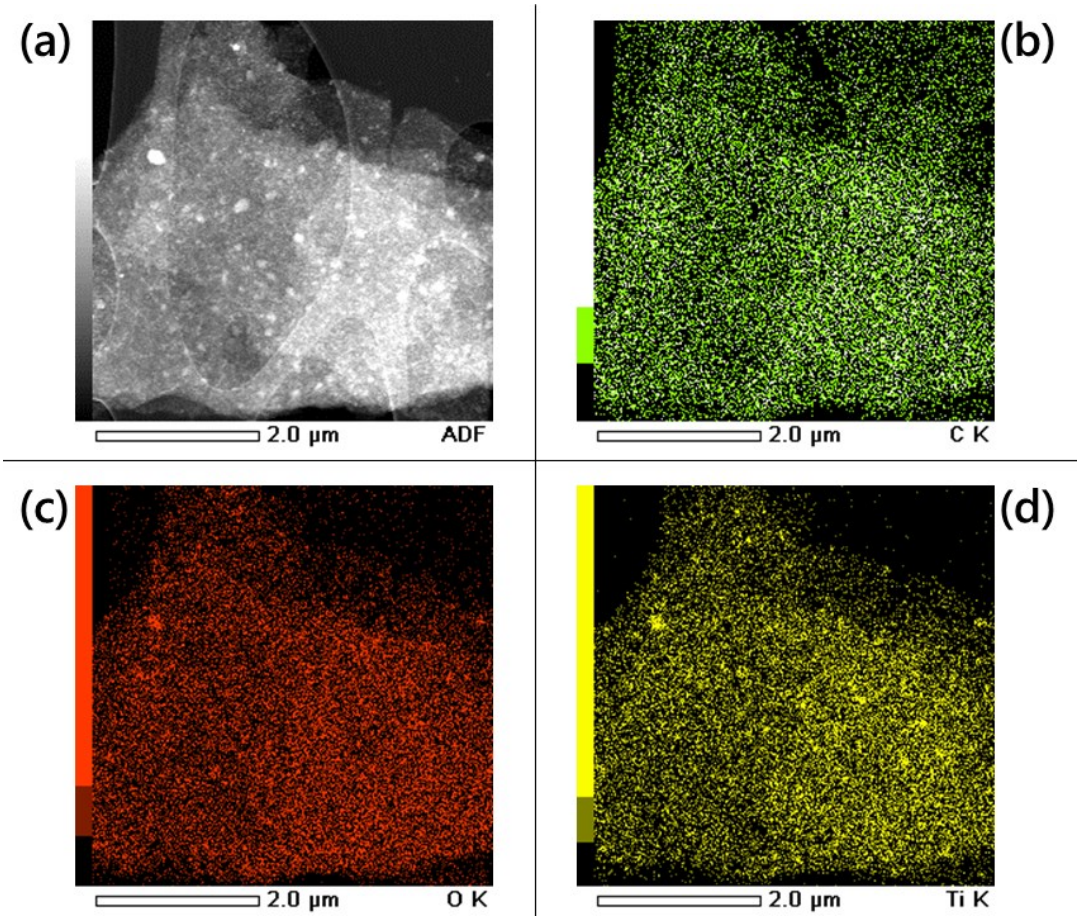


*Figure 7.6 (a) STEM image of $TiO_2$-LSGO and (b,c,d) EDX elemental maps on C, O, Ti, respectively.*

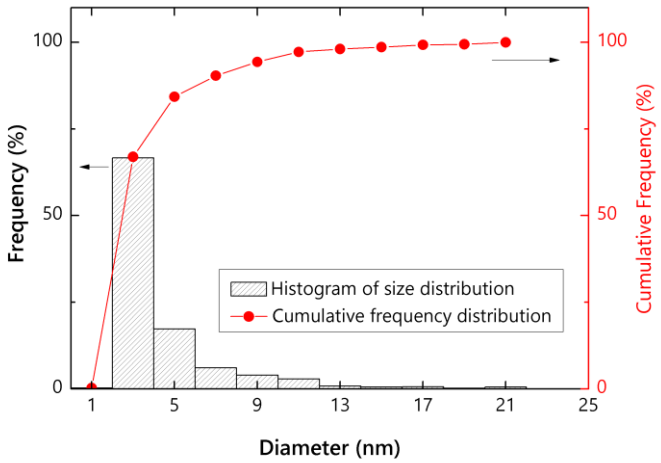


*Figure 7.7 Diameter size distribution obtained by a statistical analysis of about 1000 NPs (in gray) and cumulative frequency curve (in red).*

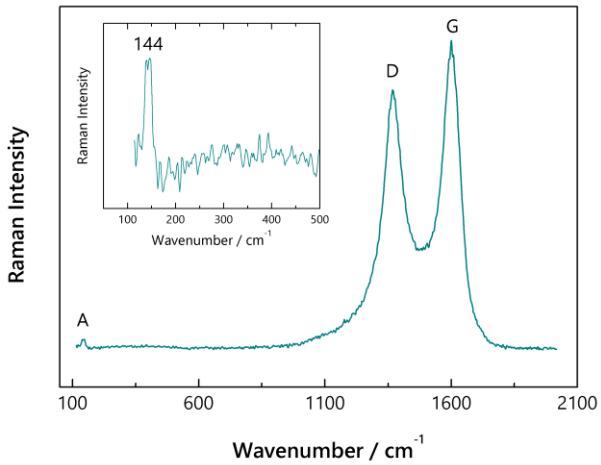


*Figure 7.8 Raman spectrum of $TiO_2$-LSGO with the most intense anatase $E_g$ vibrational mode (A) and characteristic graphene-based materials bands (D and G). In the inset the main anatase peak is zoomed. The Raman spectrum was acquired with the excitation laser at 473.1 nm.*

## References


[1] W. Gao, N. Singh, L. Song, Z. Liu, A.L.M. Reddy, L. Ci, R. Vajtai, Q. Zhang, B. Wei, P.M. Ajayan, Direct laser writing of micro-supercapacitors on hydrated graphite oxide films, Nat. Nanotechnol. 6 (2011) 496–500. https://doi.org/10.1038/nnano.2011.110.

[2] P. Nayak, N. Kurra, C. Xia, H.N. Alshareef, Highly Efficient Laser Scribed Graphene Electrodes for On-Chip Electrochemical Sensing Applications, Adv. Electron. Mater. 2 (2016) 1–11. https://doi.org/10.1002/aelm.201600185.

[3] J. Lin, Z. Peng, Y. Liu, F. Ruiz-Zepeda, R. Ye, E.L.G. Samuel, M.J. Yacaman, B.I. Yakobson, J.M. Tour, Laser-induced porous graphene films from commercial polymers, Nat. Commun. 5 (2014) 1–8. https://doi.org/10.1038/ncomms6714.

[4] M.F. El-Kady, R.B. Kaner, Scalable fabrication of high-power graphene micro-supercapacitors for flexible and on-chip energy storage, Nat. Commun. 4 (2013) 1475–1479. https://doi.org/10.1038/ncomms2446.

[5] A. Longo, R. Verucchi, L. Aversa, R. Tatti, A. Ambrosio, E. Orabona, U. Coscia, G. Carotenuto, P. Maddalena, Graphene oxide prepared by graphene nanoplatelets and reduced by laser treatment, Nanotechnology. 28 (2017) 224002. https://doi.org/10.1088/1361-6528/aa6c3c.

[6] G. Greczynski, L. Hultman, X-ray photoelectron spectroscopy: Towards reliable binding energy referencing, Prog. Mater. Sci. 107 (2020) 100591. https://doi.org/10.1016/j.pmatsci.2019.100591.

[7] X. Wang, L. Zhi, K. Müllen, Transparent, conductive graphene electrodes for dye-sensitized solar cells, Nano Lett. 8 (2008) 323–327. https://doi.org/10.1021/nl072838r.

[8] X. Li, W. Cai, I. Jung, J. An, D. Yang, A. Velamakanni, R. Piner, L. Colombo, R.S. Ruoff, Synthesis, Characterization, and Properties of Large-Area Graphene Films, ECS Trans. 19 (2009) 41–52. https://doi.org/10.1149/1.3119526.

[9] I. Jung, D.A. Dikin, R.D. Piner, R.S. Ruoff, Tunable electrical conductivity of individual graphene oxide sheets reduced at 'Low' temperatures, Nano Lett. 8 (2008) 4283–4287. https://doi.org/10.1021/nl8019938.

# 8 Electrochemical performance of $TiO_2$-LSGO in micro-supercapacitors

The electrochemical results on laser-scribed supercapacitors will be discussed in this chapter. The LightScribe® process has been proven to be effective in the production of micro-supercapacitors, showing good electrochemical performance. Graphene-based materials in LSGO exhibit EDLC behaviour, as expected for graphene-based electrodes [1]. In addition, the performance has been improved with the addition of $TiO_2$ nanoparticles in $TiO_2$-LSGO devices, which show greater electrochemical results compared to LSGO micro-supercapacitors, confirming the Faradaic effects introduced by $TiO_2$. Both the capacitive non-Faradaic and Faradaic processes will be investigated. Two different hydrogel polymer electrolytes were tested and their influence on the performance of the devices will be analyzed.

## 8.1 Electrochemical performance in PVA/$H_3PO_4$ micro-supercapacitors

The cyclic voltammetry (CV) curves of LSGO and $TiO_2$-LSGO micro-supercapacitors with PVA/$H_3PO_4$-based gel electrolyte are shown in figure 8.1. Preliminary measurements have been performed to identify the potential window in which the devices exhibit voltage stability. The potential window has been set in the range between 0 and 0.8 V, connected to the use of water as solvent in the preparation of the gel-electrolyte. To avoid electrochemical decomposition of water, occurring at 1.23 V, supercapacitors with aqueous electrolytes are typically cycled up to 1 V. In the case of gel-electrolytes using water as solvent, the voltage range is usually similar to that for aqueous electrolyte.

In LSGO micro-supercapacitor, the CV curves show a nearly rectangular shape, as characteristic of an electrochemical double layer capacitors (EDLC) [1]. For electrostatic charge storage, the current does not depend on the potential and it has opposite sign once potential sweep direction is changed [2]. When $TiO_2$ nanoparticles are combined with LSGO ($TiO_2$-LSGO), an enlargement in the area of CV curves is observed along with a slight deviation from the rectangular shape. Since at equal scan rate (dV/dt) the specific capacitance is proportional to the integral area of the curve, an increase in specific

capacitance is also achieved in $TiO_2$-LSGO compared to LSGO MSCs, resulting for all the scan rates. In detail, $TiO_2$-LSGO MSCs exhibit a remarkable enhancement at the lowest scan rate, almost doubling the integral area of the CV curve (figure 8.2). As the rate increases, the improvement in specific capacitance is reduced, yet at 10 mV/s is still about 20%, compared to LSGO MSCs

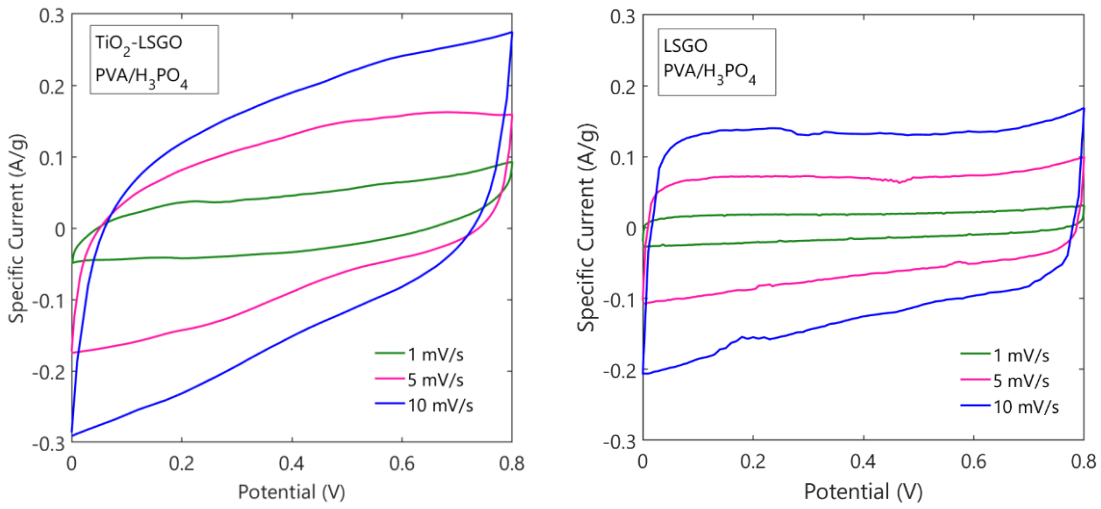


*Figure 8.1 Cyclic voltammetry curves of laser-scribed MSCs with PVA/$H_3PO_4$ gel electrolyte. $TiO_2$-LSGO and LSGO curves at different scan rates are shown on the left hand-side and on the right hand-side, respectively.*

The increase in specific capacitance, resulting from the enlargement of the integral area in the $TiO_2$-LSGO CV curve at 1 mV/s, can be observed in the comparison with LSGO at the same scan rate in figure 8.2. Here, the Faradaic effects induced by the presence of $TiO_2$ result both in the larger area of the curve and in redox peaks, observed at ~0.2 V. The greater performance at lower scan rate suggests that the Faradaic contribution is characterized by slower response time than the EDLC effect.

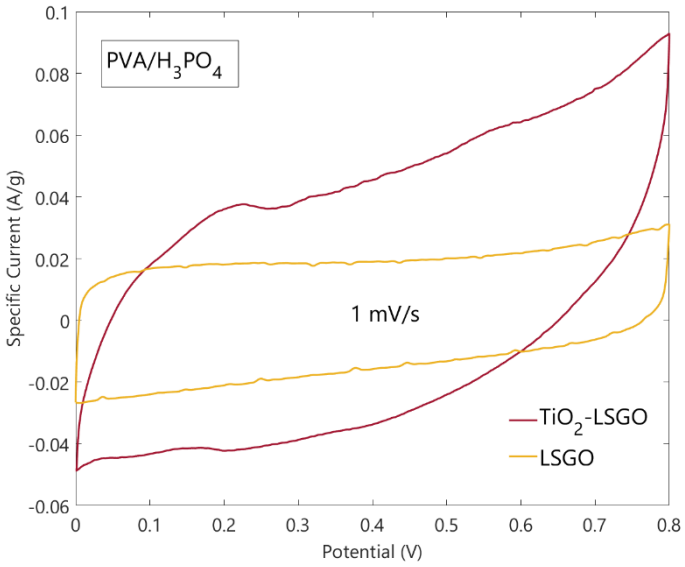


*Figure 8.2 Cyclic voltammetry curve of $TiO_2$-LSGO and LSGO MSCs with PVA/$H_3PO_4$ electrolyte at the rate of 1 mV/s.*

The increase in specific capacitance is also confirmed by galvanostatic charge and discharge measurements. Galvanostatic charge and discharge curves are shown in figure 8.3, at different current levels. LSGO micro-supercapacitor results give triangular-shaped curves, with a slight deviation from the ideal trend, at the lowest rate (0.05 A/g). When the charge storage mechanism is purely electrostatic, galvanostatic curves are triangular, as expected for an EDLC. Alterations from this trend can suggest further involved mechanisms in charge accumulation. In laser-scribed graphite oxide, the residual oxygen content form graphite oxide can contribute to this effect. In $TiO_2$-LSGO, the deviation from the triangular shape appears more evident than in LSGO, both at 0.05 A/g and 0.1 A/g, suggesting that a further contribution is involved in the storage mechanism due to the presence of $TiO_2$ nanoparticles. Thus, the charge storage in $TiO_2$-LSGO can be ascribed both to ECDL-like mechanism and to Faradaic effects, related to redox reactions occurring in $TiO_2$.

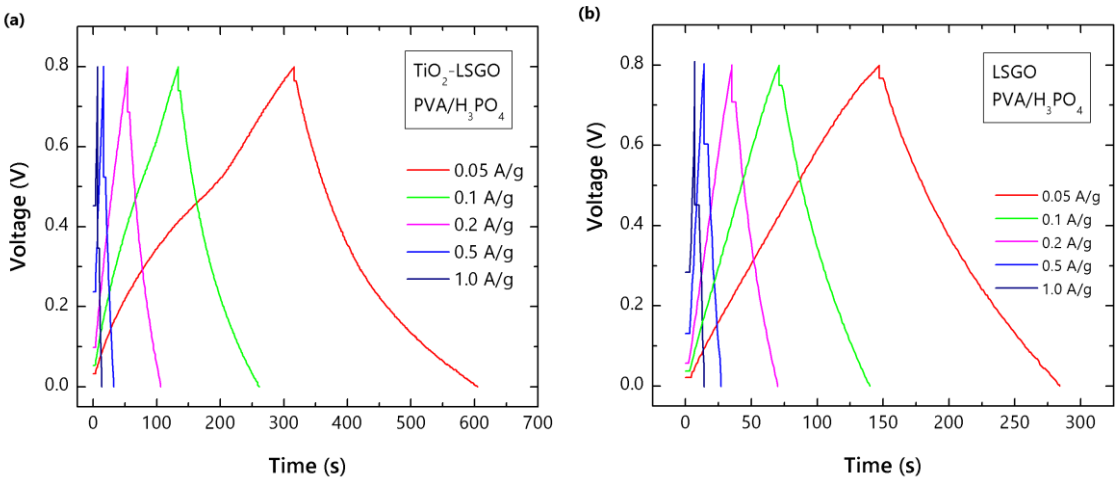


*Figure 8.3 Galvanostatic charge and discharge curves at different specific currents of (a) $TiO_2$-LSGO and (b) LSGO MSCs with PVA/$H_3PO_4$ gel-electrolyte.*

The specific capacitance was obtained from the slope of the galvanostatic curve. Specific capacitance values are shown in figure 8.4a, at each current density. In $TiO_2$-LSGO, the highest specific capacitance amounts at 92 F/g at a current density of 0.05 A/g, more than twice the value obtained for LSGO (35 F/g), at the same current density. As current density is greater, the discrepancy in specific capacitance is lowered, up to comparable values at 1 A/g, confirming the slower response time in $TiO_2$-LSGO. The specific energy is shown in figure 8.4b and maximum values are 2.0 and 0.8 Wh/kg for $TiO_2$-LSGO and LSGO, respectively. The theoretical maximum specific power has been obtained from the equation 4.7, considering the *ESR* of the supercapacitor from the *iR* drop in the galvanostatic curve, giving 350 and 459 W/kg for $TiO_2$-LSGO and LSGO, respectively. Though, the corresponding experimental power density achieved are 390 and 410 W/kg at the current density of 1.0 A/g for $TiO_2$-LSGO and LSGO, respectively. The value observed for $TiO_2$-LSGO MSC is higher than the theoretically expected one, which is likely to be underestimated due to the method used for evaluating the ESR. More accurate ESR measurements could be done by using electrochemical impedance spectroscopy.

The correlation of specific power and specific energy can be observed in a Ragone plot in figure 8.5. The mean Coulombic efficiency over 3000 cycles is >98% for both MSCs (figure 8.6). The capacitance retention exhibits a gradual decrease over cycles, consisting in an 83% retention of the specific initial capacitance for $TiO_2$-LSGO MSC, whereas fluctuations and a final 73% retention are observed for LSGO MSC (figure 8.7). The trend of LSGO MSC is overall lower than that of $TiO_2$-LSGO MSC. The fluctuating capacitance retention of the LSGO device is related to the low current level, close to the instrument sensitivity, which is

more affected by noise. The current value has been determined to compare $TiO_2$-LSGO and LSGO MSCs with a comparable specific current. The current level for LSGO is lower due to the smaller mass of the active material of the device.

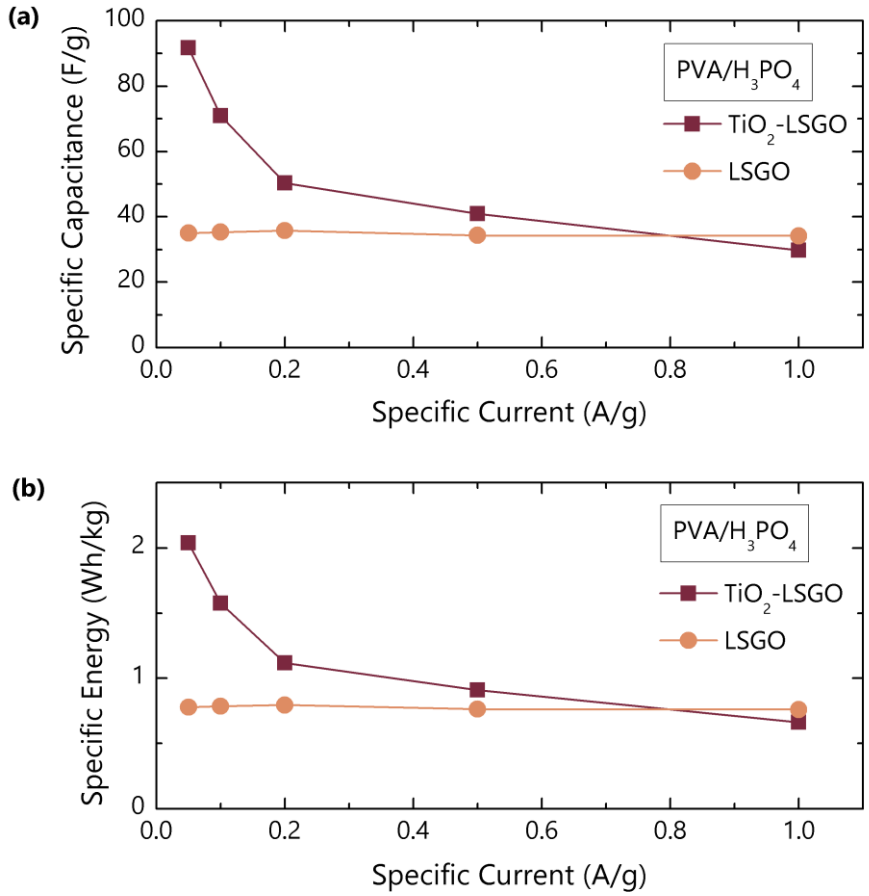


*Figure 8.4 (a) Specific capacitance and (b) specific energy achieved for $TiO_2$-LSGO and LSGO MSCs with PVA/$H_3PO_4$ gel-electrolyte at different specific currents. Values are averaged on 10 cycles at each specific current.*

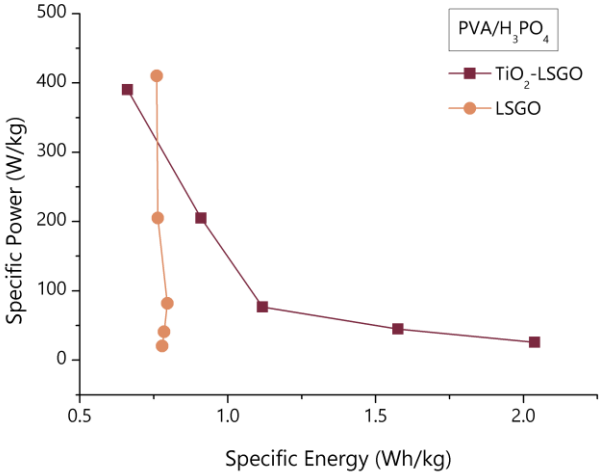


*Figure 8.5 Ragone plot for $TiO_2$-LSGO and LSGO MSCs with PVA/$H_3PO_4$ gel-electrolyte. Specific energy and specific power are obtained from galvanostatic charge and discharge curves at different specific currents.*

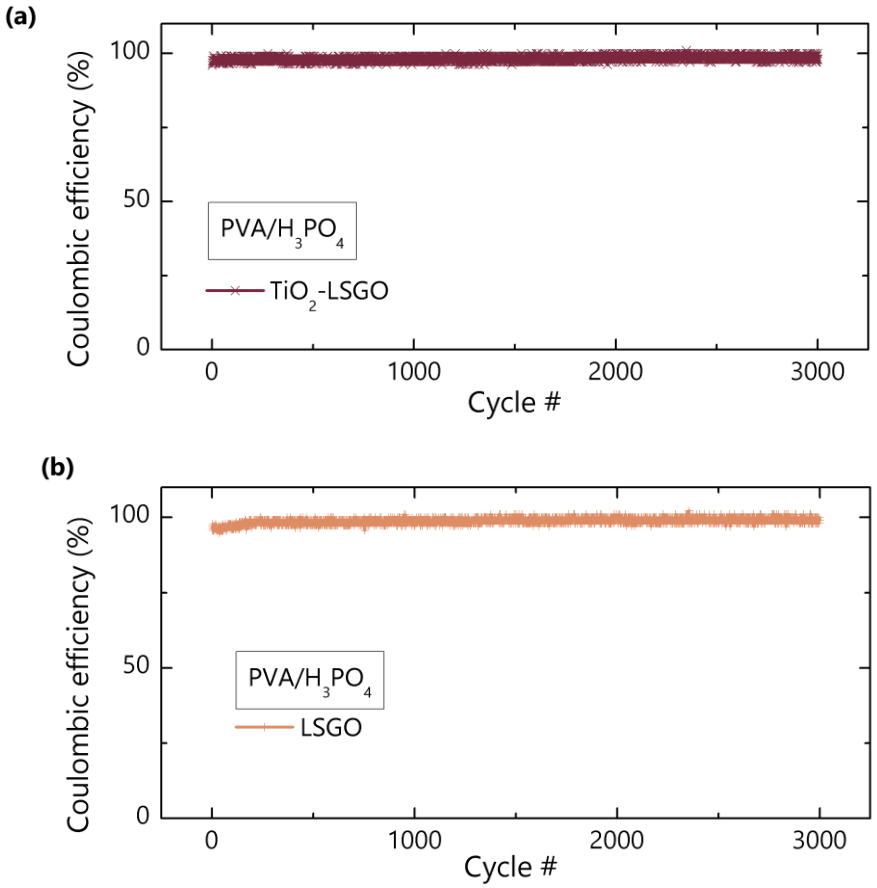


*Figure 8.6 Coulombic efficiency over 3000 charge and discharge cycles for (a) $TiO_2$-LSGO and (b) LSGO MSCs with PVA/$H_3PO_4$ gel-electrolyte.*

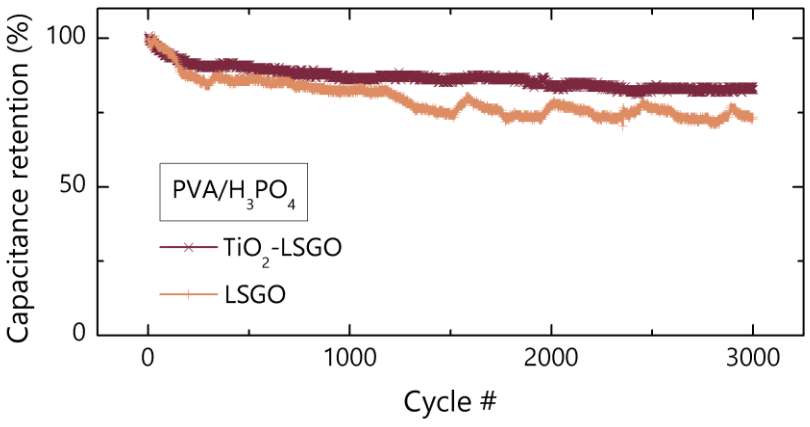


*Figure 8.7 Capacitance retention over 3000 charge and discharge cycles for (a) $TiO_2$-LSGO and (b) LSGO MSCs with PVA/$H_3PO_4$ gel-electrolyte.*

## 8.2 Electrochemical performance in PVA/$H_2SO_4$ micro-supercapacitors

The cyclic voltammetry (CV) curves of LSGO and $TiO_2$-LSGO micro-supercapacitors with PVA/$H_2SO_4$-based gel electrolyte are shown in figure 8.8. The potential window has been adapted from 0 to 0.8 V, as for PVA/$H_3PO_4$ based micro-supercapacitors.

In LSGO micro-supercapacitor, as observed for the PVA/$H_3PO_4$-based gel electrolyte MSC, CV curves show a nearly rectangular shape, verifying the EDLC behaviour of the device [1]. When $TiO_2$ nanoparticles are combined with LSGO ($TiO_2$-LSGO), an enlargement in the area of CV curves is observed, as well as for the PVA/$H_3PO_4$-based gel electrolyte MSC. Therefore, an increase in specific capacitance is also achieved in $TiO_2$-LSGO compared to LSGO MSCs, resulting for all the scan rates. In detail, $TiO_2$-LSGO MSCs exhibit a greater enhancement at lower scan rates (~25%), whereas at 10 mV/s is around 15%, compared to LSGO MSCs.

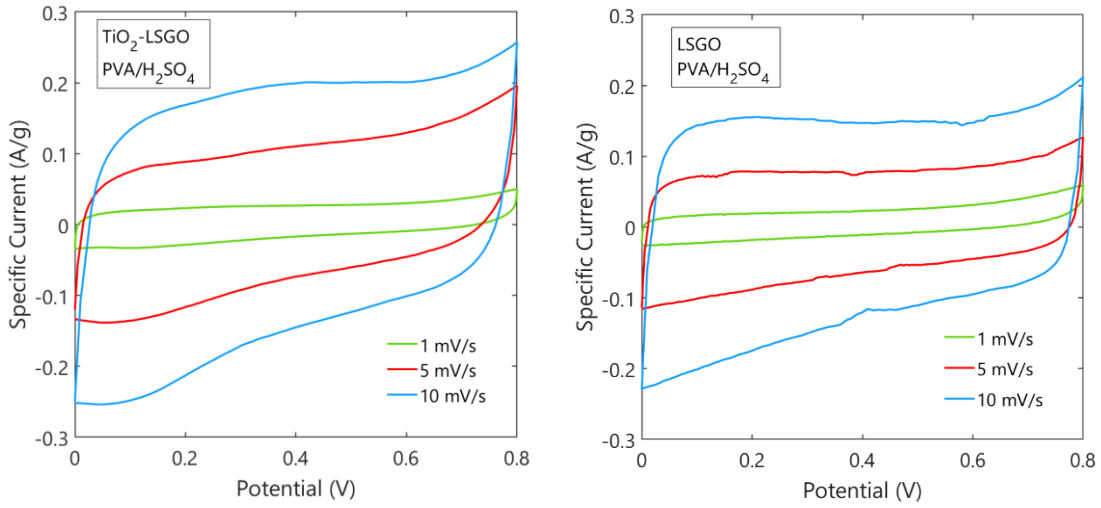


*Figure 8.8 Cyclic voltammetry curves of laser-scribed MSCs with PVA/$H_2SO_4$ gel-electrolyte. $TiO_2$-LSGO and LSGO curves at different scan rates are shown on the left hand-side and on the right hand-side, respectively.*

From the comparison of the cyclic voltammetry curves of $TiO_2$-LSGO and LSGO at the lowest rate (1 mV/s), the enlargement in the curve area can be seen in figure 8.9. In addition, redox peaks related to the presence of $TiO_2$ can be observed at ~0.1 V and at ~0.3 V. As for the PVA/$H_3PO_4$-based gel electrolyte MSC, the highest increase in specific capacitance is achieved for the slowest scan rate, due to the response time of the Faradaic contribution.

The linear trend in the upper part of the CV curve is ascribed to a resistive behaviour of the MSCs, due to the internal resistance of the devices.

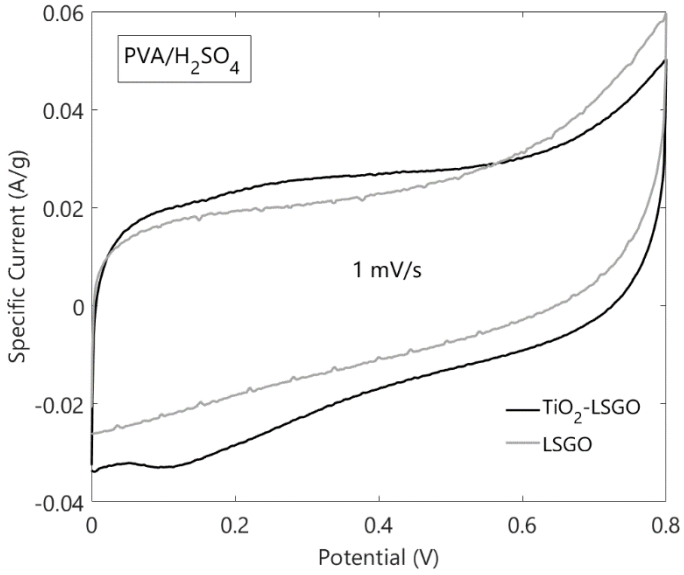


*Figure 8.9 Cyclic voltammetry curves of $TiO_2$-LSGO and LSGO MSCs with PVA/$H_2SO_4$ gel-electrolyte at the rate of 1 mV/s.*

The increase in specific capacitance is confirmed by galvanostatic charge and discharge measurements. Galvanostatic charge and discharge curves are shown in figure 8.10, at different current densities. As seen for the LSGO-PVA/$H_3PO_4$-based MSCs, also here LSGO curves show the triangular-shape, with a slight deviation from the ideal trend at the lowest rate (0.05 A/g). In $TiO_2$-LSGO, the deviation from the triangular shape is more pronounced than in LSGO, in the curves at 0.05 A/g and 0.1 A/g, confirming both the ECDL-like mechanism and Faradaic effects, related to redox reactions occurring in the presence of $TiO_2$ nanoparticles.

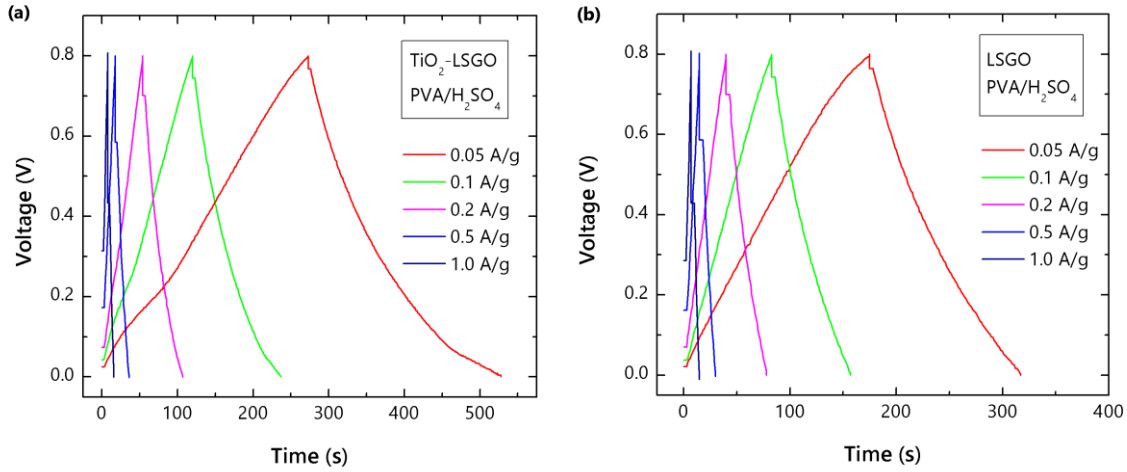


*Figure 8.10 Galvanostatic charge and discharge curves at different specific currents of (a) $TiO_2$-LSGO and (b) LSGO MSCs with PVA/$H_2SO_4$ gel-electrolyte.*

The specific capacitance, obtained from the slope of the galvanostatic curve is shown in figure 8.11a at each current density. In $TiO_2$-LSGO, the highest specific capacitance amounts at 65 F/g at a current density of 0.05 A/g, showing an over 70% increase compared to LSGO (37 F/g). As current density is greater, the discrepancy in specific capacitance is lowered, up to similar values at 1 A/g. This effect, similar to that observed in PVA/$H_3PO_4$-based MSCs, can be due to the slower response time in $TiO_2$-LSGO. The specific energy is shown in figure 8.11b and maximum values are 1.8 and 0.8 Wh/kg for $TiO_2$-LSGO and LSGO, respectively. The theoretical maximum specific power has been obtained from the equation 4.7, with 428 and 445 W/kg for $TiO_2$-LSGO and LSGO, respectively. Though, the corresponding experimental power density achieved 395 and 421 W/kg at the current density of 1.0 A/g for $TiO_2$-LSGO and LSGO, respectively. The correlation of specific power and specific energy can be observed in a Ragone plot in figure 8.12. The mean Coulombic efficiency over 3000 cycles gives 99.5% and 92.8% for $TiO_2$-LSGO and LSGO, respectively (figure 8.13a). The capacitance retention exhibits a larger stability for $TiO_2$-LSGO micro-supercapacitors, with 90% of capacitance retained after 3000 cycles, whereas in LSGO devices an 85% capacitance retention is achieved after 3000 cycles (figure 8.13b). In LSGO MSC, fluctuations have been observed as well as for LSGO MSC with PVA/$H_3PO_4$ gel-electrolyte, due to noise from the low current level.

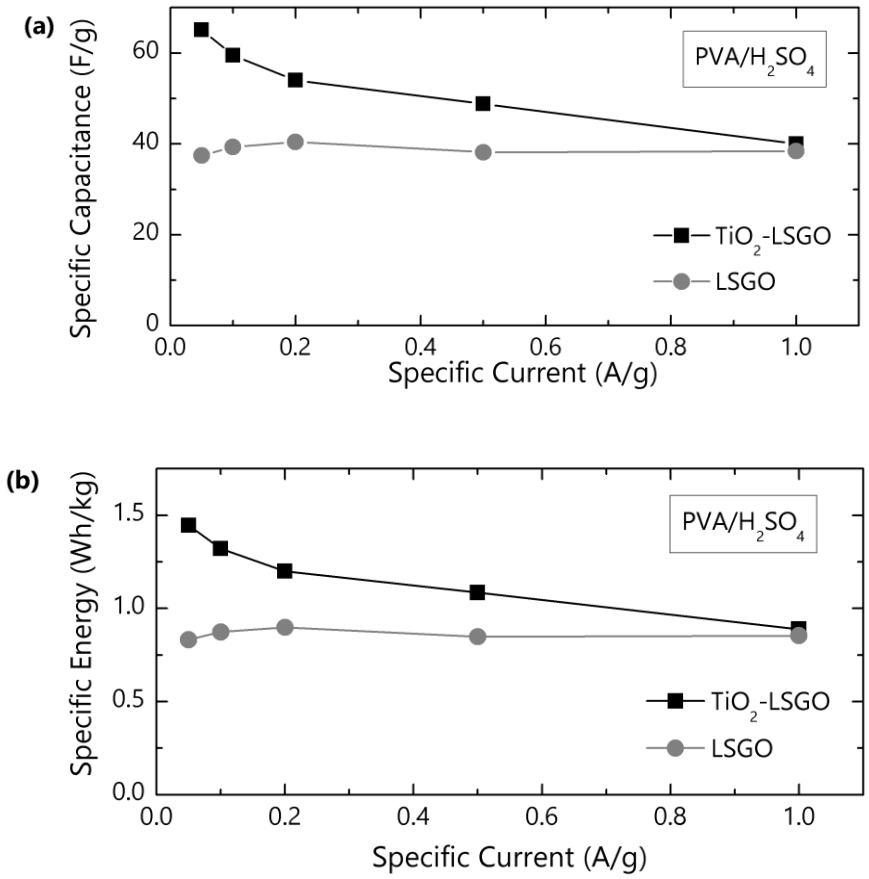


*Figure 8.11 (a) Specific capacitance and (b) specific energy achieved for $TiO_2$-LSGO and LSGO MSCs PVA/$H_2SO_4$ gel-electrolyte at different specific currents. Values are averaged on 10 cycles at each specific current.*

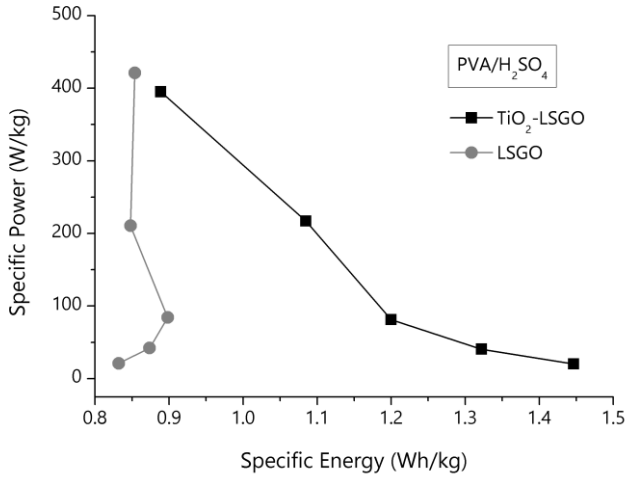


*Figure 8.12 Ragone plot for $TiO_2$-LSGO and LSGO MSCs with PVA/$H_2SO_4$ gel-electrolyte. Specific energy and specific power are obtained from galvanostatic charge and discharge curves at different specific currents.*

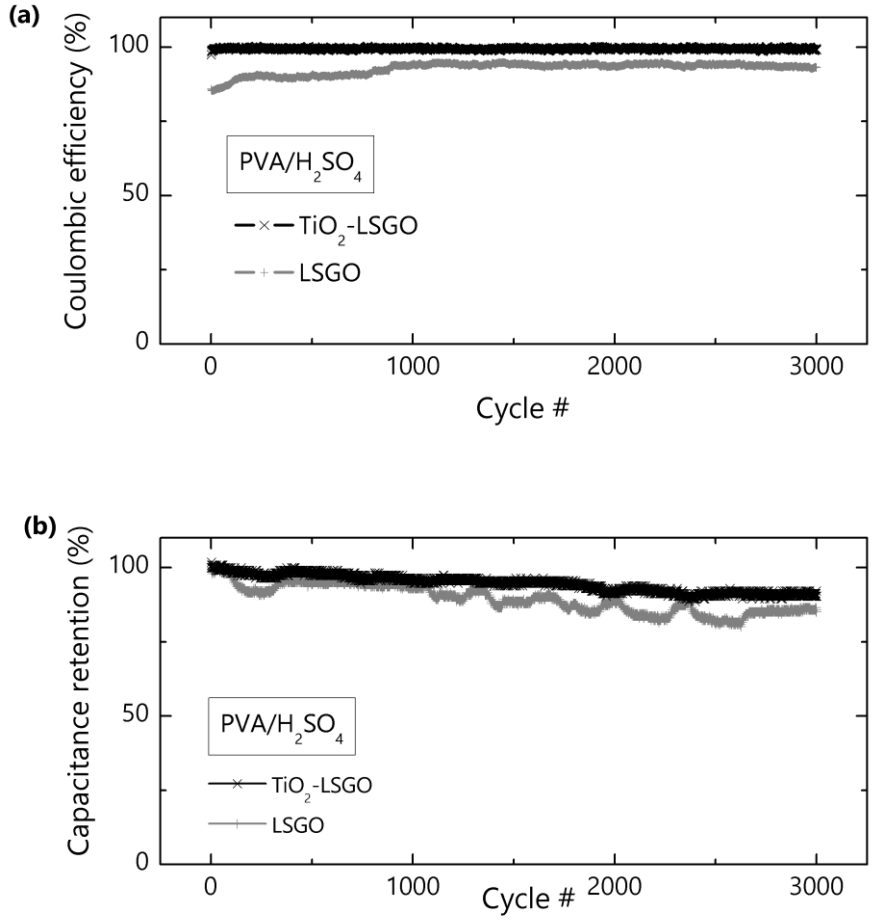


*Figure 8.13 (a) Coulombic efficiency and (b) capacitance retention over 3000 charge and discharge cycles for $TiO_2$-LSGO and LSGO MSCs with PVA/$H_2SO_4$ gel-electrolyte.*

## 8.3 Discussion

The electrochemical results on $TiO_2$-LSGO and LSGO micro-supercapacitors show an increase in the performance in the presence of anatase $TiO_2$ nanoparticles in the electrodes, compared to the LSGO devices. The enhancement is achieved for both the hydrogel polymer electrolytes tested, based on PVA/$H_2SO_4$ and PVA/$H_3PO_4$, respectively.

In LSGO devices, a typical EDLC behaviour is observed, both from the rectangular shape of CV curves and from the triangular shape of galvanostatic charge and discharge curves.

In $TiO_2$-LSGO devices, both EDLC behaviour and pseudocapacitive effects are achieved. Anatase nanoparticles are expected to introduce Faradaic effects in the charge storage mechanism [3,4]. This pseudocapacitive behaviour is here confirmed both in the cyclic

voltammetry curves and from galvanostatic charge and discharge measurements. In CV curves, the integral area is enlarged in $TiO_2$-LSGO. In addition, at low scan rates, redox peaks contributing to the increase in specific capacitance are also observed in MSCs with both the electrolytes. Regarding GCD investigation, the higher specific capacitance is confirmed by the values obtained from the slope of galvanostatic curves. At higher current density, the results of $TiO_2$-LSGO and LSGO give comparable performance. Specific energy is higher than in LSGO devices, especially at low current density, as observed for the specific capacitance. Remarkably, the $TiO_2$-LSGO devices exhibit excellent cycling stability in retaining the specific capacitance also after thousands of cycles.

$TiO_2$ in anatase phase has been reported to lead a higher increase in capacitance compared to the other $TiO_2$ polymorph, rutile, which is instead considered as a better source of cycle stability [3]. Here, as $TiO_2$ nanoparticles consist of anatase, a good specific capacitance is obtained (however, the comparison with the rutile phase cannot be considered here, since $TiO_2$ rutile has not been detected in $TiO_2$-LSGO material) and a great stability is additionally achieved, despite the absence of rutile.

Regarding the hydrogel electrolytes, good performance has been observed with two different electrolytes, confirming the right use of polymer gel electrolytes based on acidic conductive substances. It has been proven that a quick diffusion of $H^+$ from the electrolytes (here, from $H_3PO_4$ and $H_2SO_4$) can easily occur into graphene-based electrodes. The small $H^+$ size ensures that ions can be stored not only in the interface electrode/electrolyte but also in the bulk electrode [5]. Comparing the gel electrolytes, the PVA/$H_3PO_4$-based $TiO_2$-LSGO micro-supercapacitors give rise to an overall higher improvement in the electrochemical performance than PVA/$H_2SO_4$-based $TiO_2$-LSGO devices.

It is well known that transition metal oxides, such as $TiO_2$, $MnO_2$, $RuO_2$ can result as sources of pseudocapacitance, inducing a higher amount of charge stored in supercapacitors, where EDLC-like behaviour is combined with the pseudocapacitive effect [3,6–8]. In $TiO_2$, the Faradaic charge storage can be ascribed to two synergic mechanisms. The first consists of the intercalation and de-intercalation of cations from the electrolyte ($H^+$ in the electrolytes tested here) into the electrode, occurring during the charge and the discharge of the supercapacitor, while the second one involves surface adsorption according to [3]:

$$(TiO_2)_{surface} + H_3O^+ + e^- \leftrightarrow (TiO_2^- H_3O^+)_{surface} \qquad (8.1)$$

Both mechanisms are reported to determine the change in the oxidation state of Ti, from $Ti^{4+}$ to $Ti^{3+}$ with reduction and oxidation reactions, as further confirmed from redox peaks in cyclic voltammetry curves.

Regarding the electrolytes, the higher performance achieved with PVA/$H_3PO_4$-based can be ascribed to the larger amount of available $H^+$ ions than in PVA/$H_2SO_4$, keeping the same concentration [9]. Thus, a greater amount of charge stored can be achieved.

Finally, good performance has been achieved with the laser-scribed micro-supercapacitors. The combination of anatase $TiO_2$ nanoparticles with graphene-based material has been proven to be a successful strategy to increase the electrochemical properties of devices.

## References


[1] M.F. El-Kady, R.B. Kaner, Scalable fabrication of high-power graphene micro-supercapacitors for flexible and on-chip energy storage, Nat. Commun. 4 (2013) 1475–1479. https://doi.org/10.1038/ncomms2446.

[2] E. Frackowiak, F. Béguin, Carbon materials for the electrochemical storage of energy in capacitors, Carbon N. Y. 39 (2001) 937–950. https://doi.org/10.1016/S0008-6223(00)00183-4.

[3] L.L. Jiang, X. Lu, C.M. Xie, G.J. Wan, H.P. Zhang, T. Youhong, Flexible, free-standing TiO2-graphene-polypyrrole composite films as electrodes for supercapacitors, J. Phys. Chem. C. 119 (2015) 3903–3910. https://doi.org/10.1021/jp511022z.

[4] J. Kim, W.H. Khoh, B.H. Wee, J.D. Hong, Fabrication of flexible reduced graphene oxide-TiO2 freestanding films for supercapacitor application, RSC Adv. 5 (2015) 9904–9911. https://doi.org/10.1039/c4ra12980f.

[5] J.J. Yoo, K. Balakrishnan, J. Huang, V. Meunier, B.G. Sumpter, A. Srivastava, M. Conway, A.L. Mohana Reddy, J. Yu, R. Vajtai, P.M. Ajayan, Ultrathin planar graphene supercapacitors, Nano Lett. 11 (2011) 1423–1427. https://doi.org/10.1021/nl200225j.

[6] L. Jiang, Z. Ren, S. Chen, Q. Zhang, X. Lu, H. Zhang, G. Wan, Bio-derived three-dimensional hierarchical carbon-graphene-TiO2 as electrode for supercapacitors, Sci. Rep. 8 (2018) 1–9. https://doi.org/10.1038/s41598-018-22742-7.

[7] M. Toupin, T. Brousse, D. Bélanger, Charge storage mechanism of MnO2 electrode used in aqueous electrochemical capacitor, Chem. Mater. 16 (2004) 3184–3190. https://doi.org/10.1021/cm049649j.

[8] J.P. Zheng, T.R. Jow, A New Charge Storage Mechanism for Electrochemical Capacitors, J. Electrochem. Soc. 142 (1995) 60–62. https://doi.org/10.1149/1.2043984.

[9] Q. Chen, X. Li, X. Zang, Y. Cao, Y. He, P. Li, K. Wang, J. Wei, D. Wu, H. Zhu, Effect of different gel electrolytes on graphene-based solid-state supercapacitors, RSC Adv. 4 (2014) 36253–36256. https://doi.org/10.1039/c4ra05553e.

*This page intentionally left blank*

# Conclusions

Nanostructured $TiO_2$-graphene based materials have been demonstrated as effective electrode materials in Li-ion half-cells and in micro-supercapacitors.

Two approaches have been exploited to produce composite materials for Li-ion half cells: a hydrothermal synthesis and a high-energy ball milling treatment. The use of a thermally exfoliated graphite oxide (TEGO) as graphene has promoted the *in situ* hydrothermal synthesis of nanocrystalline anatase $TiO_2$ with size ~8 nm, starting from titanium tetraisopropoxide. A wide spread of truncated bipyramid-shaped nanoparticles was achieved over graphene layers, which acts as a support for the growth. The high-energy ball milling treatment has been proven as a promising alternative to chemical routes to produce a $TiO_2$-TEGO composite material. As expected from a high-energy process, disorder effects are introduced in the material, resulting in amorphous shell-like around the nanocrystalline $TiO_2$ and in deviation from stoichiometry.

The combination of TEGO with the *in situ* synthesized $TiO_2$ nanoparticles gives rise to improvement in the electrochemical performance of lithium-ion half cells compared to pristine $TiO_2$, with good electrical conductivity and remarkable cycle stability during cycling. In addition, the irreversibility of pristine TEGO after the first few cycles has been considerably reduced in the composite materials.

Two different relative contents of $TiO_2$:TEGO have been tested, (99:1) and (80:20) wt%, giving 180 and 121 mAh/g at C/5 (5h for discharging or charging) and 91 and 84 mAh/g at 2C, respectively. As the content of graphene increases compared to that of $TiO_2$, an irreversible behaviour was observed after the first few cycles, but the cycle stability has been remarkably recovered. The product with the lower ratio of graphene has led to the best performance in terms of specific capacity. Excellent capacity retention over 90% has been achieved in both the tested samples. The electrochemical results have proven the effectiveness of the graphene (TEGO) as a support for nanocrystalline $TiO_2$ in the electrode material. With its high electrical conductivity, graphene promotes the formation of a conductive network connecting anatase nanoparticles, achieving a fast charge transfer.

The composite $TiO_2$-TEGO obtained through the high-energy ball milling treatment shows comparable electrochemical performance to the hydrothermally synthesized material at low charge/discharge rate, whereas at higher rate the latter performs better. The smaller nanocrystal dimensions and the more intimate contact of the materials in the hydrothermally product are supposed to be responsible of the higher performance. However, high-energy ball milling treatment has revealed as a promising approach to obtain electrochemically active composite materials, with remarkable capacity retention over 90%.

Straightforward and large-scale technologies have been investigated to produce micro-supercapacitors electrodes, by the LightScribe® technique, using the DVD burner laser. An innovative approach has successfully promoted the growth of $TiO_2$ nanoparticles, starting from titanium tetraisopropoxide, along with the simultaneous conversion of graphite oxide in laser-scribed graphite oxide (LSGO). The novelty in the process consists in the *one-pot* synthesis of graphene-based materials and $TiO_2$ nanoparticles, forming the $TiO_2$-LSGO composite material.

The local increase in temperature as a result of the absorption of laser radiation by graphite oxide promotes both the nanoparticles crystallization and its conversion. An extensive spread of anatase nanoparticles without agglomeration has been obtained on LSGO surface, with size distribution peaked to 3-4 nm, comprising also 15-25 nm contributions. The conversion of graphite oxide into LSGO has led to a three order of magnitude increase in electrical conductivity.

In micro-supercapacitors, nanocrystalline $TiO_2$ combined with LSGO gives rise to a considerable increase in the electrochemical performance compared to LSGO. LSGO devices exhibit typical EDLC behaviour, whereas $TiO_2$-LSGO devices introduce Faradaic effects by redox reactions which are combined to non-Faradaic processes.

Two different hydrogel polymer electrolytes were tested. In PVA/$H_3PO_4$-based devices, specific capacitance of 92 and 35 F/g and specific energy of 2.0 and 0.8 Wh/kg (at 0.05 A/g) have been achieved for $TiO_2$-LSGO and LSGO, respectively. In PVA/$H_2SO_4$ the electrochemical performance is slightly lower, with 65 and 37 F/g and specific energy of 1.8 and 0.8 Wh/kg (at 0.05 A/g) for $TiO_2$-LSGO and LSGO, respectively.

The improvement of the performance in the presence of nanostructured $TiO_2$ can be ascribed both to the quick diffusion of $H^+$ from the electrolytes into the electrode and to the surface adsorption of $H_3O^+$ by titania particles, resulting in an increased specific capacitance. The electrolyte has an impact on the performance with better results in

PVA/$H_3PO_4$-based devices, due to the larger amount of available $H^+$ ions than in PVA/$H_2SO_4$.

In conclusion, nanostructured $TiO_2$-graphene based materials exhibit improved electrochemical properties both in lithium-ion half-cells and in micro-supercapacitors. The *in situ* synthesis of $TiO_2$ nanoparticles promotes the production of composite materials. The synergic action of $TiO_2$ and graphene enhances the cycling stability of the devices. The electrochemical performance is improved thanks to the conductive network formed by graphene with the electrochemically active sites of titania nanoparticles. Therefore, the combination of $TiO_2$ and graphene constitutes a successful strategy to produce cost-effective and large-scale products with competitive electrochemical performance for energy storage.

*This page intentionally left blank*

# Scientific activity

The scientific activities related to the PhD thesis work have been listed here.

**Publications:**

1. D. Pontiroli, S. Scaravonati, M. Sidoli, G. Magnani, L. Fornasini, C. Milanese, M. Riccò, Fullerene mixtures as negative electrodes in innovative Na-ion batteries, Chem. Phys. Lett. 731 (2019) 136607. https://doi.org/10.1016/j.cplett.2019.136607.
2. L. Fornasini, S. Scaravonati, G. Magnani, M. Sidoli, M. Riccò, P. P. Lottici, D. Bersani, D. Pontiroli, Enhanced laser-scribed micro-supercapacitors based on $TiO_2$-Laser Scribed Graphite Oxide, *to be submitted*.

**Posters at international conferences:**

1. L. Fornasini, G. Magnani, M. Sidoli, S. Scaravonati, G. Bertoni, D. Pontiroli, P. P. Lottici, M. Riccò, D. Bersani, 'Nanohybrid $TiO_2$-decorated graphene for energy applications', *Graphene2019: 9$^{th}$ edition of the largest European Conference & Exhibition in Graphene and 2D Materials*, 2019, Roma (Italy);
2. D. Pontiroli, G. Magnani, S. Scaravonati, L. Fornasini, M. Sidoli, A. Morenghi, M. Riccò, 'Graphene for energy storage applications', *Chemistry of graphene and applications in catalysis and polymer composites*, 2019, Milano (Italy);
3. D. Pontiroli, G. Magnani, S. Scaravonati, L. Fornasini, A. Morenghi, G. Bertoni, M. Riccò, 'Graphene-based materials for supercapacitors', *Graphene2018: 8$^{th}$ edition of the the largest European Conference & Exhibition in Graphene and 2D Materials*, 2018, Dresden (Germany).

Other activities non-related to the PhD thesis work - performed during the phD - have been listed here.

**Publications:**

1. L. Fornasini, L. Bergamonti, F. Bondioli, D. Bersani, L. Lazzarini, Y. Paz, P.P. Lottici, Photocatalytic N-doped TiO2 for self-cleaning of limestones, Eur. Phys. J. Plus. 134 (2019) 539. https://doi.org/10.1140/epjp/i2019-12981-6.
2. D. Bersani, S. Andò, L. Scrocco, P. Gentile, E. Salvioli-Mariani, L. Fornasini, P.P. Lottici, Composition of Amphiboles in the Tremolite–Ferro–Actinolite Series by Raman Spectroscopy, Minerals. 9 (2019) 491. https://doi.org/10.3390/min9080491.
3. D. Giordano, D. González-García, J.K. Russell, S. Raneri, D. Bersani, L. Fornasini, D. Di Genova, S. Ferrando, M. Kaliwoda, P.P. Lottici, M. Smit, D.B. Dingwell, A calibrated database of Raman spectra for natural silicate glasses: implications for modelling melt physical properties, J. Raman Spectrosc. (2019) 1–17. https://doi.org/10.1002/jrs.5675.
4. D. Pontiroli, S. Scaravonati, G. Magnani, L. Fornasini, D. Bersani, G. Bertoni, C. Milanese, A. Girella, F. Ridi, R. Verucchi, L. Mantovani, A. Malcevschi, M. Riccò, Super-activated biochar from poultry litter for high-performance supercapacitors, Microporous Mesoporous Mater. 285 (2019) 161–169. https://doi.org/10.1016/j.micromeso.2019.05.002.
5. L. Bergamonti, G. Predieri, Y. Paz, L. Fornasini, P.P. Lottici, F. Bondioli, Enhanced self-cleaning properties of N-doped TiO2 coating for Cultural Heritage, Microchem. J. 133 (2017) 1–12. https://doi.org/10.1016/j.microc.2017.03.003.
6. F. Košek, A. Culka, L. Fornasini, P. Vandenabeele, A. Rousaki, J. Mirao, D. Bersani, A. Candeias, J. Jehlička, Application of portable Raman spectroscopy for the screening of colored secondary sulfates in abandoned mining areas – the case of São Domingos Mine (Iberian Pyrite Belt), *under review to J. Raman Spectrosc*.

**Posters at international conferences:**

1. G. Magnani, D. Pontiroli, S. Scaravonati, L. Fornasini, D. Bersani, G. Bertoni, C. Milanese, A. Girella, F. Ridi, R. Verucchi, L. Mantovani, A. Malcevschi, M. Riccò, 'High performance supercapacitors from poultry litter super activated biochar', *Graphene2019: 9$^{th}$ edition of the largest European Conference & Exhibition in Graphene and 2D Materials,* 2019, Roma (Italy);
2. G. Barone, L. Bergamonti, D. Bersani, L. Fornasini, C. Graiff, P. P. Lottici, P. Mazzoleni, S. Raneri, 'Durability of self-cleaning coating based on N-doped $TiO_2$ on *Perlatino* limestone', *Technart 2019: International Conference on the use of Analytical Techniques for Characterization of Artworks*, 2019, Bruges (Belgium);
3. S. Raneri, M. Masotta, M. Lezzerini, D. Bersani, P.P. Lottici, M. Marino, L. Fornasini, G. Barone, P. Mazzoleni, 'Raman analysis of silica glasses with composition typical

of the Roman age', *GeoRaman 2018, XIII International GeoRaman conference,* 2018, Catania (Italy);

4. G. Gennari, D. Bersani, L. Fornasini, L. Bergamonti, P. P. Lottici, M. Branchi, L. Tireni, F. Zanella, 'In situ raman spectroscopy of microbial pigments for the identification of biocolonisations on art objects', *inArt 2018: 3rd International Conference on Innovation in Art Research and Technology*, 2018, Parma (Italy);
5. G. Barone, L. Bergamonti, D. Bersani, L. Fornasini, P. P. Lottici, P. Mazzoleni, S. Raneri, R. Rubulotta, 'Nature of pigments in natural and cultured pearls by using Raman spectroscopy', *RAA 2017, 9th International Congress on the Application of Raman Spectroscopy in Art and Archaeology*, 2017, Evora (Portugal);
6. G. Barone, L. Bergamonti, D. Bersani, L. Fornasini, U. Longobardo, P. Mazzoleni, S. Raneri, P. P. Lottici, 'Potentiality of Raman spectroscopy for pearls: characterization and authentication', *Technart: Non-destructive and microanalytical techniques in art and cultural heritage*, 2017, Bilbao (Spain).

**Conference talks at international conferences:**

1. L. Fornasini, L. Bergamonti, G. Predieri, Y. Paz, D. Bersani, P. P. Lottici, F. Bondioli, 'Self-cleaning coatings by N-doped $TiO_2$ on limestones', *Technart: Non-destructive and microanalytical techniques in art and cultural heritage*, 2017, Bilbao (Spain);
2. L. Fornasini, L. Bergamonti, F. Bondioli, G. Predieri, L. Lazzarini, Y. Paz, P. P. Lottici, 'Application of photocatalytic N-doped $TiO_2$ on three different types of limestones', *inArt 2018: 3rd International Conference on Innovation in Art Research and Technology*, 2018, Parma (Italy).

*This page intentionally left blank*

# Acknowledgements

After this three-year journey, I would like to thank each one of my travel companions. You have been a source of inspiration to me and motivated me to discover new lands, every day.

Vorrei dedicare il primo ringraziamento al mio supervisore Danilo Bersani, per essere stato un faro di scienza, oltre che di vita. Grazie Danilo per avermi dato innumerevoli opportunità di conoscere argomenti apparentemente differenti che mi hanno permesso di lavorare con così tante persone. Grazie per essere sempre stato presente e per essere un riferimento fondamentale.

Al prof. Pier Paolo Lottici rinnovo un particolare ringraziamento, per aver continuato a dedicare tempo a questa ricerca e agli altri lavori avviati in precedenza, e perché ogni ora trascorsa nel suo ufficio fa imparare qualcosa di più.

Vorrei ringraziare tutti i *convitati* del Laboratorio di Nanostrutture di Carbonio, dove disponibilità, buon umore, aiuto reciproco, ascolto e curiosità erano gli ingredienti fondamentali di ogni giornata (a cui spesso e volentieri si aggiungevano dolci e leccornie). Un ringraziamento a Mauro Riccò, per avermi fatto conoscere il *nano*-mondo del carbonio. Grazie Daniele Pontiroli, per trasmettere quotidianamente la passione che metti nel tuo lavoro e grazie per la tua interminabile gentilezza. Grazie ai compagni di laboratorio: con voi imparare è diventato un divertimento. Grazie Giacomo per avermi fatto conoscere le ricette delle sintesi. Grazie Silvio, Michele e Alberto, per avermi svelato i segreti di batterie e supercondensatori.

Desidero ringraziare i coordinatori del corso di dottorato, Stefano Carretta e Cristiano Viappiani, per essere sempre stati un punto di riferimento.

Grazie Luciana Mantovani e Laura Bergamonti, per la vostra inconfondibile disponibilità. Grazie per aver condiviso l'esperienza di *inArt 2018* dietro le quinte insieme a voi e con Lavinia, Jasmine, Claudia e Marianna. Grazie a Giovanni Bertoni per aver reso visibili le nanoparticelle. Grazie a Lucrezia Aversa and Roberto Verucchi, per le analisi alla miriade di campioni.

I would like to thank also Vittoria Pischedda, Alexis, Hatem and your colleagues for hosting me in your labs in Lyon. You let me discover the *huge* world of high-pressure.

Thanks to all the professors and researchers who I have met over the past three years, from Sicily to Belgium, from Portugal to Czech Republic. It has been a pleasure to work with you, both on Cultural Heritage and minerals.

Grazie Fabrizia, Vincenzo e Francesco, per questa bella esperienza insieme, con tanti caffè e nonostante i pranzi organizzati male e le uscite troppo rare. L'amicizia che è nata non termina con questo viaggio.

E a chi aspettava che la nave tornasse al porto, che il treno non chiudesse le porte, che l'aereo arrivasse in orario, grazie. Grazie a chi aspettava il ritorno con la luce accesa. A chi illuminava la giornata con una danza. A chi ascoltava e accendeva un sorriso. A chi era felice con una fetta di tenerina. A chi è casa, ovunque.

Grazie *a chi è stato vicino da vicino* e *a chi vicino da lontano*.